Université Fédérale

Toulouse Midi-Pyrénées

THÈSE

En vue de l'obtention du

DOCTORAT DE L'UNIVERSITÉ DE TOULOUSE

Délivré par :

École Nationale Supérieure des Mines d'Albi-Carmaux conjointement avec l'INP Toulouse

---

Présentée et soutenue par :
Victor POZZOBON

le 17 novembre 2015

Titre :

Biomass gasification under high solar heat flux

École doctorale et discipline ou spécialité :
ED MEGEP : Génie des procédés et de l'Environnement

Unité de recherche :
Centre RAPSODEE, CNRS UMR 5302, École des Mines d'Albi-Carmaux

Directeur/trice(s) de Thèse :

Sylvain SALVADOR et Jean-Jacques BEZIAN

Jury :
Michel QUINTARD - Directeur de Recherche CNRS - Institut de Mécanique des Fluides de Toulouse - Président du jury
Jean-François THOVERT - Directeur de Recherche CNRS - Institut Pprime - Rapporteur
Laurent VAN DE STEENE - Chargé de Recherche - Laboratoire CIRAD - Rapporteur
Gilles FLAMANT - Directeur de Recherche CNRS - Laboratoire PROMES - Examinateur
Fabrice PATISSON - Professeur - École des Mines de Nancy - Examinateur
Sylvain SALVADOR - Professeur - École des Mines d'Albi-Carmaux - Directeur de thèse
Jean-Jacques BEZIAN - Ingénieur - École des Mines d'Albi-Carmaux - Directeur de thèse

Biomass gasification under high solar heat flux

Victor POZZOBON

Under the direction of

Sylvain SALVADOR and Jean-Jacques BEZIAN

PhD thesis defended on the 17th of November 2015

This work was funded by the French "Investments for the future" program managed by the National Agency for Research under contract ANR-10-LABX-22-01.

École Nationale Supérieure des Mines d'Albi-Carmaux

To my father,
the man who passed
his appreciation of personal effort and
love of work well done on to me.

A mon père,
l'homme qui m'a transmis
son goût de l'effort et
son amour du travail bien fait.

Abstract / Résumé

Biomass gasification under high solar heat flux

Abstract:

Concentrated solar energy is as an alternative energy source to power the thermochemical conversion of biomass into energy or materials with high added value. Production of syngas from lignocellulosic biomass is an example, as well as the production of carbonaceous residues with controlled properties.

This work focuses on the study of the behaviour of a thermally thick beech wood sample under high solar heat flux (higher than 1000 kW/m^2). Two approaches have been undertaken at the same time: an experimental study and the development of a numerical model.

Experiments have highlighted a specific behaviour of beech wood under high solar heat flux. Indeed, a char crater, symmetrical to the incident heat flux distribution, forms in the sample. This study has also shown that biomass initial moisture content has a strong impact on its behaviour. The dry sample can achieve an energetic conversion efficiency of 90 %, capturing up to 72 % of the incident solar power in chemical form. While, high initial moisture content samples produce more hydrogen, at the price of an energetic conversion efficiency around 59 %. Furthermore, tar thermal cracking and steam reforming are enabled by the temperatures reached (higher than 1200 °C) and the presence of water. Finally, wood fiber orientation has been shown to have only a minor impact on its behaviour.

At the same time, a modelling of the coupled reactions, heat and mass transfers at stake during solar gasification was undertaken. The development of this model has highlighted the necessity to implement innovative strategies to take into account radiation penetration into the medium as well as its deformation by gasification. Numerical model predictions are in good agreement with experimental observations. Based on the model predicted behaviour, further understanding of biomass behaviour under high solar heat flux was derived. In addition, sensitivity analyses revealed that Arrhenius type models are not fitted for precise intra-particular water behaviour description and that the choice of the pyrolysis scheme is key to properly model biomass behaviour under high solar heat flux.

Keywords: Solar energy, Pyrolysis, Gasification, High heat flux, Drying, Wood.

Gazéification de biomasse sous haute densité de flux solaire

Résumé :

L'énergie solaire concentrée est une source d'énergie alternative pour la conversion thermochimique de biomasse en vecteurs énergétiques ou en matériaux à haute valeur ajoutée. La production d'un gaz de synthèse à partir de biomasse lignocellulosique en est un exemple, de même que la production de résidus carbonés à propriétés contrôlées.

Ces travaux portent sur l'étude du comportement d'un échantillon de hêtre thermiquement épais sous de hautes densités de flux solaire (supérieures à 1000 kW/m^2). Deux approches ont été développées en parallèles : une étude expérimentale et le développement d'un modèle numérique.

Les expériences ont permis de mettre en lumière le comportement particulier du hêtre sous de hautes densités de flux solaire. En effet, un cratère de char, dont la forme correspond à celle de la distribution du flux incident, se forme dans l'échantillon. Cette étude a aussi montré que la teneur en eau initiale de la biomasse a un fort impact sur son comportement. Les échantillons secs peuvent atteindre un rendement de conversion énergétique de 90 %, capturant jusqu'à 72 % de l'énergie solaire incidente sous forme chimique. Quant aux échantillons humides, ils produisent nettement plus d'hydrogène, au prix d'un rendement de conversion énergétique aux alentours de 59 %. De plus, le craquage thermique et le reformage des goudrons produits par la pyrolyse sont rendus possibles par les températures atteintes (supérieures à 1200 °C) et la présence d'eau. Enfin, il a été montré que l'orientation des fibres du bois n'a qu'un impact mineur sur son comportement.

En parallèle, une modélisation des transferts couplés chaleur matière et des réactions chimiques mis en jeu lors de la gazéification solaire d'un échantillon a été développée. La construction du modèle a mis en avant la nécessité de recourir à des stratégies innovantes pour prendre en compte la pénétration du rayonnement dans la matière ainsi que la déformation du milieu par la gazéification. Les prédictions du modèle montrent un bon accord avec les observations expérimentales. Elles ont ainsi permis de mieux comprendre les couplages mis en jeu lors de la dégradation de biomasse sous haute densité de flux solaire. De plus, des analyses de sensibilités ont révélé que les modèles de type Arrhenius ne permettent pas de décrire finement le comportement de l'eau à l'intérieur de l'échantillon et que le choix du modèle de pyrolyse était capital pour décrire correctement le comportement la biomasse sous haute densité de flux solaire.

Mots-clés : Energie solaire, Pyrolyse, Gazéification, Haute densité de flux, Séchage, Bois.

Table of contents

Nomenclature

Latin symbols

A	frequency factor, 1/s
a	pyrolysis water production factor, -
Bi	Biot number, -
b	pyrolysis char production correction factor, -
c_p	specific heat capacity, J/kg/K
D	diffusivity, m^2/s
d	diameter, m
Da_{III}	Damköhler III number, -
dt	time between two frames, s
e	steel screen thickness, m
Ea	activation energy, J/mol
g	gravity acceleration, m/s^2
h	convective heat transfer coefficient, $W/m^2/K$
Kn	Knudsen number, -
k_B	Boltzmann constant, J/K
k	reaction rate coefficient, 1/s
L	characteristic length, m
m	mass, kg
M	molar mass, g/mol
P	power, W
Pe	Péclet number, -
p	pressure, Pa
Q	volume heat source, W/m^3
q	relative permeability, -
r	radius, m
$\Re$	ideal gas constant, J/mol/K
Re	Reynolds number, -
S	pore liquid water saturation, -
T	temperature, K
t	time, s
u	velocity, m/s

Latin symbols

V	volume, m^3
X	inverse method sensitivity matrix, -
Y	mass fraction, -
y	inverse method observable, -
z	height, m

Greek symbols

α	absorptivity, -
Δh	reaction heat, J/kg
ΔH	reaction heat, J/mol
Δ	Laplacian operator, $1/m^2$
δ	difference symbol, -
ϵ	emissivity, -
ζ	porosity, -
κ	permeability, m^2
λ	thermal conductivity, W/m/K
μ	dynamic viscosity, Pa.s
ν	stoichiometric coefficient, -
ξ	radiation penetration coefficient, -
ρ	density, kg/m^3
σ	Stefan-Boltzmann constant, $W/m^2/K^4$
τ	tortuosity, -
ϕ	incident heat flux, W/m^2
Ψ	radiative heat loss function, W/m^2
ω	reaction rate, $kg/m^3/s$

Subscripts

$benzene$	benzene
bw	bound water
cap	capillary
$chamber$	reaction chamber
$char$	char
$cond$	with tar condenser
D	Darcy
eff	effective
fin	final
fs	focal spot
g	gas phase
gas	light gas
$gasi$	gasification
I	gaseous species index
i	frame pixel index in x direction
ini	initial
$intrinsic$	intrinsic
is	intermediate solid
J	solid species index
j	frame pixel index in y direction
K	reaction index
lim	limit
$long$	longitudinal
$loss$	loss
lw	liquid water
$mass$	mass
max	maximum
$no\ cond$	without tar condenser
ols	estimated using ordinary least square
p	painting
pen	penetration
$pore$	pore
$pyro$	pyrolysis
rad	radiative
$reac$	reaction
s	solid phase
$sand$	sand
sat	saturation
sp	sample
st	steel
$steam$	steam
sur	surrounding
tar	tar
th	thermal
$water$	water
$wood$	wood

Superscripts

k	frame time index
M	total number of solid specie
n	total number of frame
N	total number of gaseous specie
O	total number of reaction
T	matrix transposition operator
$\hat{}$	ordinary least square estimator

Other symbols

.	scalar product
$\times$	matrix product
$\boldsymbol{A}$	vector and matrix notation
$\boldsymbol{I}$	unit tensor
H	homothetic center, -
$\boldsymbol{n}$	normal vector, -
$\mathcal{U}$	uniform density law
∇	nabla operator, 1/m
$\prod$	product
$\sum$	sum
$< >$	mean
$\| \|$	norm
lim	limit

Introduction

Introduction

World primary energy consumption has dramatically grown over the last thirty years, from 7.14 Gtoe (Giga ton of oil equivalent) in 1980 to 13.2 Gtoe in 2012 (Fig. 1). This increase heavily rested upon fossil fuels (oil, coal and natural gas) and led to the emission of important quantities of green house effect gases in the atmosphere [1]. In turn, these gases induced global warming and climate change [2]. If not stopped, climate change will lead to more frequent extreme meteorological events. Furthermore global warming will induce a decrease in agricultural yields in tropical and temperate regions, thus endangering food security. It is therefore mandatory to keep, in the coming century, global warming below 2 °C above pre-industrial temperatures in order to avoid its most dire consequences.

At the same time, a major increase in primary energy consumption is foreseen. In its central scenario, the *International Energy Agency* predicts a 37 % growth in global energy demand by 2040 [3]. While the *US Energy Information Administration* projects a 56 % increase over the same period [4]. This rise will be driven by a increasing energy consumption in Asia, Africa, the Middle East and Latin America, which will put the world on a path consistent with a 3.6 °C global warming. Mankind should therefore reduce its reliance on fossil fuels and switch to renewable carbon neutral energy sources such as wind, hydraulic, solar power or biomass.

Among these sources, solar energy is believed to be a promising candidate because of its versatility and growth potential. Indeed, solar power can directly produce electricity thanks to photovoltaic panels. It can also generate low to high temperature heat and therefore be used in many domestics and industrial applications, ranging from producing sanitary water to cracking water molecules to produce hydrogen [5]. Nevertheless, solar energy is in essence an intermittent energy source and its storage still remains a challenge to be faced in the years to come.

Biomass is also of interest. This name groups renewable carbonaceous feedstock ranging from algae to municipal wastes. Biomass can undergo various transformations in order to be valorized, for instance, as heat via combustion, as methane via methanation or as syngas via gasification. Syngas is a mixture of hydrogen

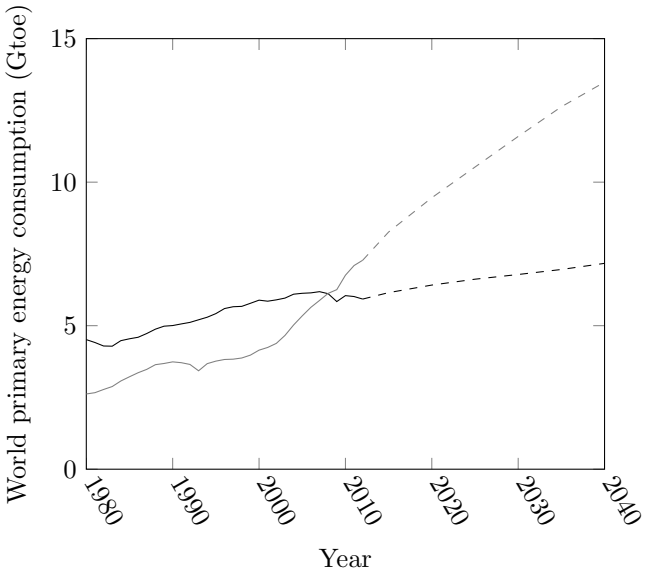

FIGURE 1: World primary energy consumption. Continuous lines: history, dashed lines: projections. Black: OECD, gray: non-OECD [4]

and carbon monoxide which has a wide number of applications. These applications include solid oxide fuel cell, gas turbine combustion, running engines, firing in bricks factory or glass kiln, Fisher Tropsch synthesis, sorted from high to low H_2/CO ratio [6]. Gasification is highly endothermic and requires temperatures higher than 800 °C to be led. Classically, the required heat is supplied by burning a fraction of the inlet biomass feed. Two main drawbacks come with this technique: the efficiency with respect to the biomass is lowered and the produced syngas is diluted by nitrogen from the combustion air.

The combination of biomass and solar energy may yield several benefits. Indeed, a synergy of these two energy sources can be envisioned. It is possible to use concentrated solar energy to power biomass gasification. The produced syngas could therefore be considered as a new vector of solar energy. It would also allow to avoid the biomass combustion associated drawbacks.

After the first oil crisis, studies on the combination of biomass gasification and concentrated solar power have been undertaken [7]. Yet, the appeal of this field of science deflated with the decrease of the the oil barrel price [8]. Nowadays, the interest in the combination of biomass and solar energy is rising again. Economical assessments have shown the potential viability of this approach [9], while technical studies have aimed at increasing the efficiency of solar gasification reactors [10, 11].

However, these studies mainly focused on reactor scale experiments and modeling, in fixed bed [7, 12–14], fluidized bed [15, 16] and cyclonic reactors [17–19]. Yet, they do not permit understanding of biomass and solar power interaction in a scientific vision.

The combination of solar energy and biomass still raises several questions at the sample scale. Radiative power has long been seen only as a way to achieve high heating rates [20–24] in laboratory scale experiments. It is only recently that solar pyrolysis has been studied in order to assess produced char properties [25]. The study featured agglomerated wood powder pellets that were suitable to lead a thermally thin experiment, but not to understand the interaction between biomass and solar energy. Furthermore, the behaviour of a virgin piece of biomass under high solar heat flux has never been studied.

In addition to the general behaviour of biomass in itself, the combination of biomass and concentrated solar energy raises several questions. For instance, under high solar heat flux, biomass would experience high heating rates and high final temperature. High heating rates could lead to:

- a very quick vaporisation of the water inside the sample, leading to a sharp increase of the internal pressure, which may, in turn, induce mechanical failure. This kind of phenomena would depend on sample heating rate, wood structure and initial moisture content
- fast pyrolysis yielding very small amounts of residual carbon solid and the rapid surface ablation of the medium

High temperature could enable:

- in situ tar thermal thermal cracking and steam reforming, as well as char gasification
- char thermal annealing
- carbon sublimation, if reached temperatures are high enough

This work aims at tackling these questions. First, literature was reviewed. On a very practical level, this review of literature has oriented toward to use beech wood (*Fagus sylvatica*) as model biomass, because it is commonly used which has two considerable advantages: allowing for comparison with other studies and increasing the availability of thermo-physical properties mandatory for numerical modelling. Then, biomass behaviour under high solar heat flux was investigated via an experimental approach as well as a numerical one. On one hand, a new experimental device allowing the exposure of a thermally thick beech wood sample to heat flux higher than 1000 kW/m^2 was built and calibrated. Then, the impact of wood initial moisture content and wood fiber orientation relative to the incident heat flux was explored. On the other hand, a new numerical model was developed. It features momentum, heat and mass conservation equations as well as radiation penetration inside of the reacting medium. The agreement between experimental observations and numerical predictions is good enough for us to be confident in the numerical model descriptive capacities. It was then used to derive a better understanding of biomass behaviour under high solar heat flux.

First of all, experimental investigations have highlighted an unreported behaviour of biomass under high solar heat flux. Indeed, a char crater appears at the center of the sample. Its shape corresponds to the heat flux distribution at the focal spot of the concentrating device. Wood initial moisture content is shown to be a key parameter that has a major impact on every aspect of biomass degradation under high solar heat flux. Surprisingly, wood fiber orientation relative to the incident heat flux is shown to have almost no influence on biomass behaviour. Numerical investigations yielded valuable insight on the phenomena at stake during solar gasification. For instance, they confirm that achieved temperatures lead to tar thermal cracking and that radiation penetration inside of the sample has to be taken into account.

Manuscript structure

This manuscript is divided into five chapters presenting the work accomplished during this PhD. For the sake of readability, it was chosen to keep this manuscript as short as possible.

Chapter 1 presents a review of the literature dealing with biomass pyrolysis and gasification. As this topic is very wide, a focus was set on solar energy and biomass pyro-gasification combination. The first part briefly presents the main subjects at stake in this work: solar energy and wood. The second part of this chapter highlights the mechanisms of biomass thermochemical degradation, from drying to gasification. In the third part, this chapter presents a review of the existing reactors used for biomass solar gasification. The last part of this chapter brings to light the existing model for biomass pyrolysis and gasification.

Chapter 2 deals with the experimental apparatus and data processing methods. It is broken into three thematics. The first one aims at describing extensively the new experimental device that was designed during this work. The second one focuses on a new method of flux mapping at the focal spot of a solar concentrating device that was developed in order to calibrate the new experimental apparatus. The last one deals with experimental procedure as well as data processing.

Chapter 3 describes the results obtained thanks to the experimental device. It reports an unseen behaviour of beech wood under high solar heat flux. Then, it describes the effect of two key parameters on biomass solar gasification: wood fiber orientation relative to the incident heat flux and wood initial moisture content. Finally, mass and energy balance closures are reported.

Chapter 4 deals with the numerical model of biomass pyro-gasification that was developed during this PhD. This chapter can be divided into three main parts. The first one presents the phenomena at stake and the assumptions that were made in order to model these phenomena. The second part reports the actual equations used to build the model. The last part explains special strategies that had to be used to describe the interaction between biomass and solar energy.

Chapter 5 presents the results produced by the numerical model. First, the validity of the assumptions made is verified and model predictions are compared to experimental observations. Then, the general behaviour of biomass under high solar heat flux is commented on. Further insights into the phenomena at stake are derived from the model predictions. Finally, the robustness of the choices made for the construction of the model are assessed through sensitivity analyses.

CHAPTER 1

State of the art

Introduction

This chapter aims at providing the required background for understanding the following work. It does not claim to be an extensive review of literature. The explored fields, i.e. solar energy and biomass conversion, are extremely wide. It would therefore be utopian to hope to review them here.

The first part introduces solar energy in terms of technology and potential. Then, it focuses on wood: its composition and properties. The concepts developed here will remain on the general level. The only aim is to familiarize the uninformed reader with knowledge of solar energy and wood.

The second part describes wood transformation with temperature. Indeed, our application temperature ranges from 20 °C to more than 1200 °C. Over this range, wood evolution can be broken down into three main steps: drying, pyrolysis and gasification.

The third part presents the past works in the field of biomass solar pyrolysis and gasification. Most of the studies focusing on biomass solar gasification were led at the reactor scale. It will be an opportunity to present the most conventional solar reactor designs. Studies at the sample scale are also reported. Yet, they remain scarce.

The last part of this chapter focuses on the modelling of the previously described phenomena. It presents the main description approaches that can be found in literature. When diverse approaches are available, the advantages and drawbacks of each are weighted.

1.1 Solar energy and wood

1.1.1 Solar energy: electricity and heat

The applications of solar can be divided into two main categories: producing electricity and producing heat. Among the challenges mankind faces in order to use this energy, storage is of note. Indeed, the incident solar power is intermittent. It varies from hour to hour because of the weather. It varies on a daily basis because of the day over night cycle. It also varies throughout the year and is not distributed uniformly on the planet.

There are two ways to convert sunlight into electricity. The first way is the use of photovoltaic panels. Photovoltaic panels use the ability of semiconductor, silicon most of the time, to absorb photons of specific wavelength and convert them into electrons. These panel produce direct-current electricity. Depending on its utilization, this electricity can be kept as it is or be transformed into alternative-current, to be sent on the grid, for instance. Photovoltaic installation size ranges from a few panels on a rooftop, producing a few kilowatts to large scale utility systems producing several megawatts. This versatility leads to a wide potential for installation in sunny

regions [26]. Photovoltaic electricity can be stored using hydroelectric energy storage or battery, yet progress remains to be done in this field of science.

The second way to produce electricity using solar energy is much more classical. Using a solar concentrating device, mirrors and/or lenses, solar beams are concentrated to produce intense heat. Industrially, heat flux above 1000 kW/m^2 (1000 suns) can be achieved. This heat is used to warm up a fluid, for instance steam. It is then recovered from the fluid and turned into electricity via a thermal energy conversion process, e.g. channelling it through a turbine in the case of steam. This last part is common with many other power plant technology. Concentrated Solar Power (CSP) plants usually are of large scale and feature storage tanks that allow to store the heated up fluids. This kind of storage allow CSP plants to face solar energy irregularity and enable them to produce electricity during the late afternoon and evening hours [27].

Process heat is the major consumer of the energy sector [26]. This heat can be divided into three categories depending on its temperature level:

- low temperature heat, below 100 °C. It is mainly used by the food, the textile and the chemical industries, for activities such as cleaning and drying. It represented 30 % of the heat used in Europe in 2005-2006
- medium temperature heat, above 100 °C and below 400 °C. The main users are still the food, the textile and the chemical industries. The activities are also similar as the one using low temperature heat: drying, cleaning, cooking. It accounted for 27 % of the heat used in Europe in 2005-2006
- high temperature heat, above 400 °C. It is used in a wide variety of industries working with high temperature processes; examples will be detailed below. It accounted for remaining 43 % of the heat used in Europe in 2005-2006

High temperature solar heat is of interest from an industrial point of view because is can easily reach fossil fuel firing temperatures without their drawbacks. Indeed, solar energy is clean in the sense that it does not add combustion residues to the process. This is why it is used to power pottery firing kilns. This heat can also be used to lead high temperature or highly endothermic processes that have an important carbon footprint, for instance the calcination reaction for lime production [28–31]. Finally, high temperature enable to break the water molecule into hydrogen and oxygen [5]. This could produce the hydrogen required by the rising number of fuel cell vehicles [26].

1.1.2 Wood: a complex material

Wood is a complex material that can be considered at several scales. At the molecular level, wood is mainly composed of three polymers: cellulose, hemicelluloses and lignin. In addition to them, water, mineral materials (also referred as *ash*) and low molecular weight organic species (referred as *extraneous materials*) can be found in the wood. The composition of wood in terms of cellulose, hemicelluloses and lignin

plays a major role in determining its properties [32].

Woods are classified into two board categories: *hardwoods* and *softwoods*. The differences between these two categories lies at the cellular scale (Fig. 1.1). Hardwoods contain wood cells with open ends. These cells stack on top of one another, forming a channel called a *vessel*. The vessels serve for sap transportation in the tree. Softwoods do not produce this type of cells, they therefore have no vessels. In softwoods, sap transportation is ensured by another type of channel, the *tracheids*, which are also present in hardwoods. Softwoods are therefore less porous than hardwoods.

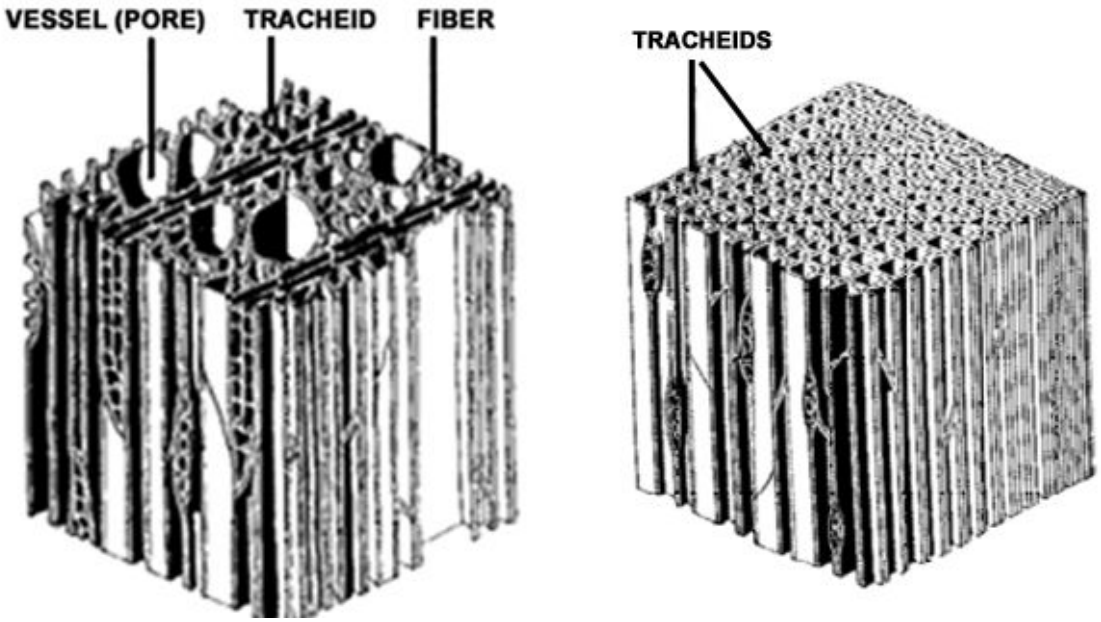

(A) Hardwoods (B) Softwoods

FIGURE 1.1: Hardwoods and softwoods anatomy [33]

At the macroscopic scale, wood can be considered as an homogeneous porous media with anisotropic physical properties. Indeed, transport properties of wood depend on the direction. It is easy to understand when considering that its structure is made of long parallel tubes. Three directions have to be considered: longitudinal (parallel to the fiber, the tree growth direction), radial (from the heart of the trunk toward the bark), orthoradial (perpendicular to longitudinal and radial). For a given wood structure, heat and mass transfers are favoured in the longitudinal direction. For instance, the longitudinal permeability is as much as five thousand times higher than the radial permeability [34]. Most of the time, radial and orthoradial properties can be assumed to be equal.

1.2 Biomass thermochemical conversion

With an increase in temperature wood undergoes several transformations (Fig. 1.2). The first one is drying, which takes place around 100 °C. Then comes torrefaction, close to 250 °C, which can be seen as the very beginning of pyrolysis. Even though this field of science receives more and more attention, it will not be considered in this review. From 400 °C to 800 °C, wood undergoes pyrolysis. During this transformation, it will turn into three main products: light gases, tar and char. Above 800 °C, char can be oxidized by steam and/or carbon dioxide to produce syngas. This step is referred as gasification. For further reading on biomass thermal degradation, one can refer to the pioneering work on Grønli [35].

FIGURE 1.2: The different steps of biomass degradation

1.2.1 Wood drying

Water can be found in wood under three forms: gaseous (water vapour), free liquid and bounded to the solid matrix (mainly to cellulose). At room temperature, water can move out of the wood porous matrix by diffusion. Around 100 °C, it is driven out by a pressure gradient induced by the boiling of liquid water. The distribution of water between these three forms is governed by a liquid-vapour equilibrium. Drying is the first major transformation undergone by the wood. This endothermic transformation is very complex. For the sake of simplicity, only drying near 100 °C will be considered. This type of drying is often referred as *high temperature drying*.

Consider a wood sample homogeneous in temperature. At 100 °C, and ambient pressure, liquid water inside of wood starts boiling. The pressure increases locally

and drives the steam out of the sample. Thus, water leaves the wood. Once all of the liquid water has been vaporised, bounded water starts separating from the wood matrix and evaporates until none remains. This is, of course, a simplified description. One should keep in mind that liquid and bounded water can move inside of the wood cavities [36]. Depending on the local temperature and pressure steam can condense. Furthermore, drying has an impact on the wood structure (contraction, distortions, cracks). It can locally lead to mechanical failure hindering the wood robustness [37–39].

High temperature drying has been shown to have an impact on the subsequent steps of biomass degradation. It modifies the yields of the pyrolysis step by increasing the proportions of light gases as well as char, therefore lowering tar production [21, 40]. This trend is consistent with an increase in wood initial moisture content: the more water, the more light gases and char are produced. Finally, the presence of water also changes the nature of produced tars. Indeed, the tar produced by pyrolysis after high temperature drying have been reported to be less acidic than those produced after a softer drying [40].

1.2.2 Pyrolysis

Pyrolysis takes place from 400 °C to 800 °C. During this transformation, the dry biomass polymers are broken down into a solid carbon residue called *char* and more than 300 different molecules [41]. These molecules can be sorted into two categories. *Light gases* (or simply *gas*) appellation covers the light hydrocarbons that remains gaseous at ambient temperature, usually from H_2 to C_3H_8. *Tar* encompass the remaining molecules that are gaseous at pyrolysis temperature, but liquid at room temperature. The proportions and compositions of these three products can vary depending on the pyrolysis conditions, for instance reported char yields range from 7 to 50 % [42, 43]. The three main factors influencing pyrolysis products distribution are: the pyrolysis final temperature and heating rate and biomass initial composition [41, 44–50]. The main trends are (Fig. 1.3):

- a high initial lignin content in wood leads to an increased char yield, while high cellulose and hemicellulose content lead to more important gas and tar yields [51–53]. Thus, hardwoods produce more gas and tar but less char than softwoods. Furthermore, minor components may also modify pyrolysis outcome. Alkali salts contained in wood ash tends to catalyse pyrolysis reactions and favour CO_2 production over CO [51, 54].

- the higher the heating rate, the more tar is produced. It is explained by the fact that at high heating rates, the produced tar are quickly expelled from the biomass. This prevents them from undergoing substantial cracking. However, low heating rate conditions can even allow for a tar to condense [55] which increases tar residence time inside of the sample and therefore their probability of undergoing cracking and repolymerisation. Liquid tar are called *intermediate*

liquid compound [22, 56] or *metaplastic phase* because of its very high viscosity [57].

- the higher the pyrolysis final temperature, the less tar is produced. Indeed, high temperatures favour tar decomposition into gas and char. This phenomenon is known as *tar thermal cracking*.

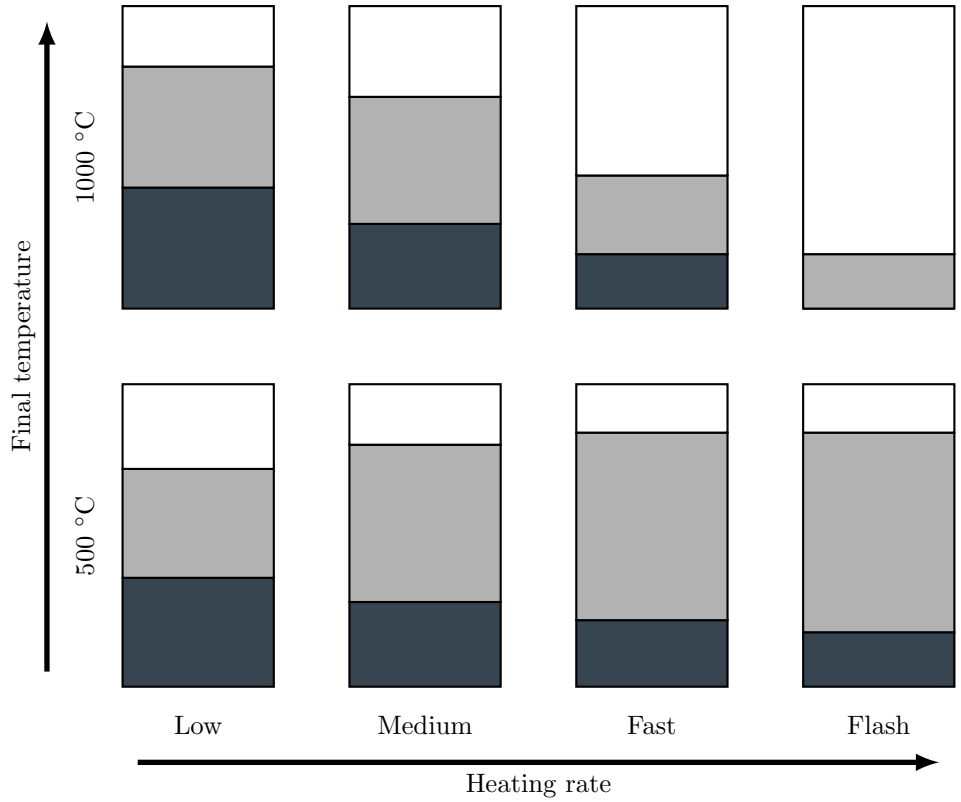

FIGURE 1.3: Pyrolysis products distribution [58]. Black: char, gray: tar, white: gas

In addition, it is commonly known that pyrolysis produces water. Yet, only few authors deal with water production during pyrolysis by considering it as an individual specie [59–63]. Most of the time, water produced by pyrolysis is taken into account as tar because it condenses at room temperature. It can be estimated that between 8 and 37 % of the initial dry biomass turns into water during pyrolysis.

As glimmered, pyrolysis is a complex and wide topic. In addition to the variety of its operating conditions, reviewing the subject is made even more difficult by the variety of feedstock (ranging from algae to tire scraps [64, 65]). Nevertheless, beech wood is the most commonly studied feedstock after coal. For the sake of readability, it was chosen to focus this review on fast pyrolysis of wood (heating rates higher than 100 K/min) and its impact on subsequent char gasification.

The way pyrolysis is led has an impact on gasification. It was shown that char reactivity during gasification varies depending on pyrolysis conditions. High heating rates tend to produce more reactive chars. These chars internal geometry offers

a higher specific surface area [46, 47, 49]. It is explained by the rapid escape of gas and tar from the sample preventing tar cracking reactions from occurring thus the deposit of char coming from tar repolymerisation reactions [23]. Their oxygen and hydrogen contents are also higher which indicates that more reaction sites are available for gasification [66].

High temperature and high pressure during pyrolysis tend to limit char reactivity. High temperature favours a reorganising of char matrix and pore coalescence. It decreases the number of reaction sites and specific surface area available for gasification [44, 50]. This phenomenon is referred as *thermal annealing*. High pressure during pyrolysis yields similar effect on char reactivity [67].

Solar heating allows to achieve high heating rates as well as high final temperatures. To this date, only one study has focused on the wood solar pyrolysis [25]. The authors focused on the chemical properties of char obtained by solar pyrolysis of beech wood pellets. They have shown that solar pyrolysis of wood leads to highly reactive char with high specific surface area. They also found the limit: final temperature above 1600 °C has an adverse effect on char reactivity, which can be explained by thermal annealing. Apart from this study, the behaviour of a biomass sample in itself under high solar heat flux remains unexplored.

1.2.3 Gasification of char

Gasification is a group of heterogeneous chemical reactions consuming carbonaceous feedstock. During gasification reactions, an oxidative reagent, most of the time steam and/or carbon dioxide, reacts with char to create hydrogen and carbon monoxide (Eq. 1.1 to 1.3). At the end of this stage, only syngas and ash remain.

$$C_s + H_2O \longrightarrow CO + H_2,\ \Delta H_{reac} = -131.1 \text{ kJ/mol, water reforming reaction} \quad (1.1)$$

$$C_s + CO_2 \longrightarrow 2CO,\ \Delta H_{reac} = -172.5 \text{ kJ/mol, Boudouard reaction} \quad (1.2)$$

$$C_s + 2H_2 \longrightarrow CH_4,\ \Delta H_{reac} = +74.4 \text{ kJ/mol, one of the methanation reactions} \quad (1.3)$$

$$CO + H_2O \longleftrightarrow CO_2 + H_2,\ \Delta H_{reac} = +41.1 \text{ kJ/mol, Water Gas Shift reaction} \quad (1.4)$$

Char-steam and char-carbon dioxide gasification are the ones that have been the most widely studied [7, 12–15, 17, 19, 43, 46, 47, 49, 68–71]. It has been highlighted that char-steam gasification is kinetically 2 to 5 times faster than char-carbon dioxide gasification. In addition, it yields a hydrogen richer syngas. Studies on the combined steam and carbon dioxide gasification have shown an interaction between the two reagents leading to a reaction rate higher than just the sum on the two individual ones [52, 72].

As discussed earlier, char reactivity is influenced by pyrolysis conditions: the higher the specific surface area, the higher the reaction rate. Minor species play an

important role in determining the gasification reaction rate. Alkali salts found in the wood can have a strong catalytic effect on the gasification reactions [47, 69, 70, 73], while silicon has an inhibitory effect [69].

1.2.4 Tar cracking and steam reforming

Tar produced by the pyrolysis of biomass are classified in two ways according to their molecular weight and their degree of breakdown. The first classification considers light, medium and heavy molecular weight tar. The second classifies tar as primary, secondary and tertiary tar depending on the extent of thermal cracking that they have undergone. Two broad kinds of tar breakdown reactions exist: thermal cracking and steam reforming. Both of them require temperatures higher than 800 °C to be of considerable importance.

Tar thermal cracking reactions breakdown the main part of medium and heavy tar into light tar (light aromatics) and gas. Some tar recombine to form thermally stable heavy tar (PolyAromatic Hydrocarbons or PAH), the *refractory tar* [74, 75]. This phenomenon grows in importance with an increase in temperature: 90 % of the tar produced by a pyrolysis at 600 °C have undergone thermal cracking once 1200 °C is reached.

Tar steam reforming includes a wide range of chemical reactions which transform tar into carbon monoxide and hydrogen (Eq. 1.5) [76, 77]. These are kinetically favoured by high temperatures; with temperature below 800 °C, only light and medium tar can be reformed, while temperatures above 1200 °C enable the reforming of the majority of the heavy tar.

$$C_xH_yO_z + (x-z)H_2O \longrightarrow xCO + (x-z+\frac{y}{2})H_2 \tag{1.5}$$

1.3 Solar reactors for biomass gasification

Solar pyrolysis and gasification have been led in a wide variety of reactor designs. The aim of these reactors is to offer the best heat transfer of the concentrated solar energy to the biomass, while controlling the reactive atmosphere. A review of the literature has recently been proposed [78].

- fluidized bed reactors are of interest because they can achieve a good thermal homogeneity and high heat exchange rates [23, 79]. Furthermore, ash can be added to the bed, hence, catalysing gasification reactions. These reactors also have drawbacks. Most of the time the steam used as fluidizing agent has to be injected in excess, hence, lowering the system efficiency. Fluidized bed reactors require a narrow particle size distribution of the input feedstock [12, 43] or the use of a fluidizing medium, such as sand [80]. Furthermore, this reactor design shows a poor capacity in cracking the tar [56]

- fixed bed reactors are well known and robust reactors [7, 12–14, 43, 47, 81]. Yet, their use for solar gasification exhibits a very specific problem. Gasification takes place on the top of the bed, at the focal spot, leaving only ash. Ash can accumulate here. Because of ash low absorptivity and thermal conductivity [81–83], it forms a radiative shield on the top of the bed which reduces the quantity of radiation absorbed by the reactor [12, 16, 43]

- vortex reactors expose the feedstock in suspension in a swirling vector gas [17–19, 28, 29]. The main drawback of this setup is the need for a very finely ground feedstock (< 200 μm)

- tubular reactors have also been used to lead a more unconventional type of char gasification: gasification in supercritical water [68, 73, 84]. The main advantage of this technique is that carbon dioxide dissolves into water, therefore facilitating the separation of syngas from other products

- rotary kilns reactors have also been used for both solar biomass gasification [56, 72] and limestone solar decarbonatation [30, 31]

Independent of the reactor design, the way in which the feedstock is exposed to the incident heat flux has an impact on the reactor behaviour. The first way is to directly expose the feedstock to the incident heat flux: the solar beams enter the reactor through a window and are directly absorbed by the reacting medium. The second way is to use an absorber heated up by the incident heat flux which emits part of the incident energy towards the inside of the reactor.

Direct heating allows to precisely locate the focal spot inside the reactor (Fig. 1.4 A). At the focal spot, very high heating rates can be achieved around 1000 K/s [7, 14, 17, 18, 56, 86]. A window is set through the aperture that the incident heat flux crosses in order to prevent the reagents or the products to freely escape the reactor and maintain a controlled atmosphere. This window induces a decrease of about 10 % of the maximum incident heat flux [87]. Furthermore, it needs to be protected from any soiling. Indeed, darking the window would increase its absorption of the incident power, increasing its temperature and potentially leading to its mechanical failure.

Indirect heating relies on an intermediary absorber that mediates the transfer of concentrated solar energy to the feedstock (Fig. 1.4 B) [12, 15, 43, 68, 72, 84]. The absorber makes uniform the emission inside of the reactor. It can also have a better spectral absorption than the feedstock, thus increasing solar energy absorption. Nevertheless, it induces heat losses by radiative emission towards the surrounding.

Regarding solar reactor design, it can be noted that the larger the reactor, the greater its thermal inertia. This is important for solar reactors because it enables them to keep working even without sun for a limited period of time [43].

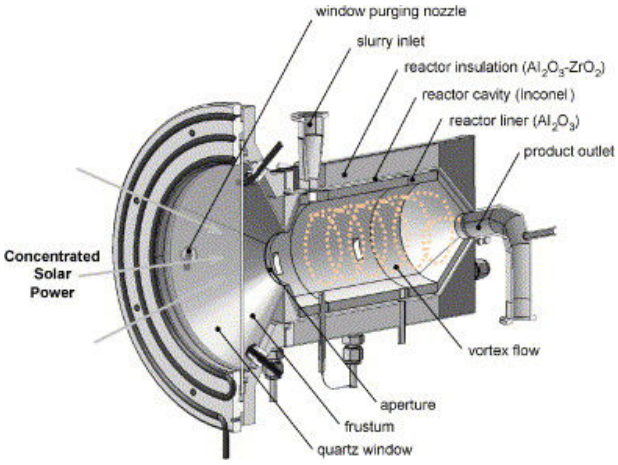

(A) A vortex reactor allowing direct heat of the feedstock [85]

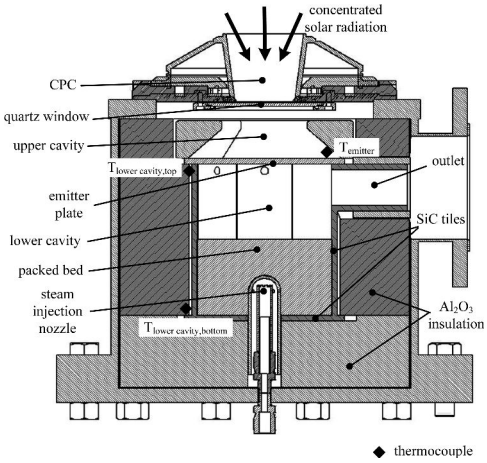

(B) A packed bed reactor equipped with an intermediary absorber [81]

FIGURE 1.4: Two reactor designs featuring direct and indirect feedstock heating

1.4 Modelling

Modelling each of the aforementioned phenomena is a challenge in itself. For each of them, several approaches exist depending on the needs it has to answer. It partly explains why there are only few attempts to build models that couple these complex phenomena [21, 88].

1.4.1 Drying

Three broad categories of models can be found in literature. The models of the first category take into account the actual liquid-vapour equilibrium [89]. These models can finely predict the transport of steam as well as free and bounded water. They are able to properly capture condensation. However, they have two limitations: their implementation might be challenging and their computational cost is much higher

than that of the other models.

The second kind of models, or Arrhenius type models, describe water vaporisation as a thermally activated phenomenon taking place around 100 °C [88, 90–93]. These models are used when drying is not the main focus of the study. Most of the time temperature of the medium will rise far above 100 °C. Hence, the model only aims at removing water from the medium. Nevertheless, some refinement might be added to them, by adding the possibility for steam to condense if the temperature is low enough [94].

The last type of models is referred as thermal models. They consider that drying take place at fixed temperature (usually 100 °C). If moisture is still present, all supply heat will be consumed by drying. Once moisture has been removed, the temperature is allowed to raise again. This kind of modelling induces sharp drying front that may lead to numerical problems [95].

For further detail on the methods used to model wood drying, one can refer to the discussion in [91].

1.4.2 Pyrolysis

Predicting the outcome of the pyrolysis of any feedstock is a particularly difficult task. As mentioned before, the parameters of influence are many and the expected products can be considered at different levels: mass dynamic and thermal behaviour of the sample or gaseous products composition.

Most of the models solve a heat and mass transfer problem coupled with biomass degradation. Some models neglect mass transfer [96] while others use a Darcy law to describe the gas flow inside of the sample. Authors generally do not discuss the possibility to correct Darcy's law using Forchheimer equation [97, 98] nor the possibility to use one or two temperatures approaches [99]. Furthermore, only few authors defend their assumptions. Very few authors use characteristic times approach to weigh the relative role of phenomena at stake beforehand [23, 100, 101], even less use dimensionless numbers [23].

Accurately describing biomass degradation into char, tar and gas is key [12, 88, 102, 103]. Indeed, poorly predicting biomass degradation leads to a biased prediction of the heat consumed by the biomass pyrolysis, having in turn an impact on the temperature field prediction, which controls biomass degradation.

Four main ways of describing biomass degradation exist; each consider biomass from a different point of view. The simplest models consider lumped species. These models can predict char, tar and gas yields, but not individual chemical molecules. Some can be basic [45] while others can feature tar cracking or intermediate species [104] (Fig. 1.5). Other models consider the biomass as a mixture of cellulose, hemicellulose and lignin. These models allow for a better prediction but require to

know the different product yields beforehand [105]. The third category are capable of predicting the production of individual species considering 10 to 50 chemical reactions, the most renowned being Ranzi model [106]. The last ones, referred as FG-DVC (for Functional Group-Depolymerization, Vaporisation, Crosslinking) were first used for coal pyrolysis prediction. They describe biomass cellulose, hemicelluloses and lignin as group monomers linked by chemical bonds. These models then predict depolymerisation and repolymerisation at the monomers level based on temperature and pressure conditions [107].

For all of these models, limitations exist. The main one is that they are validated against given sets of experimental measurements, making them depend on the conditions in which the experiments were conducted. For instance, a degradation scheme may yield very good predictions for slow, low temperature pyrolysis and be unable to properly predict the products distribution in the case fast, high temperature pyrolysis. Sadly, few experimental studies have dealt with combined high heating rate and high final temperature conditions [42]. Furthermore, to our knowledge, no biomass degradation scheme as been established for these particular conditions. This lack of studies might be explained by the adverse effect of high heating rate and high final temperature. It makes this configuration unappealing for both people who would like to maximise tar production or to enhance char yield.

Besides, biomass geometry changes during pyrolysis. The volume of the char residue is around 35 % of the volume of the initial sample [108, 109]. This change in geometry has an impact on heat and mass transfer through the sample, thus, modifying the pyrolysis products' distribution [110, 111]. Nevertheless, this phenomenon is neglected most of the time. It is only recently that some authors have been able to take it into account using a prescribed deformation method [88].

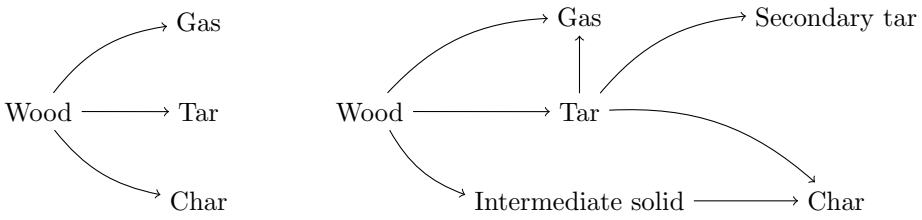

(A) A simple lumped species scheme [45]

(B) A more complex lumped specie scheme [103]

FIGURE 1.5: Different types of lumped species biomass degradation schemes

1.4.3 Gasification of char

There are two main interests behind modelling gasification reaction: predicting the products distribution and predicting the gasification reaction rate.

Predicting the distribution of the products of char gasification can been reasonably well done using the principle of minimum energy of Gibbs free energy [17, 52, 68]. This method assumes that the system has reached its thermodynamic equilibrium. It may not always be the case in actual reactors, yet this approach allows to draw a general behaviour: a higher temperature favours carbon monoxide and hydrogen over methane. Over 1100 °C, only carbon monoxide and hydrogen remain. Pressure has an adverse effect on hydrogen production. The higher the pressure, the more methane is produced.

Predicting char gasification reaction rate is a more challenging task. It can be undertaken at two levels: the particle scale in thermally thin thermogravimetric analyses or the reactor scale. The first one aims at better understanding the phenomena taking place during gasification, while the second produces kinetic parameters readily usable to describe feedstock behaviour inside a reactor.

As stated before, gasification heterogeneous reactions are influenced by oxidative atmosphere composition, sample specific surface area and mineral content. The chemistry at stake is quite complex. Proper description requires serial and parallel reactions, reactions between the products themselves, inhibitory effects of the products, catalytic effects of minerals and structure evolution [14, 19, 46, 47, 52, 71].

Simplified, macroscopic approaches have also been proposed. They aim at offering simple kinetic parameters that can be used to describe gasification reaction at the reactor scale [14, 112, 113]. These kinetics only consider the reaction rate dependency on the main oxidative reagent, i.e. steam or carbon dioxide. A review of the available kinetics can be found in [46].

Reactor scale modelling allows to compute species distribution in time and space [13, 15]. Numerous models have been proposed for reactor scale gasification [16, 114]. For more specific modelling of solar gasification reactors, one can refer to [7, 13, 15, 19, 43, 47, 68, 81].

Few authors have undertaken the modelling of the behaviour of a single thermally thick char sample undergoing gasification. Modelling such a phenomenon is challenging because the model has to take into account the deformation of the sample geometry. Indeed, in this configuration, the external layer of the reacting medium in consumed first while the core remains unconsumed. This configuration falls into the shrinking core model category which is known to be challenging to model using standard modelling approaches. Most of the proposed model are restricted to 1D configurations.

To this date, in the pyrolysis and gasification field, few models are able to describe such a phenomenon in 2D or 3D. Three of them are of note. The first one considers the gasification of a char pellet (agglomerated char particles) taking the fragmentation of the pellet into account [115]. The number of fragments produced by the pellet is prescribed, while their consumption is described using a phase function approach.

The second model describes the combustion of a biomass sphere in a grate furnace. The particle is decomposed into four layers that shrink as the biomass undergoes combustion. The last one describes the pyrolysis and ablation of the thermal shield of a space shuttle during is entry in the atmosphere [116]. Under these conditions, char is not ablated by gasification but by the high shear stress air flow. Nevertheless, the configurations are very similar. In this particular case, the deformation is not prescribed: front tracking method is coupled with Arbitrary Lagrangian Eulerian technique [117].

Conclusion

This chapter aimed at providing a basic background on solar energy and biomass thermal degradation. The key point of this chapter is that concentrated solar energy allows to produce high heat flux and to reach temperatures above 1200 °C. Exposing a wood sample to such a heat flux leads to its thermal degradation. The three main steps of this degradation are: drying, pyrolysis and gasification. These steps are complex in essence and influence one another. Only few experimental and numerical works report an in depth investigation of biomass behaviour under high solar heat flux. This PhD aims at contributing to the reduction of this gap in literature. After this literature review, beech wood (*Fagus sylvatica*) was chosen as the model biomass. Indeed, this feedstock is commonly used which has two considerable advantages: allowing for comparison with other studies and increasing the availability of thermophysical properties mandatory for numerical modelling. Given the chosen focus, i.e. thermally thick samples, this work may more easily apply to other technologies such as packed bed reactors or ablative heat shields.

CHAPTER 2

Materials and methods

Introduction

The following chapter describes the experimental device designed and the processing methods developed to explore the behaviour of beech wood under high solar heat flux. It can be divided into fives parts.

The first part sums up the objectives that were to be met by the experimental device and by the results processing methods. Two goals lie behind these objectives: better understanding of biomass behaviour by direct observation and producing results that will later be used to confront model predictions.

The second part presents the samples and their design strategy. Samples are thermally thick pieces of beech wood. Two sets of samples with two different fiber orientations relative to the incident heat flux are used in this study. Furthermore, initial moisture content of the samples is a key parameter and will therefore be varied.

The third part describes the experimental device in detail. It is composed of two different pieces: the reaction chamber and the radiative source. Building a device capable of exposing biomass to high radiative heat flux is known to be challenging. That is why, along with the description of the device, some problems faced during the conception are discussed and solution strategies are presented here.

Part four focuses on a particular problem that was faced during the conception of the experimental device: the calibration of the artificial sun. A new heat flux measurement method specific to high radiative heat flux mapping was developed [118]. This method is based on an inexpensive apparatus and basic inverse methods. They are used to compute the heat flux distribution from IR camera recordings. This technique is not specific to the experimental device developed in this work and could be used to calibrate any solar concentrating system.

The fifth part presents the experimental protocols that were followed for every run made.

The last part details the data processing methods that were used to derive information on the biomass behaviour from the measurements. Two processes are described: how pyrolysis yields are obtained from experimental data and how mass and energy balances are derived.

2.1 Objectives

The objectives that the experimental device had to meet fall into two categories: primary and secondary objectives. Primary objectives encompass the very basic features that allow for biomass exposure to high radiative heat flux.

The **primary objectives** are:

a. Exposing a thermally thick biomass sample to heat flux higher or equal to 1000 kW/m^2. Even though it seems really basic, this objective might turn out to be challenging. Indeed, reaching heat flux as high 1000 kW/m^2 is uncommon

b. Preventing the presence of oxygen in the vicinity of the sample. Given the level of temperature at stake during pyrolysis and gasification, oxygen would react with volatile matters and char. This combustion would bias the observations and induce safety problems

c. Avoiding the spoilage of the window crossed by the incident heat flux, in order to prevent its heating and mechanical failure. This constraint is identical to the one found in direct heating solar reactors

The secondary objectives have a wider scope. They cover additional features that allow further investigation of biomass behaviour and later confrontation of model predictions to experimental observations.

The **secondary objectives** are:

a. Following the sample mass throughout a run. It should, in principle, allow for the identification of phenomena by attributing to them a trend in the mass loss curve

b. Monitoring temperatures at the sample surface as well as inside the sample itself. Indeed, reported temperature levels are correlated to the phenomena at stake in the biomass degradation process

c. Computing sample transformation mass yields in terms of drying water, gas tar and char

d. Analysing gas composition

e. Analysing tar composition. This should allow to investigate tar thermal history, i.e. whether they have undergone thermal cracking or not

f. Establishing mass and energy balances of the system. Achieving closure would indeed be a token of the quality of the experiments

2.2 Samples

The samples were first designed then characterized. The objective lying behind the sample design is to explore as much as possible biomass behaviour under high solar heat flux. As identified before, sample fiber orientation relative to the incident heat flux may be a key parameter, as well as its initial moisture content. Samples were made out of beech wood only. The influence of wood type was not studied in this work.

2.2.1 Samples design

The sample design faces two major constraints: producing thermally thick sample and allowing to easily model the sample geometry. As the first constraint is obvious, the second is more subtle. Because of the wood anisotropy and the scale of the study, i.e. the sample scale, it is important to anticipate how to model the feedstock. Indeed, if the wood fibers are randomly oriented from sample to sample, the future numerical model should be able to handle this problem. In order to facilitate modelling of the sample, it was chosen to first work with wood cylinders whose fibers are parallel to the revolution axis of the cylinder (Fig. 2.1). The top surface of the cylinders would be exposed to the incident heat flux. Hence, this configuration would allow for a 2D axysymmetrical modelling of the sample geometry under the assumption that radial and orthoradial physical properties of the wood are equal. Such samples fall into the special category of wood pieces: *bois de bout*. Bois de bout are pieces for which a special care is taken so that the wood fibers would be perpendicular to a desired surface, in our case the top and bottom surfaces of the cylinder.

The sample size was determined using a *pre-model*[1] of biomass thermal degradation. The design criterion was that the lateral and bottom surfaces of the sample temperature would not exceed 50 °C after a 5 minutes exposure. This design procedure leads to the choice of 10 cm diameter, 5 cm high samples.

Bois de bout samples represent a very specific configuration; it would be bold to think that this configuration is representative of the behaviour of biomass under high solar heat flux whatever the orientation of the wood fibers relative to the incident heat flux. So, in order to assess this configuration impact, another set of samples was prepared: *bois de fil* samples (Fig. 2.1). Bois de fil samples have their fibers perpendicular to the cylinder revolution axis. They can be seen as the extreme opposite of bois de bout samples in terms of fiber orientation.

For practical reasons, it was not possible to carve bois de bout and bout de fil samples out of the same tree. Tree composition can vary depending on where it grew or the weather it was exposed to. In order to assess the potential differences between the two used trees, proximate and ultimate analysis (Tables 2.1 and 2.2, see next section) can be used. The results between the two beech woods are very close and in good agreement with values reported in literature [119]. The samples can therefore be considered to be made of the same material.

One should note that the modelling of bois de fil samples is not possible using a 2D axisymmetrical geometry. They indeed require to be described using 3D geometry.

[1] This numerical model describes beech wood drying and pyrolysis. It was implemented under Comsol. This model was used during the experimental device design stages for sizing purposes. Yet, because of this software intrinsic limitations, its development was stopped in favour of an implementation of the model using OpenFOAM CFD toolbox.

(A) Bois de bout top view

(B) Bois de fil top view

(C) Bois de bout side view

(D) Bois de fil side view

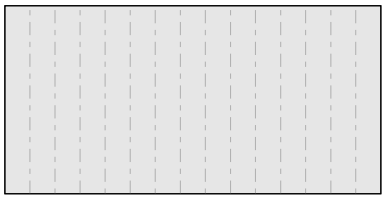

(E) Bois de bout side view schematic

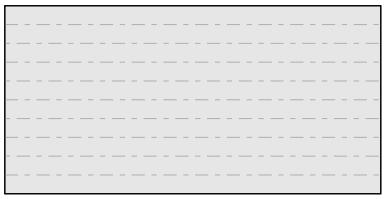

(F) Bois de fil view schematic

FIGURE 2.1: Sample views

2.2.2 Samples properties

Samples were characterized in terms of volatile matters, char and ash by a proximate analysis (Table 2.1) and in terms of carbon, hydrogen, oxygen, nitrogen and sulphur composition by an ultimate analysis (Table 2.2).

Three different moisture contents were used for the experiments:

- 0 %wb samples were oven dried until their mass stabilized
- 9 %wb samples have been several months under room conditions so that their water content stabilized. It is the state of the wood that has been stored for two years outdoor (commonly referred as *dry wood*)
- 55 %wb samples were vacuum pumped and impregnated in water until their mass stabilized. They were prepared to be a representative state of the wood after cutting

	Bois de bout	Bois de fil
Volatile matters	15.2	14.2
Char	84.3	85.0
Ash	0.5	0.8

TABLE 2.1: Wood proximate analysis (%wt)

	Bois de bout	Bois de fil
Carbon	48.78	49.96
Hydrogen	5.98	5.62
Oxygen	43.93	44.10
Nitrogen	0.35	0.32
Sulphur	0.96	-

TABLE 2.2: Wood ultimate analysis (%wt)

A change in wood moisture content induces a change in its geometry. Drying induces shrinkage, while water impregnation induces swelling. Because of the induced swelling or shrinkage, the wood density varies with moisture content. By measuring sample mass and volume, it is possible to calculate its apparent density. Table 2.3 reports the different wood apparent density and porosity assuming beech wood bulk density being 1500 kg/m^3 [120, 121]. These measurements were repeated at least 6 times in order to derive a standard deviation.

Moisture content	Density (kg/m^3)	Porosity (%)
0 %wb	652 $\pm$ 40	57 $\pm$ 2.6
9 %wb	579 $\pm$ 38	61 $\pm$ 2.6
55 %wb	535 $\pm$ 8.0	65 $\pm$ 1.2

TABLE 2.3: Sample density and porosity versus moisture content

Sample spectral properties are also of importance. Indeed, they govern the amount of radiative energy that is absorbed and emitted by the sample. Beech wood reflectivity was measured for both bois de bout and bois de fil configurations (Fig. 2.2). Furthermore, given the fact that the sample will undergo pyrolysis, after a few seconds the exposed surface will be made of char and not wood. Char reflectivity was therefore also measured (Fig. 2.2). Finally, the absorptivities of the materials were computed with respect to the lamp spectrum (see Section 2.3.2). Bois de bout and bois de fil have the same absorptivity of 0.37, while char absorptivity is 0.88.

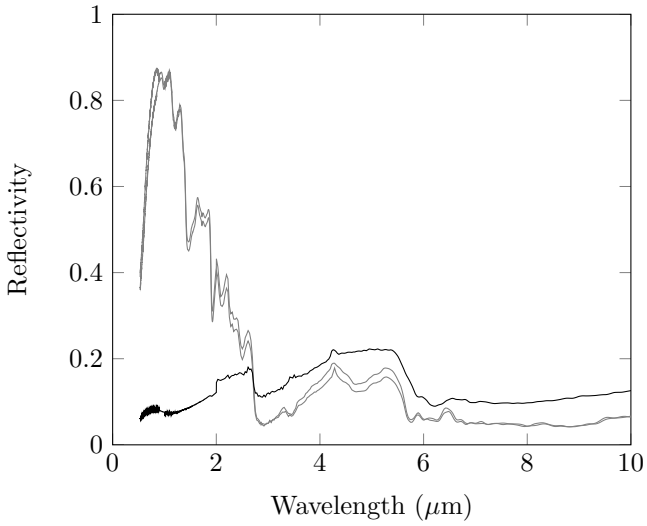

FIGURE 2.2: Beech wood and char reflectivities. Gray lines: beech wood, black line: char

2.3 Experimental apparatus

During a run, the sample is placed in an enclosure referred to as the *reaction chamber*. The reaction chamber allows to expose the sample to the concentrated solar heat flux. It also ensures that no oxygen is allowed in the vicinity of the sample, monitors sample mass and temperature, captures tar and permits to analyse the gas.

For this study, no solar concentrating system was readily available. Therefore an artificial sun was used instead. This kind of radiative source has long been used to emulate solar energy in terms of density and spectrum. They are now becoming more and more widespread because they allow to study high temperature phenomena [28, 87, 122, 123] without suffering from the main drawback of solar energy, i.e. intermittence. The applications of this kind of device were recently and extensively reviewed in [124]. One should note that these devices are also referred to as *image furnaces*.

The reaction chamber is positioned on a scale (Fig. 2.3). Special care was taken in ensuring scale stability. It was placed on a massive independent stainless steel table so that it is not subject to vibrations. Furthermore, the artificial sun is placed above the reaction chamber, yet, no contact point exists between the two.

The reaction chamber is described first, then the radiative heat source is presented.

2.3.1 Reaction chamber

The objectives of the reaction chamber are numerous. The main idea behind the reaction chamber design (Fig. 2.4 and 2.5) is that: placing the sample in a swept channel allows to expose the sample through a windowed aperture, evacuate the

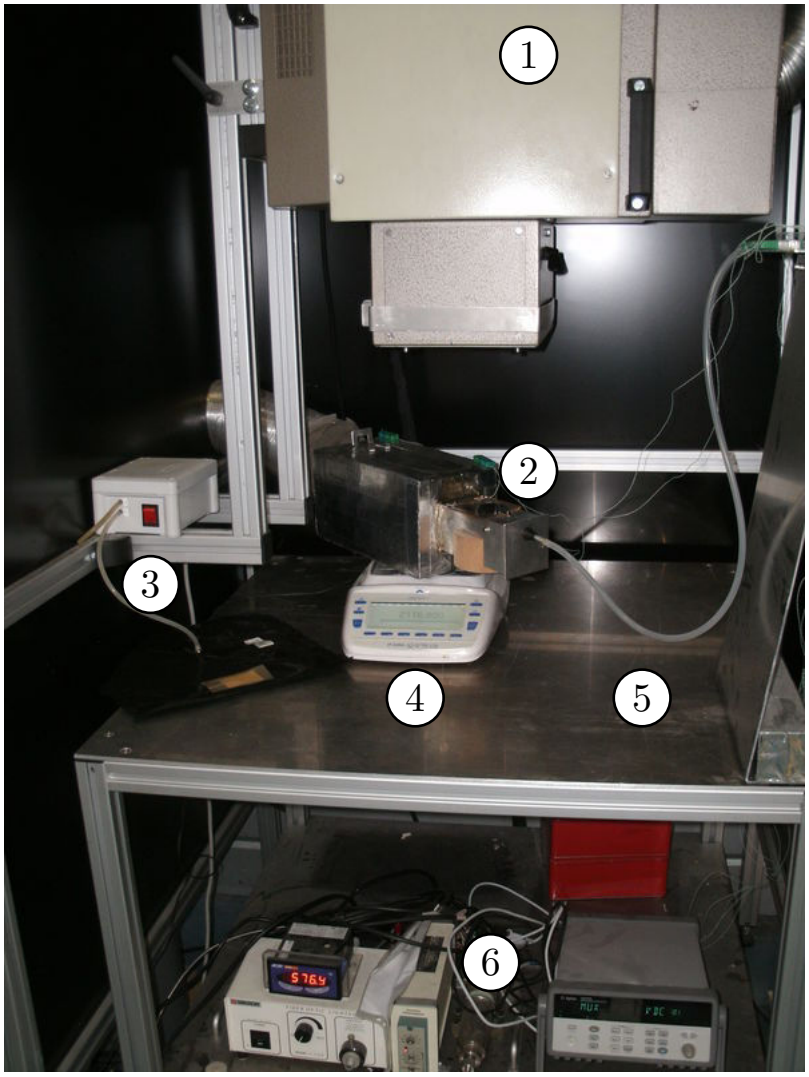

FIGURE 2.3: Picture of the experimental device. 1: artificial sun, 2: reaction chamber, 3: gas sampling device, 4: scale, 5: stainless steel table, 6: temperature recording devices

produced gas and tar, condense the tar just downstream of the sample in a condenser and analyse the remaining gas. The following parts describe how the reaction chamber fulfils these objectives.

2.3.1.1 Controlling the atmosphere and exposing the sample

The atmosphere around the sample can be easily controlled by sweeping it with an inert gas such as nitrogen. Furthermore, purging the reaction chamber with more than 10 times its volume before a run would ensure that no oxygen remains in the vicinity of the sample.

The reaction chamber has to allow for a continuous exposure of the sample throughout a 5 minutes run. The main problem is that, while undergoing pyrolysis, the sample produces abruptly gas and tar. Because of wood fiber orientation, these

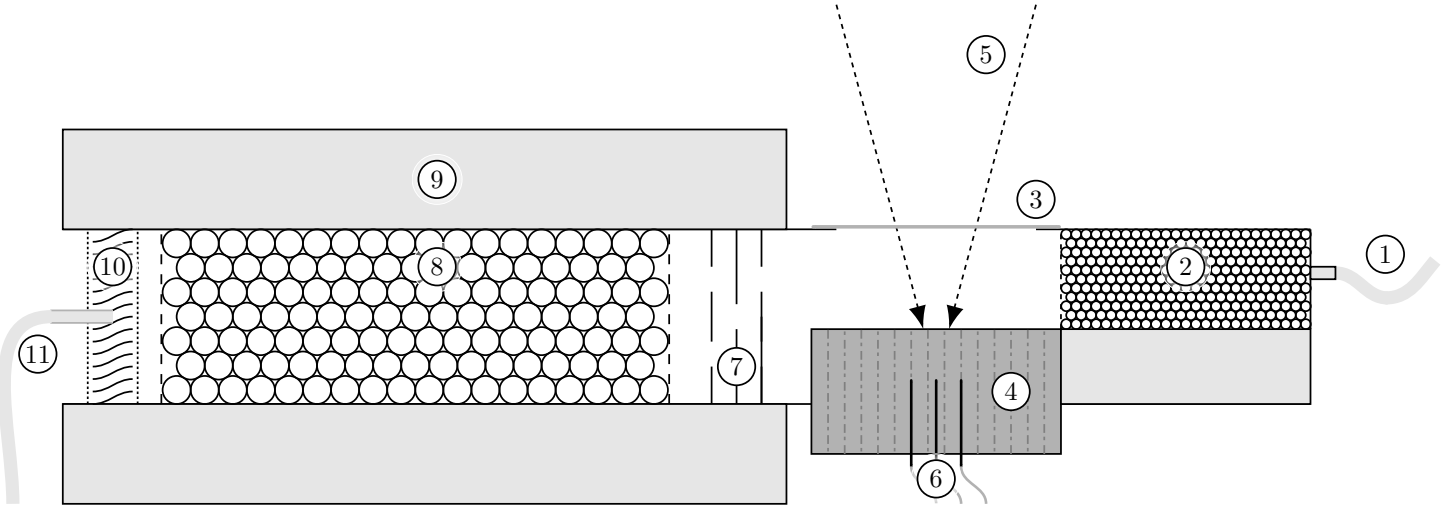

FIGURE 2.4: Schematic of the reaction chamber. 1: nitrogen inlet, 2: porous medium, 3: quartz window, 4: sample, 5: incident heat flux, 6: thermocouples, 7: static mixer, 8: condenser, 9: insulating material, 10: cotton trap, 11: gas sampling probe

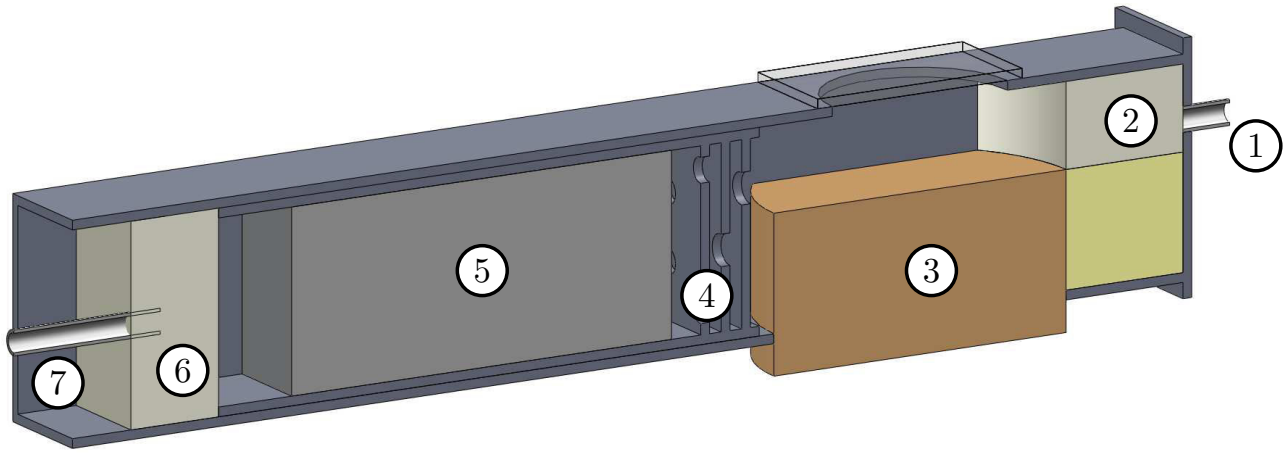

FIGURE 2.5: Schematic of the reaction chamber, cut view, without insulating material. 1: nitrogen inlet, 2: porous medium, 3: sample, 4: static mixer, 5: condenser, 6: cotton trap, 7: gas sampling probe

gases are expelled toward the quartz window. If the tar would come in contact with the window, they would undergo thermal cracking and leave a carbon layer on the window. It would increase the window absorptivity, hence its temperature, and quickly lead to its mechanical failure, allowing oxygen to enter the reaction chamber.

In order to prevent this kind of incident from happening, the nitrogen sweep flow rate has to be high enough to drive gas and tar away from the window. Yet, the flow should be laminar in order to prevent turbulent mixing. Furthermore, it was also thought that maximizing sweeping flow shear stress on the sample surface would further increase its capability to drive away the produced gas and tar (Fig. 2.6). Hence, a porous medium was set on the sweeping flow trajectory upstream to the

sample, so that a sweeping flow would be in a laminar plug flow configuration upon reaching the sample. In order to save the time and cost of a trial and error approach, this concept was first tested using numerical models: the pyrolysis pre-model produced the gas and tar flow rate expelled by the sample. Fluent was used to calculate the required nitrogen flow rate and the porous media length so that the window would stay clean. Numerical design advised a sweeping flow rate of 60 l/min. Experiments showed it could be safely lowered to 40 l/min. Lowering the sweeping gas flow rate comes with advantages: produced gases are less diluted which facilitates its analysis, reducing the condenser payload (Section 2.3.1.2) and being more cost efficient. Therefore, the nitrogen flow rate was set to 40 l/min for all experiments using a mass flow meter and a controller.

The porous medium is a packed bed of 2 mm diameter alumina spheres. It has been observed that these spheres absorb water contained in air. Therefore, this porous medium should be dried before a run in order to prevent its drying from biasing the mass monitoring.

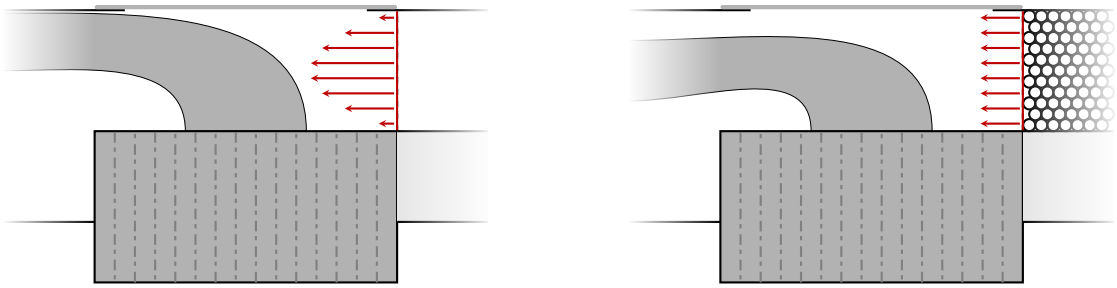

(A) Poiseuille flow (B) Plug flow

FIGURE 2.6: Nitrogen sweeping flow configurations

2.3.1.2 Condenser

Once driven away from the sample, the gas, tar and water are forced into a tar and water condensing device referred to as *condenser*. This condenser aims at capturing all the tar and water produced by the sample during a run. Hence, the downstream flow would be free of tar and water. It could thus be analysed for gas composition. Regarding water, one point arises. Water stopped by the condenser is the sum of water coming from the sample drying as well as the water produced by the pyrolysis. In this study, water produced by the pyrolysis will be accounted as tar. *Water* will refer to the water coming from the sample drying.

The condenser takes advantage of the fact that tar is by definition a liquid at room temperature. By lowering the flow temperature below 0 °C, tar and water condense into small droplets. These droplets can then be captured using a cotton filter. To ensure that tar condenses throughout a run, the condenser temperature has to remain below 0 °C. This could be achieved in two ways: by continuously cooling

the condenser or by cooling the condenser before the start of a run at a temperature low enough so that it would not reach 0 °C before the end of that run. These two methods have their own drawbacks. The first one implies supplying cool liquid to the condenser and therefore hanging tubes from the reaction chamber. This might be a problem for the continuous weighing of the reaction chamber (Section 2.3.1.4). The second implies that the condenser would be efficient only for a certain amount of time. The second method was thought to be the best. Thus, a transient condenser was designed for 5 minutes run.

The condenser is removable, so that it can be immersed in cold liquid before a run. Liquid nitrogen was chosen as cooling medium (77 K, or -196 °C). For convenience sake, the condenser should not be too heavy. Hence, its volumetric heat capacity has to be high enough so that enough negative calories could be stored for a run. After a search, it was found that aluminium was the best available solution because of its high heat capacity, low density, thermal stability and availability. Hence, the condenser was made out of aluminium.

The main part of the condenser is a porous media made of aluminium spheres. This design was chosen because it enables a good solid gas contact and a low pressure drop. The main fraction of the negative calories is stored in the aluminium spheres. Upstream of the aluminium spheres packing is a static mixer made of a set of unevenly perforated plates. Indeed, the sweeping flow being laminar, hot tar, water and gas do not mix with nitrogen. If sent with no mixing inside of the condenser, this hot core flow would heat up only the central part of the condenser, leaving the lateral parts as thermally dead volume (Fig. 2.7). Downstream of the aluminium spheres is a cotton trap. This trap is set to capture tar droplets and aerosols escaping the condenser. Indeed, preliminary runs have shown that the aluminium spheres do not intercept all of the tar droplets. It was therefore mandatory to place a filter to stop them.

Finally, the reaction chamber was surrounded by insulating material in order to prevent water contained in air to condense on the reaction chamber outer surface near the condenser.

2.3.1.3 Gas and tar analysis

A continuous gas analysis throughout a run was too complex. It was chosen to resort on batch sampling. Three gas samples were taken at the outlet of the cotton trap over different time laps during a run: t = 0 to 1 minute, 2 to 3 minutes and 4 to 5 minutes. Gas were stored in Tedlar bags and then analyzed using a microGC. The reported species are: H_2, CO, CO_2, CH_4, C_2H_2, C_3H_8, C_2H_6 and C_2H_4. These species are thought to represent more than 95 % of the gas emission [100, 125]. Because of the sweeping flow, these species are diluted by nitrogen. Nitrogen represents 90 %vol of the analyzed gas feed, which is low enough not to hinder measurements quality.

In addition to providing the gas composition, gas analysis is a way of computing

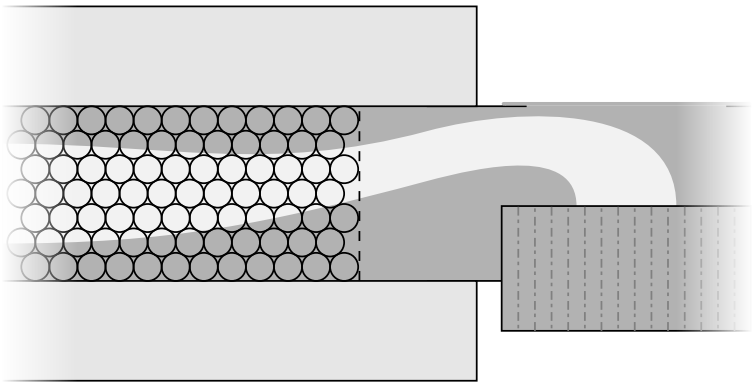

(A) Without static mixer

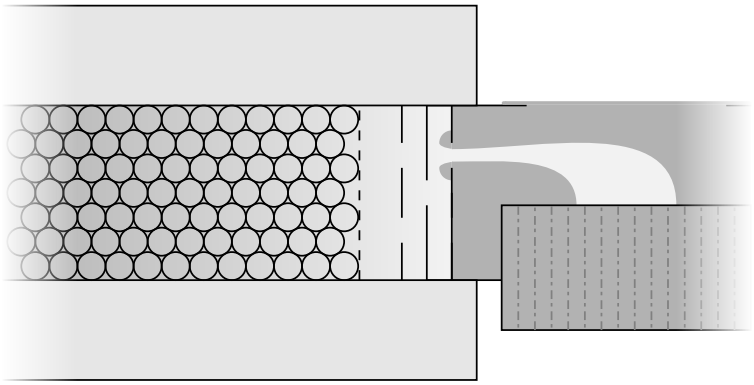

(B) With static mixer

FIGURE 2.7: Schematic of the flow pattern inside of the condenser

sample gas yield. Indeed, average gas composition can be also used to calculate the average gas production rate. As the nitrogen flow rate and the stream composition are known, it is possible to compute the average gas flow rate and thus sample gas production rate.

Cotton containing tar was stored in air tight boxes and sent to CIRAD laboratory for tar composition analysis. Tar was desorbed in acetone before being analysed using gas chromatography coupled with mass spectrometry. Four analyses were performed: tar produced by bois de bout sample for the three initial moisture contents. 9 %wb initial moisture content samples tar were analysed twice in order to assess the run to run repeatability of the results.

2.3.1.4 Mass and temperature monitoring

During a run, the whole system is weighed using a scale. Therefore, the system mass loss can be accounted for. A bichromatic radiometer is set in such a way that it measures sample surface temperature at the focal spot. A set of three thermocouples is placed inside of the sample in order to monitor its core temperature.

A Precisa EP 2220M scale was used to monitor the reaction chamber mass. It has a range of 2.220 kg and a precision of 1 mg. In order not to perturb the mass signal, special care was taken in using long, loose and flexible cables for thermocouples connections and nitrogen feeding. Because the condenser is removable, the scale can be used to determine different quantities:

- when the condenser is not fitted into the reaction chamber, gas, tar and water freely escape the reaction chamber. Under these conditions, the mass signal accounts for the sample mass loss evolution
- when the condenser is fitted into the reaction chamber, tar and water are stopped. Therefore, only gas escapes the system. The mass signal only accounts for the gas production rate

As a complement to continuous mass monitoring, mass measurements were taken before and after a run. They allow to calculate wood consumption, water, char, gas and tar average production rates. Before a run, sample mass $m_{sample,\ ini}$ and reaction chamber mass $m_{chamber,\ ini}$ were measured. After a run, sample mass $m_{sample,\ fin}$ and reaction chamber mass $m_{chamber,\ fin}$ were measured again. Exposed samples contain a char residue produced by pyrolysis which was not consumed by gasification (Fig. 2.8). This char was scratched away from the sample and its mass m_{char} was taken. Then, the void left by the char was filled with thin sand in order to measure the volume of the crater in the wood. The mass of this sand m_{sand} was taken. Knowing, the sand and the wood density, it is possible using Eq. 2.1 to determine the mass of wood m_{wood} consumed during a run.

$$m_{wood} = m_{sand}\frac{\rho_{wood}}{\rho_{sand}} \tag{2.1}$$

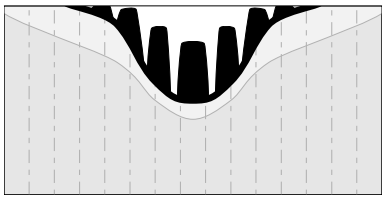

FIGURE 2.8: Schematic cut view of a sample after exposure. Dark gray: moist wood area, light gray: dry wood area, black: char residue

Sand density was measured every day, right before using it to measure the crater volume. Indeed, sand is an hygroscopic material and could therefore absorb water which would change its density.

In addition to mass measurements, temperatures were also recorded. Holes were drilled into the samples and type K and S thermocouples were used to monitor temperatures at several points inside of the samples. The thermocouples were placed 2 cm below the exposed surface one on the sample revolution axis and two 1 cm away from the axis (Fig. 2.4). Surface temperature was also monitored using a

bichromatic radiometer. Its measurement capacity ranges from 600 to 1800 °C. Finally, a thermocouple was set at the outlet of the reaction chamber, so that outlet flow temperature could be monitored.

2.3.2 The radiation source: an artificial sun

Artificial suns are basically made of xenon arc lamp and a concentrating mirror (Fig. 2.9). The lamp is placed at the first focal point of an elliptical mirror. The mirror intercepts the radiation coming from the lamp and redirects it toward its second focal point. The system is enclosed in a casing for both safety and technical reasons. Firstly, because the lamp produces very intense radiations that can damage the eyes of the people looking at it. Secondly, the whole system dissipates a tremendous amount of heat. Half of the lamp electric consumption is directly converted to heat and half of the produced radiation (one quarter of the lamp electric consumption) is intercepted by the casing. Air fans are used to remove this heat. The casing helps to properly direct the air flow around the lamp. Furthermore, a shutter is placed on the casing so that exposure can be controlled without turning on and off the lamp.

In our case, a former cinema lantern was used as casing. Inside of it, a 4 kWe lamp xenon arc lamp (OSRAM XBO 4000 W/HS) was used. According to the manufacturer, the efficiency of the conversion to radiation is about 50 %. In order to intercept the maximum amount of radiation, the largest mirror available was used (semi major axis: 430 mm, semi minor axis: 205 mm). It has a 12.98° aperture angle. This aluminium coated mirror was supplied by Edmund Optics (Ref. 90-972).

The spectrum of the radiation coming out of the casing was measured using Ocean Optics USB2000 spectrometer (Fig. 2.10). It can be seen that the incident radiation spectral distribution is close to the solar spectrum at sea level through one air mass. Both distributions exhibit a thermal continuum, yet they differ by some absorption and emission band associated to gases. The spectrum produced by the artificial sun is slightly shifted toward low wavelength and features emission rays of xenon between 400 and 600 nm. While solar spectrum features absorption rays of H_2O and CO_2.

Determining the incident heat flux at the focal spot of the artificial sun is a challenging task. This problem has been approached using various methods. In some cases a radiometer [127] or equivalent [128] is used to map the focal spot. This method is time consuming and offers a low spatial resolution map. Yet, it yields an absolute value of the incident heat flux and requires no external scaling factor. In other cases a CCD camera is used to record a gray value image of a water-cooled target [123, 124]. Then using an external measurement, often a radiometer reading, a scaling factor is applied to the recorded image. This method allows for a high resolution but relies entirely on the external scaling factor and the use of a high-end water-cooled target. One last way of mapping the heat flux distribution is to run

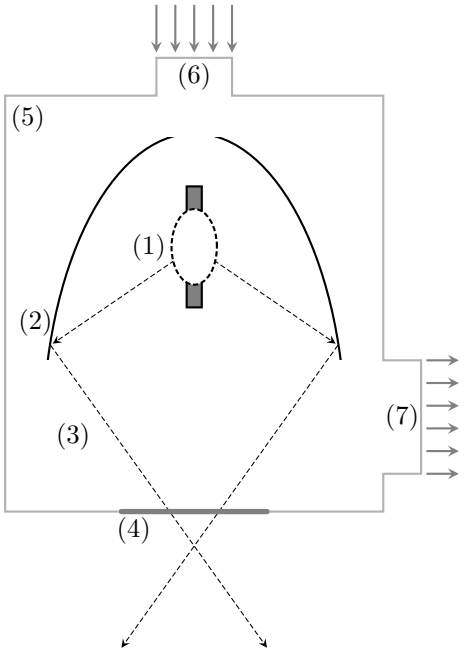

FIGURE 2.9: Schematic of the artificial sun. 1: 4 kW xenon arc lamp, 2: elliptical mirror, 3: a ray, 4: shutter, 5: casing, 6: air inflow, 7: air outflow

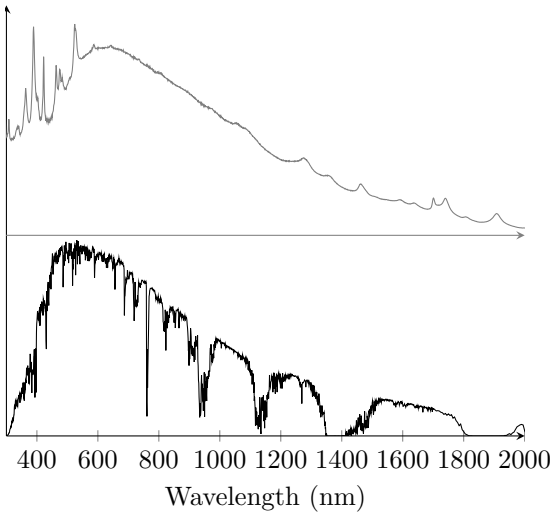

FIGURE 2.10: Power spectral distribution (y axis: arbitrary units). Black: solar spectrum at sea level through 1 air mass [126], gray: incident radiation spectrum

the device at minimal power, for example using the moon instead of the sun for an outdoor dish [129]. Pictures can be taken and processed to yield high resolution incident heat flux map. Then, the actual map can be computed using the ratio of the two source powers. Sadly, this is not possible for certain devices such as xenon arc lamps because their minimal power is very close to their nominal operating condition.

The former methods being out of reach, it was therefore mandatory to develop a new method that would allow to map the incident heat flux distribution at the focal

spot of solar concentrating systems.

2.4 Artificial sun calibration

The idea behind the method[2] that is described in this section is quite simple. It is thought that by placing a screen on the artificial sun beams trajectory and monitoring its warming up, it would be possible to determine the incident heat flux intercepted by the screen.

Heat flux distribution mapping is a widespread problem that can be found in numerous industrial situations. Among the various methods that have been developed for the determination of the incident heat flux, the inverse methods are of particular interest. Inverse methods associate a problem, a mathematical model and experimental measurements to compute quantities of interest. They adopt a reverse point of view in comparison to the classical approaches. For example, a classical heat transfer problem is the determination of a temperature field from known boundary condition, heat source and material properties. This is called a direct problem. On the contrary, an inverse problem is the determination of boundary conditions, heat source and/or material properties from temperature measurements. A model linking the measurements to the desired value is built; it is called an inverse model. This approach has been applied with success to a wide variety of problems, such as the design of insulation protection [130], or the sizing of a heat exchanger [131].

The following sections present: the experimental setup used to collect data, the mathematical treatment of the data and the results, i.e. the heat flux distribution.

2.4.1 Experimental setup

To map the incident heat flux, a screen is set in front of the artificial sun (Fig. 2.11). Thus, the beams coming out of it are intercepted by the screen. As beams energy is absorbed by the screen, its temperature rises. The temperature variations are recorded by a 320x240 IR camera with a working range between 8 and 12 μm. Screen exposure is controlled by a shutter placed on the light trajectory before the focal spot. The focal spot of this device is known to be 32 cm away from the lamp house casing.

In order to have a flat emissivity of 0.79 in the camera working range, one side of the screen was painted with a black paint. Temperature was monitored on the painted side of the screen. Far from the focal spot, the painted side of the screen was illuminated (Fig. 2.11). At the focal spot, the bare steel side of the screen was illuminated reducing the absorbed energy by a factor of about 2 (Fig. 2.12).

[2] This method was published in *Solar Energy* journal (*DOI: 10.1016/j.solener.2015.04.021*). It is reproduced with the editor authorisation.

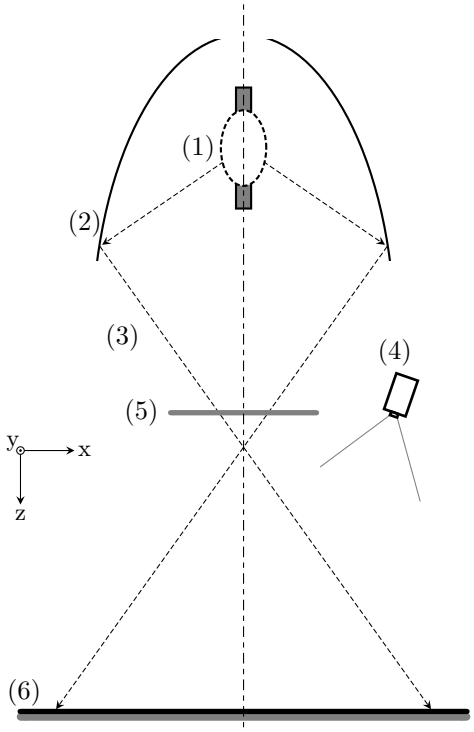

FIGURE 2.11: Calibration apparatus schematics, defocused configuration. 1: 4 kWe xenon arc lamp, 2: elliptical mirror, 3: a ray, 4: camera, 5: shutter, 6: screen, black line: paint

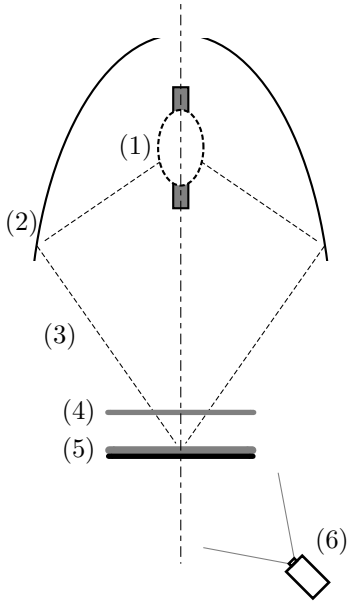

FIGURE 2.12: Calibration apparatus schematics, focal spot configuration. 1: 4 kWe xenon arc lamp, 2: elliptical mirror, 3: a ray, 4: shutter, 5: screen, 6: camera, black line: paint

2.4.2 Experimental procedure

The proposed inverse method requires transient screen temperature measurements. Indeed, it uses the recording of the screen temperature elevation to yield a map of the incident heat flux. Incident heat flux is mapped at the focal spot and also at several distances from the focal spot: 50, 75, 100, 125 and 150 cm. Focal spot measurements are the one of interest here. Indeed, they will allow to compute the incident heat flux on the sample. More specifically, what is of interest is focal spot measurements with the quartz window of the reaction chamber. Under these conditions, two types of focal spot mapping are produced: with and without additional quartz window on the beams trajectory. Measurements with the window yield the heat flux distribution on the sample. While measurements without the window are combined with those far from the focal spot to assess beam energy conservation over the distance. Furthermore, measurements far from the focal spot can be compared with Gardon radiometer readings for comparison. In order to assess repeatability, each measurement was repeated twice.

For every run the following experimental procedure was observed:

- the screen and the camera are positioned
- the shutter is closed
- lamp is turned on
- 10 minutes are allowed for the lamp and lamp house to be thermally stable
- the camera is started
- the shutter is opened
- the acquisition is turned off once critical temperatures are reached
- the shutter is closed

2.4.3 Experimental precautions

Because the camera was off the optical axis of the system, the pictures had to be corrected using a projective transformation before computing the incident heat flux.

In order to later simplify the problem, the screens were chosen to be thin and made out of a conductive material, so that temperature is almost constant along their thickness. Here, a 0.8 mm thick stainless steel square plate (304L steel) was used to produce the screens.

In cases where the screen is far from the focal spot (Fig. 2.11), its temperature does not increase much and its physical properties are assumed to remain constant. This assumption implies that the screen temperature does not increase beyond reasonable bounds: 80 °C. This temperature was chosen to keep the screen thermal conductivity variation below 10 %. In this configuration, under moderate heat flux,

the exposed side of the screen is painted in black.

At the focal spot (Fig. 2.12), screen temperature increases sharply up to 300 °C within 3 seconds after which acquisition is stopped. Screen physical properties variations was taken into account. Bare steel was exposed to incident heat flux, in order to take advantage of its reduced surface absorptivity and reduce the temperature increase speed so that enough frames could be acquired before the screen reached 300 °C. Temperature was monitored on the other side that was painted in black.

A Gardon radiometer was used to measure incident heat flux on the screen at different positions. These measurements allowed to validate the inverse method results.

In our problem, it is critical to know several key spectral properties: the screen absorptivities with respect to the lamp spectrum and the screen emissivity with respect to the camera range. These properties were measured using a spectrometer and are available in Table 2.4.

Symbol	Property	Value	Dimension
α_p	Paint absorptivity	0.90	-
α_{st}	Steel absorptivity	0.48	-
ϵ_p	Paint emissivity	0.79	-
ϵ_{st}	Steel emissivity	0.48	-
ρ_s	Steel density	7900	kg/m^3
$\lambda_{st,\ 20\ °C}$	Steel thermal conductivity	15	W/m/K
$c_{p_{st},\ 20\ °C}$	Steel heat capacity	500	J/kg/K
e	Steel screen thickness	0.80	mm

TABLE 2.4: Physical properties of the screen

2.4.4 Screen heating up direct model

In order to accurately describe the screen temperature evolution, the direct model has to account for interception of the incident heat flux, conduction inside of the screen, convective and radiative heat loss on the two faces. In this case, the temperature of the screen is governed by a classic 3D transient conduction model:

$$\rho_{st} c_{p_{st}} \frac{\partial T}{\partial t} = \lambda_{st} \Delta T \tag{2.2}$$

The set of boundary conditions are based on the the heat flux continuity. On the upper surface of the screen, incident heat flux, convective and radiative heat loss contribute to the heat flux:

$$-\lambda_{st}\nabla T.\boldsymbol{n} = -\alpha_p\phi + h(T - T_{sur}) + \epsilon_p\sigma(T^4 - T_{sur}^4) \tag{2.3}$$

With a surrounding temperature T_{sur} of 20 °C.

On the lower surface of the screen, convective and radiative heat losses govern the heat flux:

$$-\lambda_{st}\nabla T.\boldsymbol{n} = h(T - T_{sur}) + \epsilon_{st}\sigma(T^4 - T_{sur}^4) \tag{2.4}$$

On the side of the screen, thermal insulation can be assumed:

$$-\lambda_{st}\nabla T.\boldsymbol{n} = 0 \tag{2.5}$$

This classical conduction model can be simplified. Indeed, temperature inside the screen might be uniform in its thickness because the screen is very thin and made out of conductive material. Radiative Biot number based on the screen thickness can be calculated (Eq. 2.6). Under the most severe circumstances using ϕ_{max}, the Biot number remains below 0.1. Therefore, the temperature of the screen can be assumed to be homogeneous in its thickness.

$$Bi_{rad,\ st} = \frac{\alpha_{st}\phi_{max}e}{\lambda_{st}\delta T} = 0.090 \tag{2.6}$$

The direct model can be simplified into a 2D transient model by inserting upper and lower surface boundary conditions (Ep. 2.3 and 2.4) as source terms in Eq. 2.2:

$$\rho_{st}c_{p_{st}}\frac{\partial T}{\partial t} = \lambda_{st}\Delta T + \frac{\alpha_p\phi}{e} - \frac{2h}{e}(T - T_{sur}) - \frac{(\epsilon_p + \epsilon_{st})\sigma}{e}(T^4 - T_{sur}^4) \tag{2.7}$$

With the boundary condition on the side of the screen:

$$-\lambda_{st}\nabla T.\boldsymbol{n} = 0 \tag{2.8}$$

2.4.5 Screen heating up inverse model

The inverse model (Eq. 2.9) was built based on the direct model. It enables the calculation of the incident heat flux ϕ and the convective heat transfer coefficient h for each pixel. Thus it yields a map of the incident heat flux. The idea behind the inverse model is to calculate the gap (called *observable* $y_{i,j}^k$) between the measured increase in temperature and the contribution of heat diffusion and radiation losses. This gap is directly associated to the contribution of the incident heat flux and the convective loss. Then using ordinary least square method [132], heat flux and convective heat transfer coefficient are computed to minimize this gap. Thus, the best fitting heat flux $\hat{\phi_{i,j}}$ and convective heat transfer coefficient $\hat{h_{i,j}}$ are determined for each pixel. In the present work, for the sake of simplicity, it is assumed that both

ϕ and h are constant in time for a given pixel.

The observable $y_{i,j}^k$ can be written for each pixel at each time step as follows:

$$y_{i,j}^k = T_{i,j}^{k+1} - T_{i,j}^k - dt\frac{\lambda_{st}}{\rho_{st}c_{p_{st}}}\Delta T_{i,j}^k - dt\frac{(\epsilon_p + \epsilon_{st})\sigma}{\rho_{st}c_{p_{st}}e}((T_{i,j}^k + 273)^4 - (T_{sur} + 273)^4) \quad (2.9)$$

Where, the Laplacian operator is computed using central finite differences scheme:

$$\Delta T_{i,j}^k = T_{i+1,j}^k + T_{i-1,j}^k - 4T_{i,j}^k + T_{i,j+1}^k + T_{i,j-1}^k \quad (2.10)$$

For a given pixel, the observable is written as follows:

$$\boldsymbol{y_{i,j}} = \begin{pmatrix} y_{i,j}^1 \\ \vdots \\ y_{i,j}^k \\ \vdots \\ y_{i,j}^{n-1} \end{pmatrix} \quad (2.11)$$

A sensitivity matrix $\boldsymbol{X_{i,j}}$ has to be built and inversed for each pixel. This matrix is the mathematical object which contains the contribution of the incident heat flux and the convective loss.

$$\boldsymbol{X_{i,j}} = \begin{pmatrix} \frac{dt\alpha}{\rho_{st}c_{p_{st}}e} & -\frac{2dt}{\rho_{st}c_{p_{st}}e}(T_{i,j}^1 - T_{sur}) \\ \vdots & \vdots \\ \frac{dt\alpha}{\rho_{st}c_{p_{st}}e} & -\frac{2dt}{\rho_{st}c_{p_{st}}e}(T_{i,j}^k - T_{sur}) \\ \vdots & \vdots \\ \frac{dt\alpha}{\rho_{st}c_{p_{st}}e} & -\frac{2dt}{\rho_{st}c_{p_{st}}e}(T_{i,j}^{n-1} - T_{sur}) \end{pmatrix} \quad (2.12)$$

Then, the system can be inverted using simple matrix operations yielding the incident heat flux and the convective coefficient maps:

$$\begin{pmatrix} \hat{\phi_{i,j}} \\ \hat{h_{i,j}} \end{pmatrix} = (X_{i,j}^T X_{i,j})^{-1} X_{i,j}^T y_{i,j} \quad (2.13)$$

The inverse method approach has two major advantages that are underlined here. First, on the contrary to CCD camera heat flux measurements, it does not require an external scaling factor. This factor being most of the time provided by a radiometer [87, 124]. Second, distance-temperature measurement encounters a reflexion problem. Indeed when the target is exposed to an incident heat flux, a fraction of this heat flux is reflected toward the captor. Thus the measured temperature is the sum of the actual temperature and the reflected heat flux contribution. Precaution

has to be taken in order to accurately monitor temperature [133, 134]. In the present work, by building the observable using temperature differences, the additive contribution of the reflected heat flux to the monitored temperature is nullified.

The thermal properties of the screen material were set as follows. As stated before, far from the focal spot, the screen temperature remains relatively low. It allows to reasonably assume that screen physical properties are constant. Values of the screen thermal conductivity and heat capacity can be found in Table 2.4. On the contrary, at the focal spot, screen temperature increases sharply up to 300 °C. Thus physical properties could not be assumed to be constant and the following correlations [135] were used to describe screen thermal conductivity and specific heat capacity evolution with temperature:

$$\lambda_{st}(T(K)) = 7.9318 + 0.023051\ T - 6.4166 \times 10^{-6} T^2\ \text{W/m/K} \tag{2.14}$$

$$c_{p_{st}}(T(K)) = 426.7 + 1.700 \times 10^{-1} T + 5.200 \times 10^{-5} T^2\ \text{J/kg/K} \tag{2.15}$$

2.4.6 Calibration method validation

It is common in the inverse method field to check the inverse algorithm capabilities with simulated values [136]. The direct model was computed with a prescribed heat flux. Then noise was added to the produced temperature data and finally the inverse algorithm was run. The agreement between actual values and estimated values of the incident heat flux was very good. From there, heat flux distribution were estimated from IR measurements for various distances ranging from $z = 0$ to $z = 150$ cm from the focal spot.

Figure 2.13 reports the determined heat flux contour map 100 cm away from the focal spot. One can see that the incident heat flux has a ring shape with a higher heat flux on the right hand side of the map. These discrepancies are attributed to error in the geometrical adjustment of the lamp and the mirror.

A Gardon radiometer was used to measure heat flux along the horizontal and vertical axes as a test to validate the inverse method estimation. Figure 2.14 compares the inverse method results with Gardon radiometer measurements. Both methods yield very close results. Moreover the inverse method provides at a time higher spatial resolution heat flux map than the Gardon radiometer measurements.

The beam total power is obtained by integrating the heat flux over the screen surface. Figure 2.15 reports the beam power variation as a function of the distance of the target to the focal spot. The incident power exhibits small variations of $\pm$ 5 % around an average value of 966 W. The accuracy of the presented measurements are

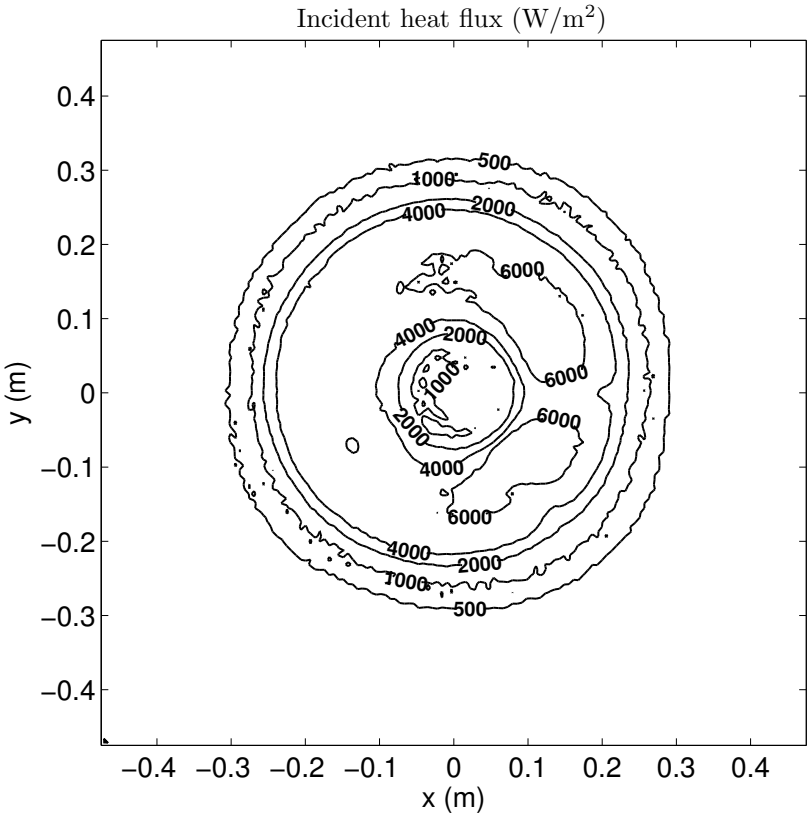

FIGURE 2.13: Heat flux mapping 1 m away from the focal spot

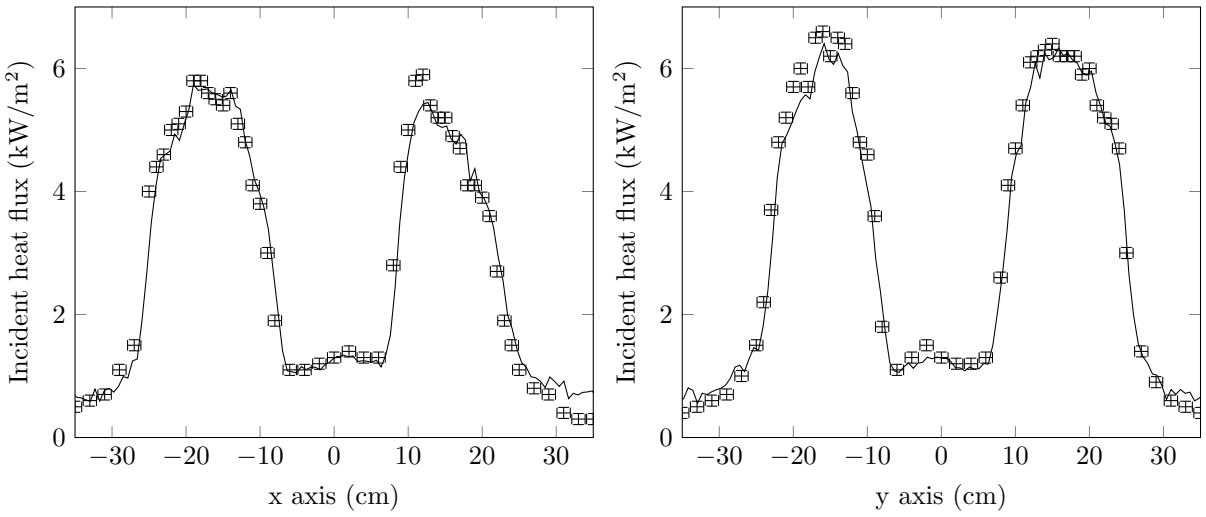

FIGURE 2.14: Heat flux 1 m away from the focal spot. Continuous line: from inverse method, crosses with error bars: from Gardon radiometer

thought to be very good.

Repeatability was assessed using the two measurements made for each distance. Figure 2.16 reports the deviation between two runs: it is lower than 5 % in

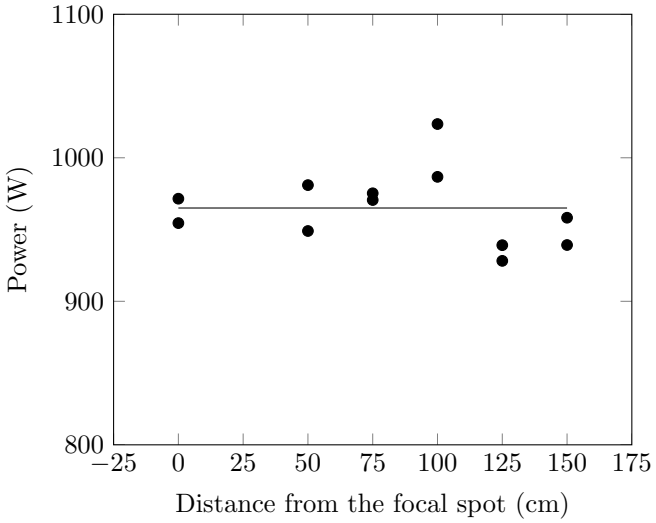

FIGURE 2.15: Incident power for all runs. Dot: individual value, continuous line: average value

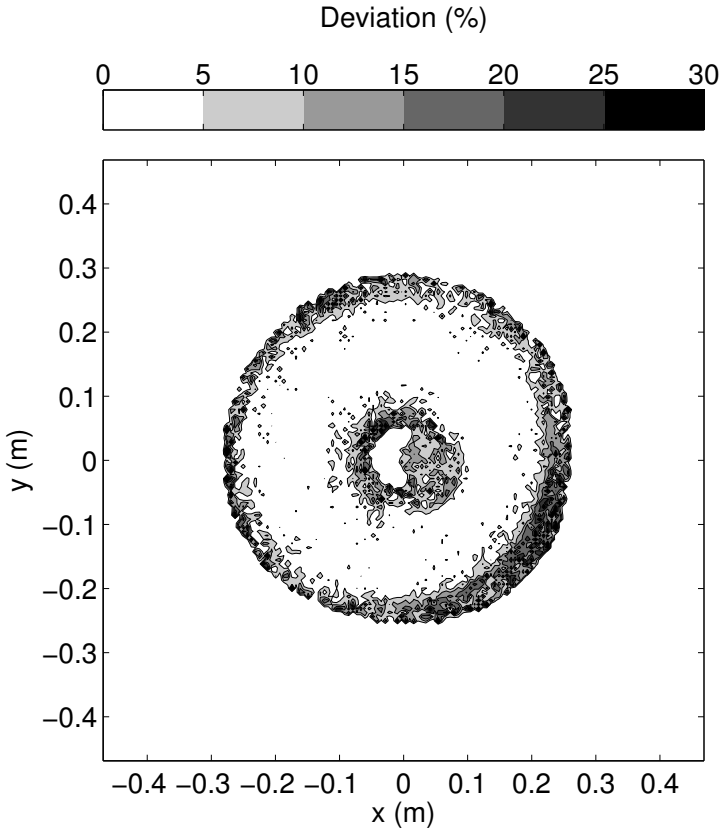

FIGURE 2.16: Typical deviation between two runs 1 m away from the focal spot

the regions where signal-to-noise ratio is good i.e. area with high incident heat flux. The discrepancy increases in low heat flux areas, which can be explained by the fact that the temperature rise is small in these regions: in this case, the sensibility coefficient associated to convective heat loss tends towards zero

(Eq. 2.16) which lowers inverse method predictions quality and therefore repeatability.

$$\lim_{T_{i,j}^k \to T_{sur}} -\frac{2dt}{\rho_{st} c_{p_{st}}(T_{i,j}^k) e}(T_{i,j}^k - T_{sur}) = 0 \tag{2.16}$$

2.4.7 Results

Figure 2.17 reports the determined heat flux distributions at the focal spot with and without the additional quartz window. The spatial distributions exhibit revolution symmetry. Figure 2.18 reports cut views of the heat flux distribution along x and y axes at the focal spot. In both configurations, the distributions along the two axes are very close. They exhibit a Gaussian shape, which is congruent with literature [123, 124, 127]. The discrepancies between the two configurations are around 11 % for the peak heat flux (1201 and 1072 kW/m^2, 11 % discrepancy) and the total incident power on the screen (936 and 820 W, 12 % discrepancy). Furthermore, with the additional window, the focal spot distribution is flatter than without it. Again, these trends are coherent with other authors' observations [87].

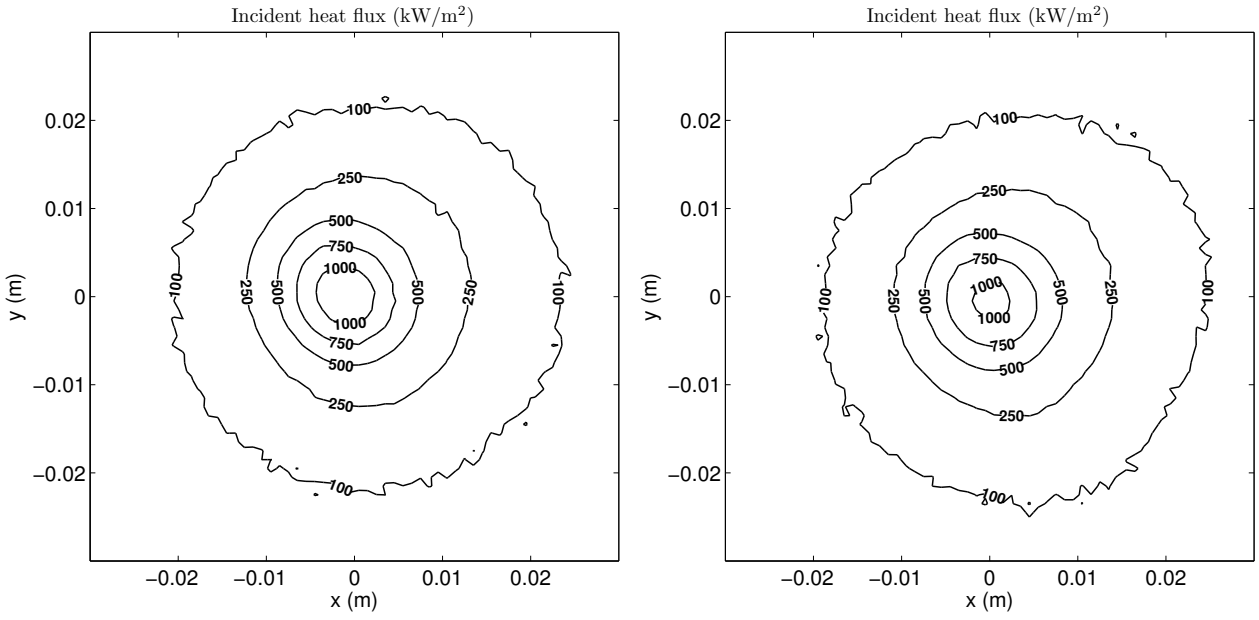

(A) Without additional window

(B) With additional window

FIGURE 2.17: Heat flux mapping at the focal spot

Integrating the heat flux distribution over the sample top surface yields the power delivered to the sample by the artificial sun. The sample is exposed to a Gaussian shaped heat flux with a maximum of 1072 kW/m^2 and a total power of 655 W.

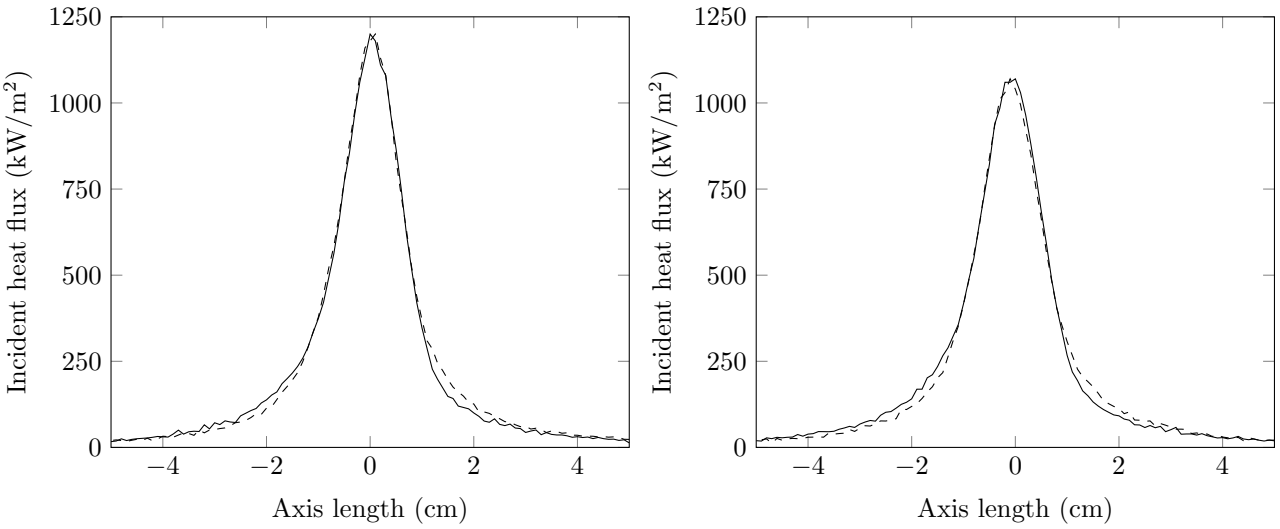

(A) Without additional window (B) With additional window

FIGURE 2.18: Heat flux distributions at the focal spot. Continuous line: along x axis, dashed line: along y axis

2.4.8 Comments on the calibration method

This calibration method uses inverse methods on a basic level. Using more advanced techniques, the incident heat flux can be further characterized. Among the critical possible improvements, time variability of the heat flux is of note. Indeed using more sophisticated approaches [130, 137, 138], it would be possible to compute a time dependent incident heat flux and convective heat transfer coefficient for each pixel.

Nevertheless, it is thought that the method used here can be trusted. Indeed, the set of results obtained far from the focal spot were validated by comparison with Gardon radiometer readings: the agreement between the two methods is very good. Furthermore, the computed beam total power has also been shown to be the same for several distances of the screen to the focal spot. Finding that total power is conservative is a token of the good quality of the proposed method.

2.5 Experimental procedures

Two different, yet similar, protocols were followed depending on whether or not the condenser was used.

Without condenser, the following steps were strictly followed for each run:

- drying the porous media upstream of the sample using a dry nitrogen flow until its mass stabilised (usually 2 hours)
- weighing of the sample and the reaction chamber

- fitting of the sample inside of the reaction chamber
- purging the system with nitrogen
- placing the cell at the focal spot
- starting mass and temperatures recordings
- opening of the shutter
- exposing the sample for 5 min
- closing of the shutter
- cooling the sample under nitrogen sweep for 5 min
- extracting the sample
- weighing the sample and the reaction chamber
- cleaning every part using isopropanol

With the condenser, some specific steps were added:

- drying the porous media upstream of the sample using a dry nitrogen flow until its mass stabilised (usually 2 hours)
- weighing the sample, the reaction chamber, the condenser and the cotton trap
- immersing condenser into liquid nitrogen
- fitting of the sample inside of the reaction chamber
- fitting the liquid nitrogen cooled condenser and the cotton trap into the reaction chamber
- purging the system with nitrogen
- placing the cell at the focal spot
- starting mass and temperatures recordings
- opening of the shutter
- exposing the sample for 5 minutes while collecting gas sample
- closing of the shutter
- cooling the sample under nitrogen sweep for 5 min
- extracting the sample and the condenser
- weighing the sample, the reaction chamber, the condenser and the cotton
- placing tar soiled cotton in air tight recipient

- cleaning every part using isopropanol

In order to assess the run to run repeatability, each run was repeated at least three times.

2.6 Data processing

To go from raw data to information, mass and temperature measurements need refinement. The mass signal processing into wood consumption and also drying water release, char gas and tar average production rates is described below. Then, the next step is taken by calculating mass and energy balances.

2.6.1 Gas, tar, water and char final yields

To derive gas, tar, water and char final yields, different parts of the experimental device were weighed before and after a run (Section 2.3.1.4). These measurements are used to calculate mass variations over a run. Then, these mass variations are divided by the run time in order to obtain consumption and production rates.

Samples were exposed to radiative power in two configurations: with and without condenser. During a run without the condenser, gas, tar and water freely escaped from the reaction chamber. Thus, the reaction chamber mass variation $\delta m_{chamber,\ no\ cond}$ accounts for the mass of gas produced by the sample m_{gas}, the mass of evaporated water from the sample m_{water} and the mass of tar produced by the sample m_{tar} (Eq. 2.17).

$$\delta m_{chamber,\ no\ cond} = m_{chamber,\ fin\ no\ cond} - m_{chamber,\ ini\ no\ cond} = m_{gas} + m_{water} + m_{tar} \tag{2.17}$$

During a run with the condenser, gas alone escapes from the reaction chamber. Thus, the reaction chamber mass variation $\delta m_{chamber,\ cond}$ only accounts for the mass of gas produced by the sample m_{gas} (Eq. 2.18).

$$\delta m_{chamber,\ cond} = m_{chamber,\ fin\ cond} - m_{chamber,\ ini\ cond} = m_{gas} \tag{2.18}$$

The question of the validity of the comparison between $\delta m_{chamber,\ no\ cond}$ and $\delta m_{chamber,\ cond}$ may arise. Indeed, these two values are not determined using the same sample. Comparing the reaction chamber mass variation in the two configurations (i.e. $\delta m_{chamber,\ no\ cond}$ and $\delta m_{chamber,\ cond}$) is possible thanks to the good run to run repeatability of the mass signal (Fig. 2.19).

From these various measurements, it is possible now to determine the mass of evaporated water released by the sample m_{water}. First of all, m_{wood}, m_{char}, $m_{sample,\ ini}$, $m_{sample,\ fin}$, m_{gas} and $\delta m_{chamber,\ no\ cond}$ are known. We now consider the sample mass variation δm_{sample}. It accounts for the mass loss of wood m_{wood}, mass loss by

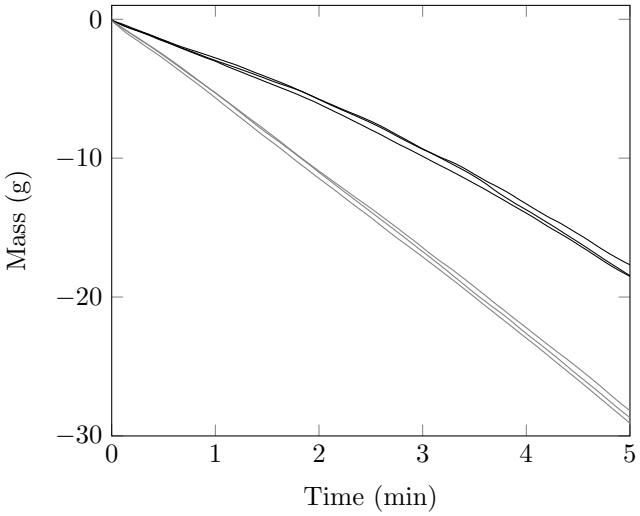

FIGURE 2.19: Six mass signals of reference case samples (9 %wb, bois de bout). Black: with condenser (stopping tar and water), gray: without condenser

drying m_{water} and mass gain by char formation m_{char} (Eq. 2.19). It possible to access m_{water} using Eq. 2.19. By knowing m_{water}, it is now possible to access m_{tar} using Eq. 2.20.

$$\delta m_{sample} = m_{sample,\ fin} - m_{sample,\ ini} = m_{char} - m_{wood} - m_{water} \tag{2.19}$$

$$m_{tar} = m_{chamber,\ fin\ no\ cond} - m_{chamber,\ ini\ no\ cond} - m_{gas} - m_{water} \tag{2.20}$$

It is therefore possible to calculate the average wood consumption and also drying water release, char, gas and tar average production rates by dividing the masses by the total run time of 5 minutes. These time averaged production rates are to be considered with caution. Indeed, one should bear in mind that actual, time dependent, production rates may not be constant over time.

Furthermore, by continuously weighing the reaction chamber during a run with the condenser, it is possible to monitor the evolution of gas production rate over time.

2.6.2 Mass and energy balances

Knowing the different species production rates, it is easy to derive the mass balance by comparing gas, tar and char production rates to wood consumption rate. In order to go further, energy balance is computed.

The considered system is the reaction chamber enclosing the sample. In order to compute energy balance, it is mandatory to identify energy inlets, outlets, sources, sinks and storages. There are two energy inflows and sources:

- the incident radiative power
- the chemical power of the pyrolysed wood

Four energy outflows and sinks can be counted:

- the chemical energy stored in gas and tar
- the sensible heat contained in the flue gas
- the water vaporisation heat
- the power emitted by the exposed surface of the sample

The system can store energy in two ways:

- the chemical energy stored in the produced char
- the sensible heat contained in the remains of the sample

Knowing the production rates of the different species, it is possible to calculate the chemical power contained in their flows using their Higher Heating Value (HHV). Wood, tar and char HHVs were taken from literature with values of 19.0, 19.0 and 32.1 MJ/kg respectively [139–141]. Gas HHV was calculated based on its composition using individual species HHV (Table 2.5). Using temperature measurements, the sensible heat contained in the flue gas and the remains of the sample can be evaluated. Sensible heat evaluation requires to know the specific heat capacity of the flue gas and the remains of the sample. Those were estimated, as the nitrogen specific heat capacity at the flue gas temperature for the flue gas, and as the wood specific heat capacity at 50 °C for the remains of the sample.

Species	HHV (MJ/kg)
Beech wood	19.0
Tar	19.0
Char	32.1
H_2	142
CO	10.1
CO_2	0
CH_4	55.5
C_2H_2	49.9
C_2H_4	50.3
C_2H_6	51.9
C_3H_8	50.4

TABLE 2.5: Species Higher Heating Value (HHV) [139–142]

Evaluating the radiative heat loss is more challenging. The power emitted by the sample ($P_{rad,loss}$) can be estimated using Eq. 2.21. Yet, one needs to determine the surface and the temperature of the power emitting area. The temperature is taken as

the one reported by the radiometer. The radius of the area is taken as the radius of the focal spot (r_{fs}). It is commonly determined using the width of the incident heat flux profile taken at the half of its maximum (Fig. 2.20). In our case, $r_{fs} = 7.3$ mm.

$$P_{rad,\ loss} = \pi r_{fs}^2 \sigma (T^4 - T_{sur}^4) \tag{2.21}$$

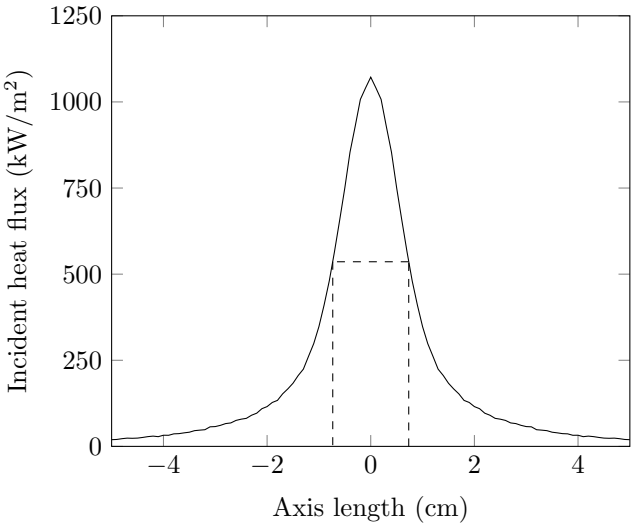

FIGURE 2.20: Incident heat flux distribution on the sample. Dashed lines: width of the profile at the half of its maximum

Conclusion

This chapter presented the materials and methods used in the experimental part of this work. The samples are thermally thick beech wood cylinder whose fiber orientation and initial moisture content is controlled. They are set in an enclosure referred to as the reaction chamber. This reaction chamber allows to expose the sample to high solar heat flux, to control the sample atmosphere, to monitor key parameters and to analyse the produced gas. For convenience sake, an artificial sun is used as radiation source. Special care was taken in calibrating this device, leading to the development of a new method of calibration for solar concentrating systems. Finally, experimental protocols and data processing methods were presented. They should allow to determine wood consumption, water, gas tar and char production rates as well as mass and energy balances.

CHAPTER 3

Experimental results

Introduction

The following chapter presents the results obtained thanks to the experimental device. It is divided into five parts, each one dealing with a specific aspect of the results.

The first part analyses the results associated with the reference case (9 %wb, bois de bout). The results can be broken into different categories: sample geometry, reported temperatures, consumption and production rates, gas, tar and char compositions.

The second part compares the sample geometry evolution for the six configurations. Two different patterns emerge from this comparison. None of them have been reported in literature before. They are thought to be specific to biomass solar gasification.

The third part deals with the impact of the sample fiber orientation relative to the incident heat flux. The two configurations will be compared in the light of consumption and production rates, reported temperatures and gas composition.

The fourth part focuses on the effects of the sample initial moisture content.

The last part details the establishment of an energy balance. Mass and energy balance closures being quite good, they allowed to go one step further and to deduce system energy conversion efficiency.

3.1 Reference case processing

The case processing is extensively described here for the reference case: 9 %wb, bois de bout. The data reported by the experimental device are analysed first, then gas, tar and char compositions are discussed.

3.1.1 Experimental observations

Figure 3.1 shows the samples after a 5 minutes exposure to radiation. A complex geometry has developed. On the top view, one can see a fractured design showing alternatively empty canyons and char rods. The cut view highlights the presence of a charred area with a crater shape. This shape corresponds roughly to the incident heat flux distribution. This crater is filled with standing char rods as illustrated in Figure 2.8.

Sample mass evolution with time have already been reported in Figure 2.19. The mass curves exhibit linear trends, with almost no inflexion. It is therefore not

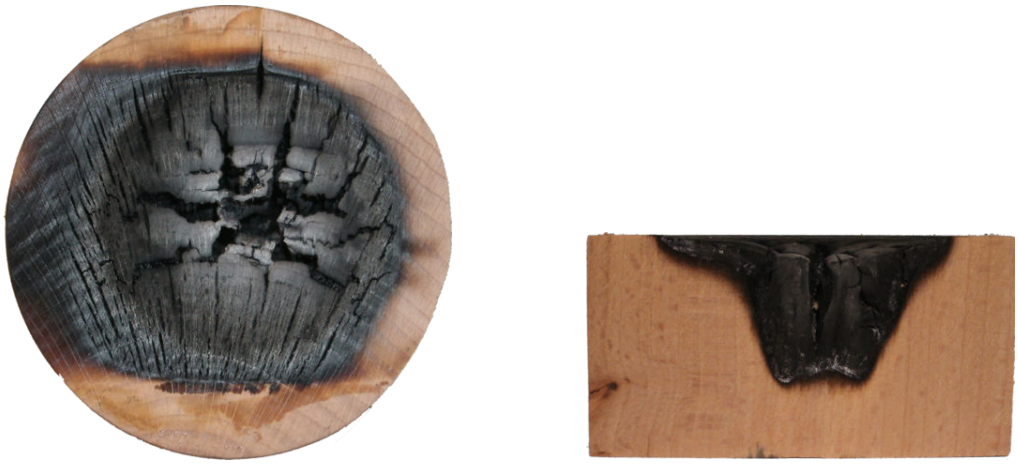

(A) Top view (B) Cut view

FIGURE 3.1: Sample views after a 5 minutes exposure for the reference case (9 %wb, bois de bout)

possible to identify phenomena at stake from mass readings. Yet, these curves can be processed to yield averaged production/consumption rates.

On average, wood consumption rate is 5.76 g/min (Table 3.1). It is mainly transformed into gas (3.65 g/min) and char (1.37 g/min). The production of tar is quite low with only 9 % (0.50 g/min) of the dry wood being turned into tar. This low tar yield is later explained by tar thermal cracking and steam reforming.

Radiometer surface temperature measurements are reported in Figure 3.2. During the first few seconds of the run, the reading exhibits an overshoot. This overshoot is explained by the high reflectivity of virgin wood around 63 % [109] that blinds the radiometer with reflected light from the xenon arc lamp. Once the surface is charred, the reflectivity drops to near zero and allows for a proper measurement of the surface temperature. During a run, surface temperature is around 1530 °C, with a slightly downward trend. Between runs, measurements exhibit the same trend, yet ± 120 °C variations are observed. It is known from literature that temperatures higher than 800 °C are required to achieve tar thermal cracking [75] and tar steam reforming [76]. Here, the reported temperature is much higher than 800 °C, making tar thermal cracking and tar steam reforming kinetically favoured.

Figure 3.3 presents in depth thermocouple temperature measurements. These measurements show a wide run to run variation. Indeed, thermocouples are located in a fractured medium. Depending on the thermocouple location, i.e. inside a char rod or in between two rods, the reported temperatures differ. When located in between two rods, the thermocouple is directly exposed to the incident heat, therefore its temperature increases sharply. When concealed inside of a char rod, the temperature history shows a plateau around 100 °C, associated to drying, and then steadily increases. Nevertheless, it yields some information on the sample heating rate. From thermocouple inside a rod readings, heating rate inside of the sample is

		Time averaged rate (g/min)					Temperature
		Wood	Water	Char	Gas	Tar	(°C)
Bois de bout	0 %wb	7.05 ± 0.48	0.49 ± 0.49	1.74 ± 0.002	4.12 ± 0.07	1.63 ± 0.88	1594 ± 123
	9 %wb	5.76 ± 0.42	1.57 ± 0.43	1.37 ± 0.002	3.65 ± 0.07	0.50 ± 0.82	1530 ± 120
	55 %wb	0.99 ± 0.02	5.89 ± 0.06	0.09 ± 0.002	1.70 ± 0.55	-0.87 ± 0.93	1317 ± 98
Bois de fil	0 %wb	7.09 ± 0.48	0.06 ± 0.49	1.48 ± 0.002	3.64 ± 0.19	1.84 ± 0.98	1616 ± 46
	9 %wb	5.68 ± 0.42	1.09 ± 0.42	1.38 ± 0.002	3.58 ± 0.23	0.49 ± 0.83	1605 ± 90
	55 %wb	1.49 ± 0.03	2.57 ± 0.04	0.17 ± 0.002	1.94 ± 0.20	-0.80 ± 0.98	1426 ± 20

TABLE 3.1: Time averaged wood consumption, water, char, gas and tar production rates and average surface temperature for the six configurations

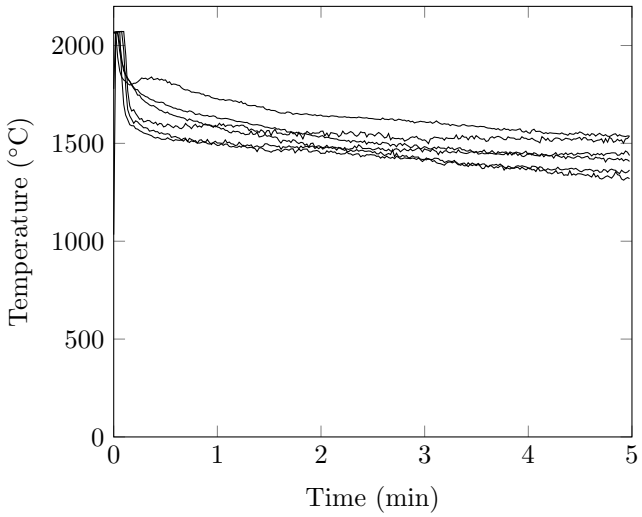

FIGURE 3.2: Six different runs surface temperature for the reference case (9 %wb, bois de bout)

around 250 K/min in the 100 to 600 °C zone.

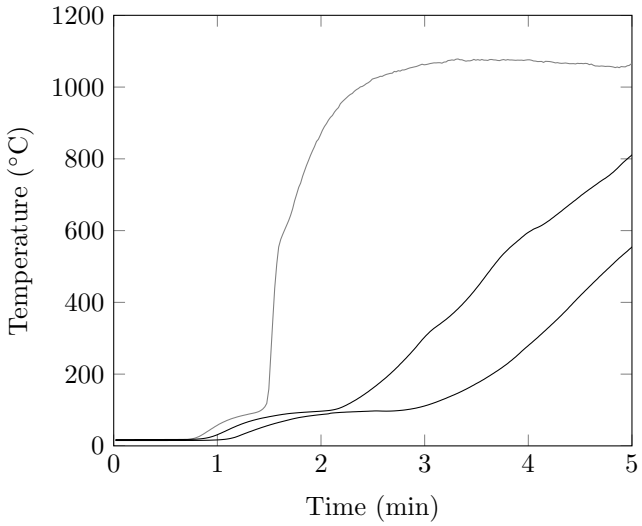

FIGURE 3.3: Temperature histories reported by thermocouple on the sample axis for the reference case (9 %wb, bois de bout). Gray: thermocouple positioned in between two rods, black: thermocouples positioned inside of a rod

Figure 3.4 reports the N_2 free gas composition along a run. One can see that H_2 and CH_4 fractions remain constant throughout a run, while CO fraction decreases from 44 % to 36 % and CO_2 fraction increases from 5 % to 17 %. The explanation for the observed trends in terms of gas composition is not straightforward because both tar cracking and tar steam reforming reactions may participate in the process. Furthermore, it cannot be asserted that thermochemical equilibrium is reached in the gas phase; the process is potentially kinetically limited. Finally, an in depth explanation lies beyond the scope of this work. Other species - C_2H_2, C_3H_8, C_2H_6 and C_2H_4 - present in the gas were quantified (Fig. 3.5). Given the measurement

uncertainty, their fractions can be considered stable during a run. Gas readings show a good repeatability from run to run. Therefore, the averaged total gas production rate was computed from the average gas composition. The obtained values are 10 % close to the one obtained using mass measurements. It is thought to be a very satisfactory agreement.

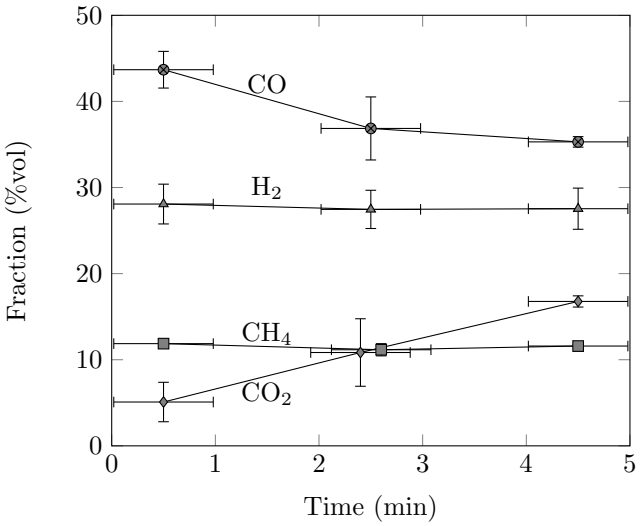

FIGURE 3.4: Gas composition downstream the condenser for the reference case (9 %wb, bois de bout), major species. Triangle: H_2, circle: CO, diamond: CO_2, square: CH_4

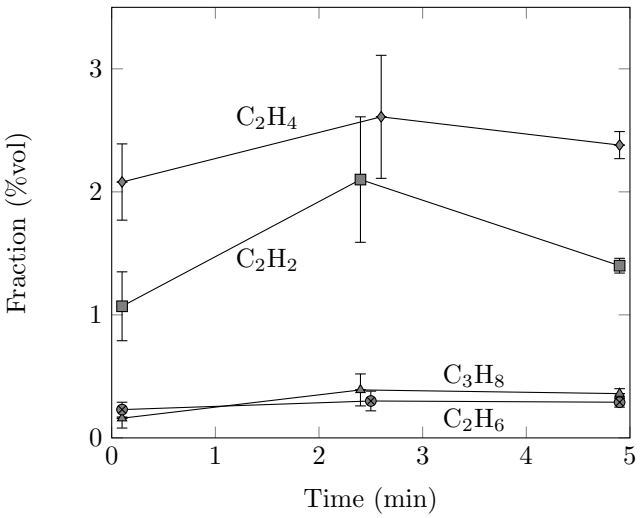

FIGURE 3.5: Gas composition downstream the condenser for the reference case (9 %wb, bois de bout), minor species. Triangle: C_3H_8, circle: C_2H_6, diamond: C_2H_4, square: C_2H_4

Tar analyses show that they are mainly composed of primary (acetic acid, phenol, hydroxyethanal, 1-hydroxy-2-propanone) and tertiary (naphthalene, acenaphthalene, phenanthrene) organic tar [74] (Appendix A). This configuration, where primary and tertiary tar are found together with no significant amount of secondary tar, is known to be a sign of intense thermal cracking [75]. Furthermore, the analyses show

a good run to run repeatability even though tar were stored for a long time before being analysed.

Until now, we only considered time averaged value of production rates. The experimental device allows to go one step further and study the gas production rate evolution with time. Gas production rates for the reference case is available in Figure 3.6. Gas production clearly increases with time. It is thought that as the char crater grows the residence time of tars inside of it increases. Therefore, the contact time between steam and tar before quenching by nitrogen sweep increases, favouring tar thermal cracking and tar steam reforming leading to gas formation.

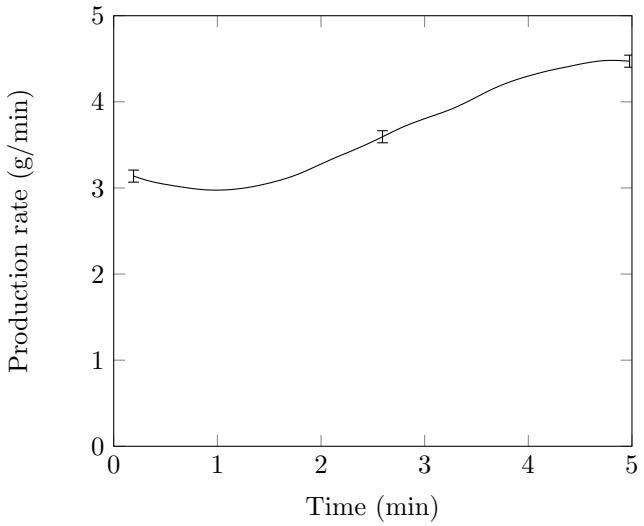

FIGURE 3.6: Gas production rate for the reference case (9 %wb, bois de bout) with estimated error bars

3.1.2 Char properties

In order to get more insight on char composition and structure, char rods were taken from the sample and ground. Nevertheless, one should keep in mind that the char may not be homogeneous throughout the sample. Therefore, obtained results reflect average char properties.

Table 3.2 reports the ultimate analysis for char obtained from bois de bout with different initial moisture content. These char compositions are similar. They all exhibit high oxygen and hydrogen contents. Oxygen fractions can be as high as 18.11 % for 55 %wb initial moisture content sample. Yet, these results are in good agreement with the existing study on solar pyrolysis [25]. High oxygen and hydrogen fractions of are signs that these chars have not undergone thermal annealing [46] even though they were produced at high temperature. It might be explained by the fact that the char does not spend enough time at high temperature to undergo a significant amount of annealing.

Wood initial moisture content	0 %wb	9 %wb	55 %wb
Carbon	85.06	87.82	78.5
Hydrogen	2.94	2.75	3.05
Oxygen	11.99	9.43	18.11
Nitrogen	-	-	0.34
Sulphur	-	-	-

TABLE 3.2: Char ultimate analysis (%wt)

A TriStar II 3020 BET was used to determine the chars specific surface area and pore volume (Table 3.3). These values are in good agreement with literature [25]. Furthermore, two trends emerge from these measurements: a higher initial moisture content leads to higher specific surface area and pore volume and bout de fil configurations exhibit higher specific surface area and pore volume than bois de bout configurations. The first trend can be explained by the fact that high initial moisture content enables char steam gasification to a higher extent than low initial moisture content cases. Gasification turns char into gas, and hence increases the specific surface area and pore volume. Thus a higher amount of char steam gasification induces a higher specific surface area and pore volume. Regarding the impact of fiber orientation, it can be noted that in bois de fil configurations, gases escape by the rear of the char rods while they escape by the top of the rods in bois de bout configurations. Hence, the residence time of tar inside of the rods is shorter in bout de fil configurations than in bois de bout configurations. Thus, less time is offered to tar repolymerisation reactions, carbon deposit is therefore less important which leads to higher surface area and pore volume.

		Specific surface area (m^2/g)	Pore volume (cm^3/g)
Bois de bout	0 %wb	44.13	0.01150
	9 %wb	76.56	0.02415
	55 %wb	86.61	0.04905
Bois de fil	0 %wb	93.16	0.04087
	9 %wb	69.86	0.03053
	55 %wb	122.38	0.08774

TABLE 3.3: Chars BET specific surface area and BJH adsorption pore volume

The structure of a char rod was also analysed using scanning electron microscope (SEM) (Fig. 3.7). From the top view, one can see that the char has kept the wood channel structure. Special structures can be found at the end of these channels. They look like solidified liquid. They are thought to be *intermediate liquid compound* [22, 56], that was molten during the run and that solidified during the sample cooling. On the side view, it is possible to see minerals (white dots) uniformly spread throughout the surface.

Finally, char spectral properties have already been reported in Section 2.2.2.

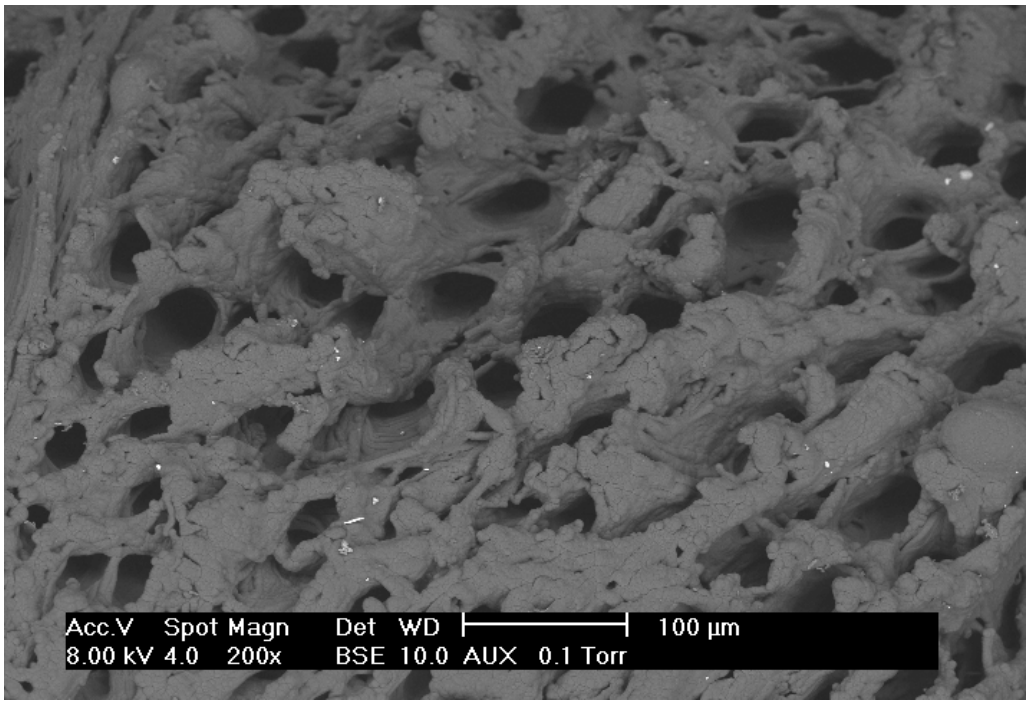

(A) Top view

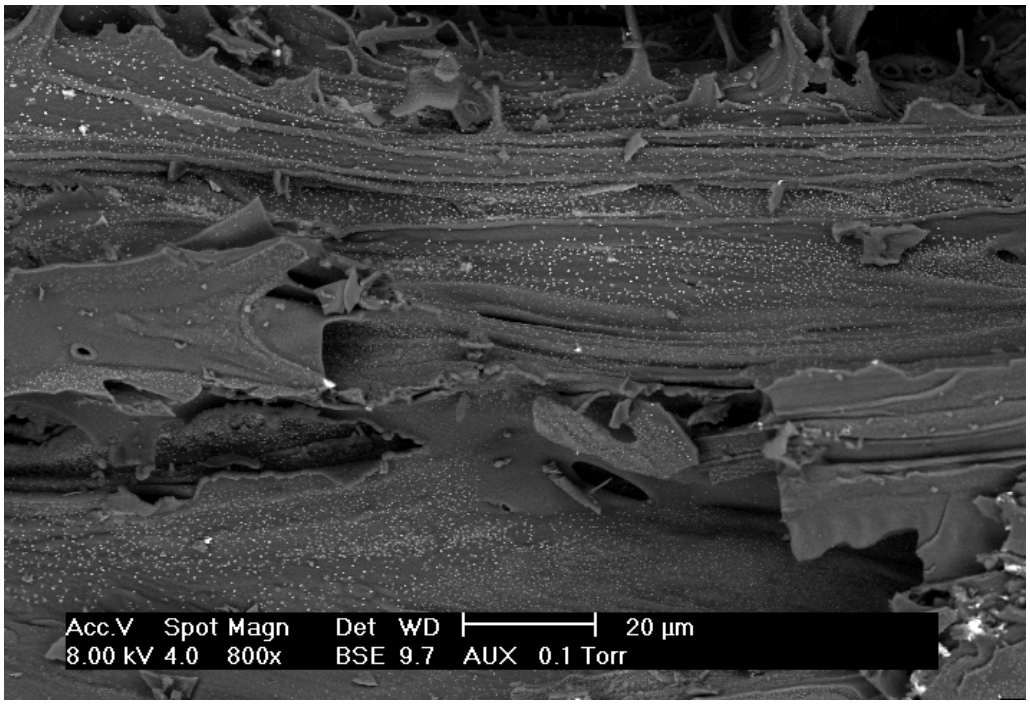

(B) Side view

FIGURE 3.7: Char rod SEM pictures for the reference case (9 %wb, bois de bout)

They are in good agreement with values found in literature.

3.2 Crater formation

Top and cut views of 0, 9 and 55 %wb initial moisture content samples in both fiber directions are reported in Figures 3.8 and 3.9. The 0 %wb initial moisture content samples cut views are close to those of 9 %wb initial moisture content samples. During a run, sample geometry is significantly modified. Two main behaviours emerge from these observations. For low initial moisture content samples, char rods stand inside the crater. For high initial moisture content samples, a smaller crater is formed, yet no rods stand inside of it. Moreover, cut views show that the transition between wood and char is very sharp. It is therefore possible to consider that the sides of the crater are in fact the location of a pyrolysis front. Sadly, no transition between wet and dry wood can be observed. Thus, it is not possible to locate a potential drying front.

In the case of low initial moisture content samples, wood shrinkage and mechanical failure are thought be at the origin of the char rods formation. Indeed, it is known that during pyrolysis wood shrinks as it turns into char loosing about 65 % of its initial volume [108, 109]. In this case, under radiative heat flux, the medium undergoes pyrolysis and starts shrinking. As the mechanical constraint grows, some weak spots in the wood structure break. These breaks yield char rods on one hand and canyons on the other. Then the canyons allow the radiation to penetrate even further inside of the sample, providing energy for in depth pyrolysis. In the end, this mechanism yields a crater zone which has a shape close to incident heat flux distribution. Moreover, it is possible using the cut view pictures to determine the pyrolysis front thickness. The front thickness is about 4 mm for 0 %wb samples and 3 mm for 9 %wb samples

In the case of high initial moisture content samples, steam coming from drying is thought to play a major role in the geometrical evolution of the sample. In the case of low initial moisture content samples, the amount of water released by drying is not high enough to allow for complete char gasification. For high initial moisture content samples, the drying provides enough steam to gasify the char produced by the pyrolysis. Indeed, in order to escape from the sample, the steam has to go through the char which is at a temperature far higher than 800 °C. Therefore, char undergoes steam gasification which explains why no char rods are found inside of the crater. Furthermore, the pyrolysis front thickness is small, about 0.5 mm. Indeed, pyrolysis is thought to be shortly preceded by a drying front and is closely followed by a gasification front which immediately consumes the char produced by the pyrolysis front

There are also similarities in the crater shapes between bois de bout and bois de fil sample (Fig. 3.9). In the case of 0 and 9 %wb initial moisture samples, the char rods inside of the crater are standing upward in both cases. This is surprising given the fact that in the bois de fil cases, the wood fibers are orthogonal to the incident heat flux. Nevertheless, some minor discrepancies remain. One can also note that the average diameter of the char rods is more important for bois de fil samples. Bois de bout samples exhibit a deeper and narrower crater than bois de fil samples. This is due to the fact that wood is an anisotropic material. In the bois de bout cases, the fiber orientation favours heat conduction towards the bottom of

(A) 0 %wb bois de bout

(B) 0 %wb bois de fil

(C) 9 %wb bois de bout

(D) 9 %wb bois de fil

(E) 55 %wb bois de bout

(F) 55 %wb bois de fil

FIGURE 3.8: Sample top views after 5 minutes exposure

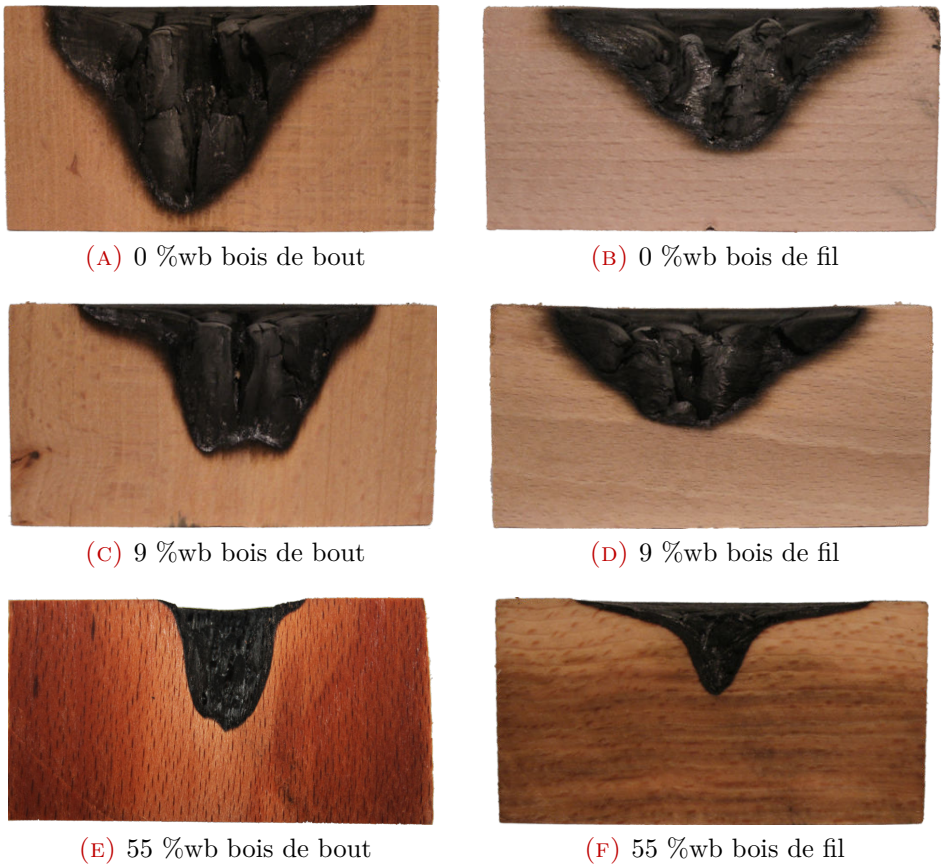

(A) 0 %wb bois de bout (B) 0 %wb bois de fil

(C) 9 %wb bois de bout (D) 9 %wb bois de fil

(E) 55 %wb bois de bout (F) 55 %wb bois de fil

FIGURE 3.9: Sample cut views after 5 minutes exposure

the crater inducing sharper shapes. In the bois de fil cases, the fiber orientation favours heat conduction towards the sides of the crater inducing flatter shapes. Char internal geometry also differs between the two configurations. As aforementioned, bois de fil samples exhibits higher specific surface area and pore volume than bois de bout samples (Table 3.3).

3.3 Impact of fiber orientation

Sample fiber orientation varies between two extreme configurations: bois de bout (vertical fibers) and bois de fil (horizontal fibers). This difference was expected to have an impact on the behaviour of the samples because wood is an anisotropic material. Indeed, the ratio of longitudinal to radial thermal conductivity is about 2 [143] and the ratio of the permeability for the same directions is about five thousand [34].

Figure 3.10 allows for a direct confrontation of the production/consumption rates between the two fiber orientations (data can be found in Table 3.1). The wood consumption, drying water release, gas, tar and char production rates exhibit close values with only one exception for the 55 %wb cases. In these particular cases, water released is much higher for vertical fiber samples than for horizontal ones. It can be

explained by the fact that these saturated samples dry in pure nitrogen. Indeed, the channels of the wood come out directly on a dry nitrogen sweeping flow. This setup dramatically promotes drying. In the case of bois de fil samples, the channels of the wood come out on the side of the sample, where there is no sweep. The discrepancy between bois de bout and bois de fil water release rate for 55 %wb samples is explained by a more efficient drying in the first case. This was checked in special experiments where samples were expose to the nitrogen sweep without radiative heating.

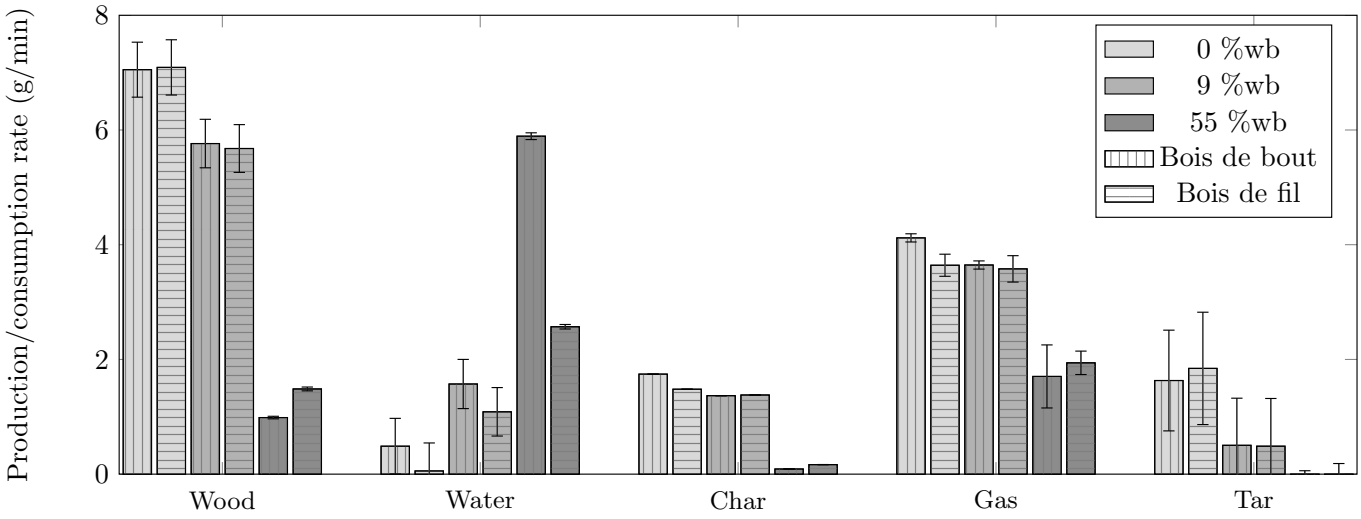

FIGURE 3.10: Production/consumption rates for the six configurations

Figure 3.11 reports the fractions of the major components of the gas at the outlet of the condenser (data can be found in Table 3.4). The gas composition for the two fiber orientations are very close for CO, CO_2 and CH_4. The fraction of H_2 may seem to be slightly more important for bois de fil, yet, given the uncertainty, no solid conclusion can be drawn. The same can be stated for minor gas components as reported in Table 3.5.

Finally, average surface temperatures are very close for bois de bout and bois de fil configurations (Table 3.1).

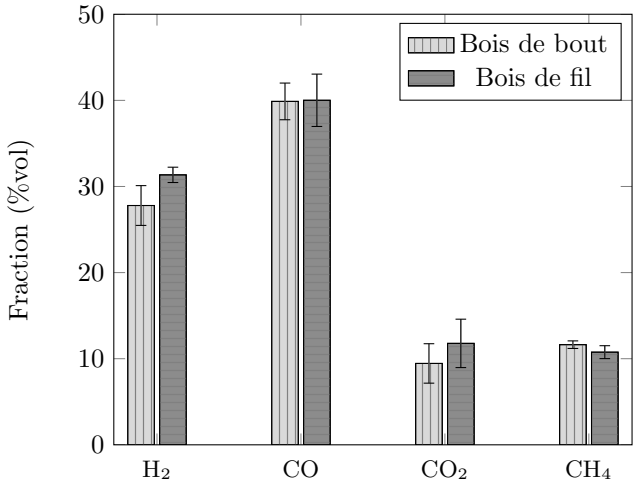

FIGURE 3.11: Fractions of major components in the gas for 9 %wb moisture content samples. Dark gray: bois de bout, light gray: bois de fil

		Fraction (%vol)			
		H_2	CO	CO_2	CH_4
Bois de bout	0 %wb	25.85 ± 2.06	43.16 ± 2.37	11.09 ± 2.59	13.22 ± 0.53
	9 %wb	27.79 ± 2.31	39.88 ± 2.13	9.45 ± 2.29	11.63 ± 0.44
	55 %wb	37.81 ± 3.42	30.95 ± 3.12	12.15 ± 2.41	8.47 ± 0.95
Bois de fil	0 %wb	30.52 ± 3.32	40.53 ± 1.17	11.23 ± 2.01	11.23 ± 0.49
	9 %wb	31.35 ± 0.89	40.01 ± 3.04	11.78 ± 2.81	10.76 ± 0.75
	55 %wb	36.83 ± 1.69	33.42 ± 2.36	13.51 ± 2.13	8.71 ± 0.53

TABLE 3.4: Fractions of major components in the N_2 free gas at the outlet of the condenser averaged throughout a run

		Fraction (%vol)			
		C_2H_2	C_3H_8	C_2H_6	C_2H_4
Bois de bout	0 %wb	1.69 ± 0.48	0.31 ± 0.13	0.34 ± 0.05	2.73 ± 0.29
	9 %wb	1.41 ± 0.28	0.27 ± 0.08	0.26 ± 0.06	2.29 ± 0.31
	55 %wb	1.70 ± 0.38	0.03 ± 0.02	0.11 ± 0.02	1.80 ± 0.32
Bois de fil	0 %wb	1.33 ± 0.19	0.20 ± 0.08	0.32 ± 0.05	2.26 ± 0.39
	9 %wb	1.58 ± 0.51	0.22 ± 0.11	0.29 ± 0.04	2.08 ± 0.20
	55 %wb	1.65 ± 0.26	0.10 ± 0.05	0.20 ± 0.03	1.97 ± 0.12

TABLE 3.5: Fractions of minor components in the N_2 free gas at the outlet of the condenser averaged throughout a run

3.4 Impact of initial moisture content

The comparison of production/consumption rates between different initial moisture contents cases is not direct. For instance, the amount of gas produced by a high initial moisture sample is lower than for an initially dry sample. Yet, the amount of converted wood is not the same between these two. In order to solve this problem,

the water, char, gas and tar production rates were divided by the wood consumption rate, giving yields on dry wood basis (Table 3.6).

		Water	Char	Gas	Tar	Closure (%)
Bois de bout	0 %wb	0.07 ± 0.07	0.25 ± 0.02	0.58 ± 0.05	0.23 ± 0.14	106
	9 %wb	0.27 ± 0.09	0.24 ± 0.02	0.63 ± 0.06	0.09 ± 0.15	96
	55 %wb	5.97 ± 0.20	0.09 ± 0.01	1.73 ± 0.60	-0.89 ± 0.93	105
Bois de fil	0 %wb	0.01 ± 0.07	0.21 ± 0.01	0.51 ± 0.06	0.26 ± 0.16	98
	9 %wb	0.19 ± 0.09	0.24 ± 0.02	0.63 ± 0.09	0.09 ± 0.15	96
	55 %wb	1.73 ± 0.07	0.11 ± 0.01	1.31 ± 0.17	-0.54 ± 0.65	88

TABLE 3.6: Time averaged yields on dry wood basis and mass closure

Firstly, as one can see from Table 3.6, the closure of the mass balance is between 88 and 106 % which is quite good. Then, as stated before, fiber orientation induces only minor variations in terms of yields. Figure 3.12 reports the relative production yields for bout de fil samples; two main trends emerge from these results:

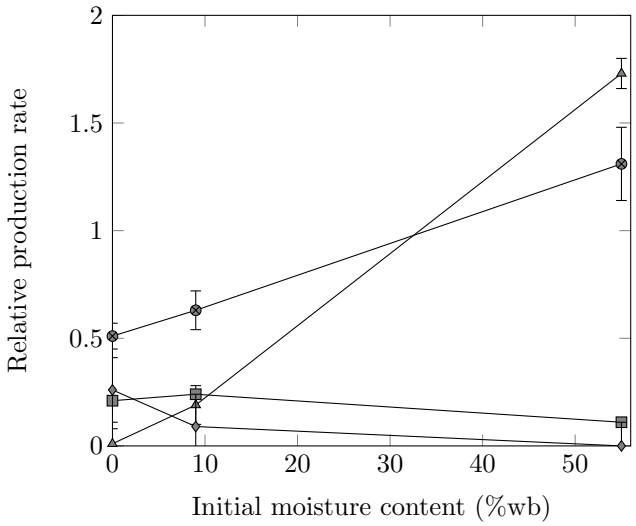

FIGURE 3.12: Relative production rate for bout de fil samples over the range of initial moisture content. Triangle: drying water, square: char, circle: gas, diamond: tar

- an increase in sample initial moisture content leads to a significant reduction of tar production. For 0 %wb initial moisture content samples, about 25 % of the wood is transformed into tar. Whereas the tar yield is only 9 % for 9 %wb initial moisture content samples. Tar steam reforming is thought to play a role in this reduction. Indeed, both tar and steam have to escape the medium passing through the crater where temperature is high enough to promote tar steam reforming

- an increase in sample initial moisture content leads to a major increase in gas production, relative to the wood consumption. The gas yield even exceeds 1 for

55 %wb initial moisture content samples. This means that the produced gas mass exceeds the consumed dry wood mass. It is possible if steam contributes to gas mass through char steam gasification, tars or methane steam reforming

The reported tar production rates are negative for 55 %wb initial moisture content samples (Table 3.1). The error associated with these measurements is quite high. Two observations are to be added. It has been qualitatively observed that tar production during these runs is actually very low. Indeed, at the end of these runs the condenser contains only water; no sign of tar (in terms of deposit, color nor smell) can be found in it. Furthermore, the tar cotton trap is superficially coloured in light brown, suggesting that only few tars were produced and trapped.

As one can see in Figure 3.13, gas composition varies with sample initial moisture content. Given the error bars, it is possible to consider that gas from 0 and 9 %wb initial moisture content samples have the same composition. Increasing the initial moisture content to 55 %wb leads to an increase in H_2 fraction from 26 to 38 %vol, a decrease in CO and CH_4 fractions from 43 to 31 %vol and from 13 to 8.5 %vol respectively, while CO_2 fractions remains stable. Yet, one should keep in mind that the total gas mass production dramatically increases at the same time. The rise in H_2 production is thought to be associated with syngas production by steam gasification of char.

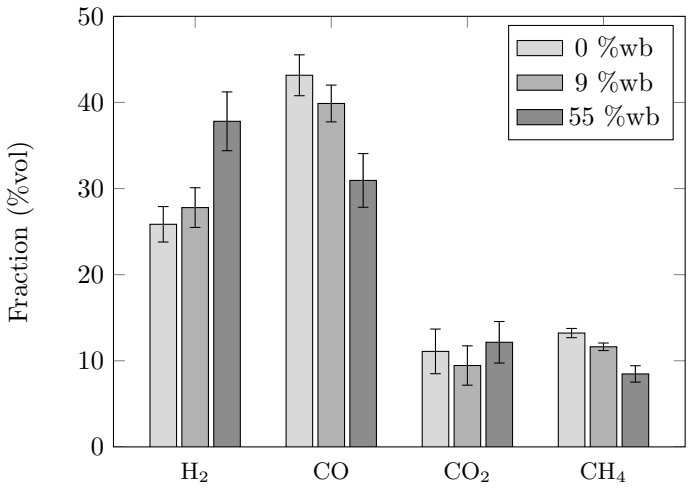

FIGURE 3.13: Major components of the gas for 0, 9 and 55 %wb moisture content bois de bout samples

Tar captured in cotton traps were analysed for 0 and 9 %wb initial moisture bois de bout samples. It was not possible to analyse tar produced by 55 %wb initial moisture content samples. Indeed, as aforementioned, the cotton traps contained almost no tar. Analysed tar compositions are similar. In the two configurations, the main products are primary and tertiary tar which are indicators of intense tar thermal cracking. Yet, 0 %wb initial moisture content sample tars exhibit a slightly wider variety of PAH. Steam reforming takes place to a greater exten for 9 % initial moisture content samples, which might explain the reduction in number of PAH

found in 9 %wb initial moisture content sample cotton traps.

Finally, average surface temperatures drops from about 1600 °C down to 1300 °C as biomass initial moisture content increases from 0 to 55 %wb (Table 3.1). This is thought to be a consequence of the endothermic char steam gasification reaction.

3.5 Energy balance

Energy balance of the system was calculated based on the method described in Section 2.6.2. In order to evaluate specific heat capacities and powers, it is mandatory to know the temperatures of the flue gas, the focal spot and the sample. Flue gas temperature was taken as 150 °C, in agreement with thermocouples measurements. Radiometer reported temperatures were used to calculate sample emitted power. Sample sensible heat is more challenging to evaluate. Indeed, temperature is not uniform throughout the sample. It was chosen to rely the pre-model predictions as well as thermocouple readings. Therefore, the sample sensible heat was determined considering a 250 g sample of which average temperature is about 50 °C. Table 3.7 reports the values of the different contributions to the energy balance as well as closure of this balance. The closure of the energy balance ranges from 87 to 104 % which is thought to be satisfactory.

Considering that at the process scale, gas, tar and char are the recoverable output energy carriers, it is interesting to evaluate the fraction of the input energy these products can contain. We consider the two energy inputs - incident radiative power and chemical power contained in wood - and the three energy outputs - chemical powers contained in gas, tar and char. Table 3.8 provides the fraction of the input power sources transferred to the three outputs for the six configurations. One can see that the total power contained in the outputs ranges as high as 94 % for dry samples down to 59 % for high initial moisture content samples. Gas contain about 45 % of the input power in any of the configurations. For high initial moisture content sample, the output power is only around half of the input power. It is indeed hindered by drying endothermicity.

For the six configurations, the total power contained in the outputs is higher than the wood input power, meaning that a fraction of the incident radiative power was converted into chemical form. The amount of converted radiative power is calculated by subtracting the wood HHV input from the total HHV output. Table 3.9 reports the amount of radiative power retained by the system outputs. The fraction of the input radiative power converted into chemical form ranges from 24 % for 9 %wb, bois de fil samples to 72 % for 0%wb, bois de bout samples. Furthermore, as for the energy conversion efficiency, bois de bout samples exhibit better performances than bois de fil samples.

Finally, in order to generalize the produced results, the wood consumption, water, char, gas and tar production rates for 1 kW of radiative power were calculated and

		Radiative input (W)	Wood HHV input (W)	Gas HHV output (W)	Tar HHV output (W)	Char HHV output (W)	Emitted power (W)	Water vaporisation power (W)	Flue gas sensible heat (W)	Sample sensible heat (W)	Closure (%)
Bois de bout	0 %wb	655	2233	1254	517	933	116	18	101	38	103
	9 %wb	655	1825	1137	159	732	101	59	99	38	94
	55 %wb	655	312	529	0	49	61	222	104	38	104
Bois de fil	0 %wb	655	2246	1095	584	792	122	2	99	38	94
	9 %wb	655	1798	1066	154	738	119	41	98	38	92
	55 %wb	655	470	576	0	89	80	97	97	38	87

TABLE 3.7: Inputs powers distribution between chemical outputs and losses

		Gas HHV output (%)	Tar HHV output (%)	Char HHV output (%)	Sum (%)
Bois de bout	0 %wb	43	18	32	94
	9 %wb	46	6	30	82
	55 %wb	55	0	5	60
Bois de fil	0 %wb	38	20	27	85
	9 %wb	43	6	30	80
	55 %wb	51	0	8	59

TABLE 3.8: Power distribution in system chemical outputs. All percentages are on a total power input basis (radiative + wood)

		Radiative input (W)	Wood HHV input (W)	Total HHV output (W)	Converted radiative power (W)	Converted radiative power fraction (%)
Bois de bout	0 %wb	655	2233	2704	471	72
	9 %wb	655	1825	2028	203	31
	55 %wb	655	312	578	266	41
Bois de fil	0 %wb	655	2246	2471	225	34
	9 %wb	655	1798	1958	160	24
	55 %wb	655	470	665	195	30

TABLE 3.9: Stored radiative power in the system outputs

Initial moisture content	Production/consumption rate (g/min/kW)				
	Wood	Water	Char	Gas	Tar
0 %wb	10.8 ± 0.73	0.41 ± 0.74	2.46 ± 0	5.92 ± 0.2	2.65 ± 1.42
9 %wb	8.73 ± 0.64	2.03 ± 0.65	2.1 ± 0	5.52 ± 0.23	0.76 ± 1.26
55 %wb	1.89 ± 0.04	6.46 ± 0.07	0.2 ± 0	2.78 ± 0.58	-1.28 ± 1.46

TABLE 3.10: Averaged wood consumption, water, char, gas and tar production rates per unit of incident power

reported in Table 3.10 for the different initial moisture contents. This approach should facilitate reactor design for instance. These data were produced by averaging bois de bout and bois de fil contributions because in a reactor samples are generally randomly oriented. In addition, the total outputs power is 90, 81 and 60 % of the total inputs power for 0, 9 and 55 %wb initial moisture content samples, respectively.

Conclusion

Thermally thick beech wood samples were exposed to radiative heat flux comparable to the ones found in solar power towers. To do so, a new experimental device was built. It allowed to investigate the behaviours of the biomass under heat fluxes

higher than 1000 suns.

An original behaviour has been highlighted. Under high radiative heat flux, sample geometry evolves dramatically during a run. A crater which mirrors incident heat flux distribution is formed. Two mechanisms of crater formation have been proposed: one involving sample shrinkage and mechanical failure for low initial moisture content samples, the other relying on char steam gasification for high initial moisture content samples.

It was shown that, even for high initial moisture content sample, water vaporisation did not suffice to lead to sample mechanical failure. Furthermore, produced chars do not undergo thermal annealing and exhibit high oxygen and hydrogen contents. Finally, achieved temperatures were high enough to promote tar thermal cracking, but not sufficient to induce carbon sublimation.

The effect of wood fiber orientation relative to the incident heat flux was questioned. Samples in bois de bout and bois de fil were used to address this question. Surprisingly, the produced results show that varying the sample orientation between these two extrema has only a minor effect on the sample behaviour.

The influence of the sample initial moisture content was investigated. It was highlighted that samples containing high initial moisture content undergo char gasification. They produce 2.6 times more gas - per unit of converted dry wood - than low initial moisture content samples. Furthermore, this gas is richer in H_2 - 36 %vol instead of 26 %vol. Nevertheless, the input power retained in the products is quite low, around 59 %. The tar yield is close to zero. It has also been shown that samples containing no water produce much more tar than moist samples. For these samples solar pyro-gasification exhibits a very good energy conversion efficiency: the recoverable products contain 90 % of the inputs (solar + wood) power. Furthermore, the power recovered in the outputs exceeds the wood input power alone, in every configuration. It means that some of the incident radiative power has been converted into chemical form. The fraction of the incident radiative power captured can be as high as 72 % for 0 %wb, bois de bout samples.

It can be concluded that the solar pyro-gasification of moist biomass is interesting for enhanced direct H_2 production with reduced tar yield, while solar pyro-gasification of dry biomass is advantageous in the perspective of solar to fuel conversion.

Furthermore, this experimental work yields substantial data which can be used to validate numerical model predictions.

CHAPTER 4

Numerical model

Introduction

This chapter describes the different steps that were followed during the development of the numerical model. The first parts of the chapter are classical model building stages, the last ones, on the contrary are specific to the modelling of biomass gasification under high solar heat flux.

The first part presents the objectives that were to be met by the model. In addition to properly describing biomass behaviour, the model aims at yielding a better understanding of the couplings at stake during biomass solar pyro-gasification.

The second part lists the different phenomena taking place during biomass degradation under high solar heat flux. It also explains why some of them are not considered in the model.

The third part reports the preliminary study that was conducted before building the model. This study is mainly based on dimensionless numbers. They are used to assess the validity of assumptions that are made, for instance the use of the Darcy's law and of one common temperature for the solid and gas phases.

The fourth part presents the numerical domain and the equations that are used to build the model. They can be summed up as classical convection diffusion equations in a reacting porous medium. The 2D axysymmetrical assumption used to model the geometry prevents the model from being able to describe bois de fil samples, hence, it is limited to bois de bout configurations.

The fifth part explains how the physical properties supplied to the model were chosen. Indeed, the model has to describe biomass behaviour over a large range of temperature. Therefore, a special care was taken in using temperature dependent correlations instead of constant values.

The sixth part introduces the method used to describe sample deformation. Indeed, the char produced by the pyrolysis is partially consumed by steam gasification, leaving sometimes no solid phase behind. In order to take this effect properly into account, the medium geometry has to evolve accordingly.

The seventh part presents how radiation penetration was taken into account. Radiation penetrates into the medium by two mechanisms: penetration through the sample porosity and penetration in between the char rods.

The last part describes the numerical methods that were used to solve the governing equations and the challenge faced for solving pressure equation.

4.1 Objectives

The numerical model was built in order to yield more insights about the behaviour of biomass under high solar heat flux. As a minimum, the model has to be able to satisfactorily capture the behaviour of the samples in the different initial moisture content conditions. Once that requirement is achieved, the model can be used to fulfil the following objectives:

a. Understanding the coupling between the different step of biomass degradation

b. Explaining what mechanisms lie behind sample deformation

4.2 Phenomena at stake

Before building the model, it is important to count the phenomena at stake during biomass solar pyro-gasification. Drying, pyrolysis and gasification take place at the same time inside of the sample. These transformations release gas that move throughout the medium. In addition, they have an impact on the medium temperature, which in turn has an impact on reaction rates. This configuration leads to numerous potential couplings.

These phenomena and their associated components can be categorized as:

- incident radiative heat flux: heat flux mapping, radiation interaction with the flue gas, radiation penetration into the medium
- heat and mass transfer inside of the sample: conductive, convective and radiative heat transfer as well as mass convection and diffusion
- heat and mass transfer outside of the sample: convective heat and mass transfer
- thermochemical conversion: wood pyrolysis, tar thermal cracking, tar steam reforming, char gasification
- phase change: drying
- geometry modification: wood shrinkage, char rod formation, char consumption by gasification

Among the listed phenomena, tar steam reforming will not be taken into account. Indeed, no kinetic model of intra-particular tar steam reforming is available.

Radiation interaction with the flue gas was also neglected. To assess the validity of this assumption, an estimation of the incident power absorbed by the atmosphere was computed. Knowing the composition of atmosphere above the sample, including H_2O and CO_2, its pressure and its temperature, an absorption spectrum was produced using HITRAN transition database [144]. Using this spectrum, it was possible to calculate that only 1 10^{-5} % of the incident power was absorbed.

Wood shrinkage resulting from drying or pyrolysis was not taken into account. Shrinkage induced by drying was neglected because it is thought that once dried, wood quickly undergoes pyrolysis, therefore limiting the amount of shrunk dried wood. Furthermore, wood shrinkage induced by drying is known to be anisotropic and of little magnitude [37]. It can reach up to 10 % on the tangential direction while remaining close to 0 on the longitudinal one [145]. Shrinkage induced by pyrolysis was not taken into account strictly speaking, yet its main consequence, i.e. char rods formation, was described using an homogeneous approach as described in Section 4.7.2.

4.3 Dimensionless numbers and assumptions

In order to get a first insight about the problems at hand, dimensionless numbers were calculated using characteristic values. They should be of help in determining the general behaviour of the sample. Then, they are used as guides to chose relevant assumptions during the model construction stage.

4.3.1 Dimensionless numbers

First, a radiative Biot number was calculated for wood (Eq. 4.1) using characteristic values of the physical properties available in Table 4.1. As expected, its value is greater than 1. The sample is therefore not thermally homogeneous.

$$Bi = \frac{\phi_{max} L_{sp}}{\lambda_{wood} \delta T} = 357 \tag{4.1}$$

Then, Damköhler III numbers were calculated for pyrolysis and gasification (Eq. 4.2 and 4.3). Both of them are greater than 1. Combined with the fact that Biot number is greater than 1, one can expect the presence of chemical fronts induced by thermal inhomogeneity for both pyrolysis and gasification.

$$Da_{III,\ pyro} = \frac{\phi}{k_{pyro} \rho_{wood} \Delta h_{pyro} L_{sp}} = 75 \tag{4.2}$$

$$Da_{III,\ gasi} = \frac{\phi}{k_{gasi} \rho_{char} \Delta h_{gasi} L_{sp}} = 116 \tag{4.3}$$

In addition, pore Reynolds number was calculated (Eq. 4.4). It is around 1, when evaluated in the most unfavourable case. Darcy's law can therefore be used to derive gas phase velocity with no need for inertial correction [97, 98].

$$Re_{pore} = \frac{\rho_g \|\boldsymbol{u_g}\| d_{pore}}{\mu_g} = 1.2 \tag{4.4}$$

Symbol	Property	Value	Dimension
c_{p_g}	gas phase heat capacity	1004	J/kg/K
$d_{benzene}$	benzene molecule diameter [146]	5.27	Å
d_{pore}	pore diameter	55.3	μm
k_B	Boltzmann constant	$1.380\ 10^{-23}$	J/K
k_{gasi}	gasification reaction rate at 800 °C	$2.0\ 10^{-4}$	1/s
k_{pyro}	pyrolysis reaction rate at 400 °C	$6.2\ 10^{-3}$	1/s
L_{sp}	sample characteristic length	0.05	m
p	pressure	101325	Pa
$\|\boldsymbol{u_g}\|$	gas phase Darcy's velocity magnitude (computed as $\|\boldsymbol{u_g}\| = \frac{\kappa_{char}}{\mu_g}\frac{\Delta p}{L_{sp}}$)	0.33	m/s
Δh_{gasi}	gasification reaction heat	1093.5	kJ/kg
Δh_{pyro}	pyrolysis reaction heat	80	kJ/kg
Δp	maximal internal overpressure [101]	30000	Pa
δT	characteristic temperature difference	1500	K
ζ	porosity	0.61	-
κ_{char}	char permeability [48]	$1.0\ 10^{-11}$	m^2
λ_g	gas phase thermal conductivity	0.026	W/m/K
λ_{wood}	sample thermal conductivity	0.1	W/m/K
μ_g	gas phase viscosity	$1.8\ 10^{-5}$	Pa.s
ρ_{char}	char density	85	kg/m^3
ρ_g	gas phase density	1.2	kg/m^3
ρ_{wood}	wood density	579	kg/m^3
ϕ_{max}	max incident heat flux	1072	kW/m^2

TABLE 4.1: Physical properties used for dimensionless numbers calculations

Pore thermal Péclet number was also calculated (Eq. 4.5). Its value is below 1. This has two main consequences: dispersive regime can be ignored [147] and local thermal equilibrium can be considered as achieved in the medium [99, 148]. Therefore, a single temperature field can be used to describe both solid and gas phase temperatures.

$$Pe_{pore} = \frac{\zeta \rho_g c_{p_g} \|\boldsymbol{u_g}\| d_{pore}}{\lambda_g} = 0.52 \tag{4.5}$$

Finally, Knudsen number was calculated for different conditions: wood at room temperature and char at 2000 K. The maximum value is far below 0.01 (Eq. 4.6). It is therefore possible to use continuum mechanics laws to describe the problem and neglected Knudsen diffusion.

$$Kn = \frac{k_B T}{\sqrt{2}\pi d_{benzene}^2 p d_{pore}} = 4.0\ 10^{-3} \tag{4.6}$$

Based on the different dimensionless numbers values, a schematic diagram of the sample during its degradation can be drawn (Fig. 4.1). Drying, pyrolysis and gasification take place at different depths inside of the sample. The gases they produce escape the porous medium though a high temperature char layer and are driven away by the nitrogen sweep.

4.3.2 Assumptions

Assumptions were drawn in order to build the numerical model. Most of them are classical assumptions used to model transport in porous medium; others are more specific to biomass degradation:

- wood and char are considered as anisotropic homogeneous porous media
- as discussed before, bois de bout samples are modelled using a 2D axisymmetrical geometry. It is made possible because wood and char radial and tangential physical properties values are close
- Darcy's law is used to derive gas phase velocity. This assumption is backed up by pore Reynolds number value
- a single temperature is used to describe solid and gas phase temperatures. This simplification is supported by pore thermal Péclet number value
- dispersive regimes are ignored, which is defended by pore thermal Péclet number value
- gases are assumed as ideal
- drying is described using a liquid-vapour equilibrium model
- pyrolysis is described using a pseudo-species model

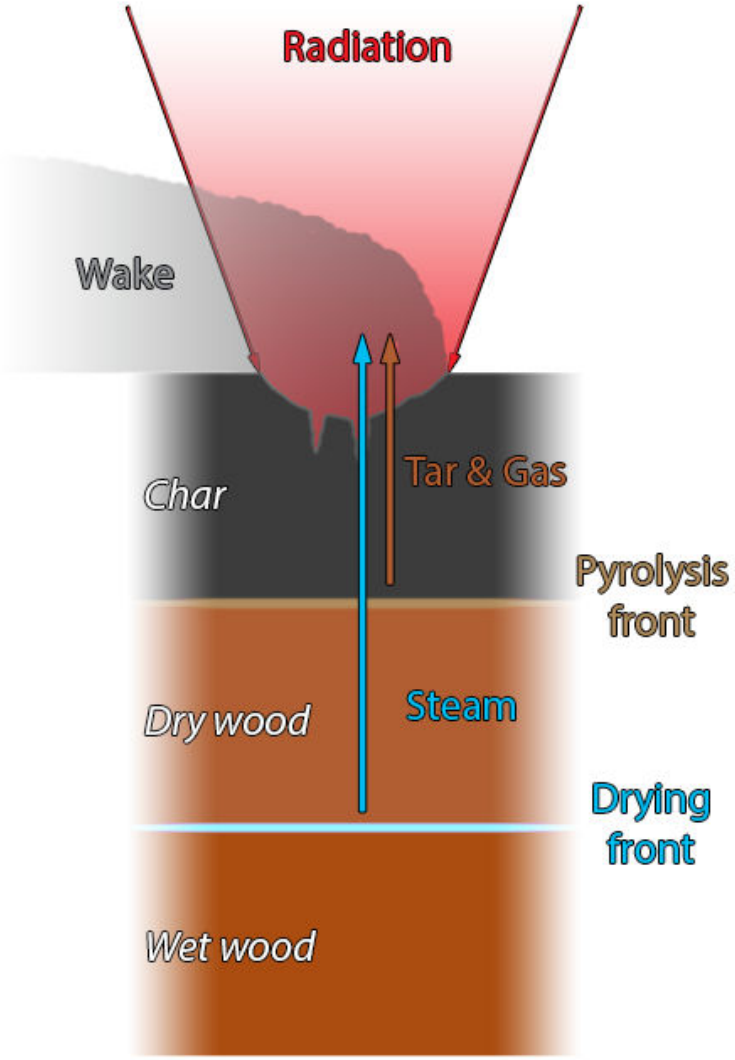

FIGURE 4.1: Schematic view of the sample during its degradation

- nine different species are considered: wood, gas, tar, refractory tar, intermediate solid, char, water, steam and air
- ash is not considered
- model molecules are used to set the physical properties of the different gaseous species: benzene is used as model molecule for tar, carbon monoxide for gas and nitrogen for air
- reaction heats are assumed to be constant even though temperature increases
- wood and char are assumed to be gray and diffuse materials, meaning that their emissivities equals their absorptivities

4.4 Numerical model

The numerical model aims at describing bois de bout samples under high solar heat flux. As stated before, these samples can be modelled as a 2D axsymmetrical domain into which conservation equations are solved.

4.4.1 Computational domain

The sample cylinder shape was reduced to wedge under the assumption that it can be modelled as 2D axsymmetrical (Fig. 4.2). Only bois de bout samples can be modelled using this method. Furthermore, it is only possible because a special care was taken in ensuring that the samples fibers were parallel to the incident heat flux. Nevertheless, some limitations to this approach exist; for instance, the nitrogen sweeping has a straight direction which is not compatible with 2D axsymmetrical modelling.

The sample is exposed to the incident heat flux on its top boundary. The top boundary also allows the gas phase to escape the medium. Side and bottom boundaries are adiabatic gas outlets.

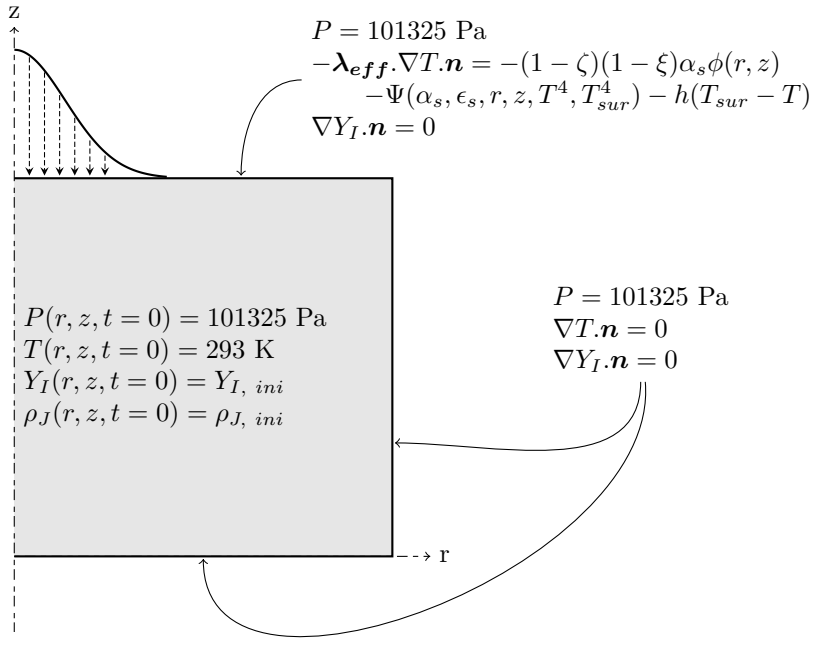

FIGURE 4.2: Computational domain, initial and boundary conditions

The mesh is made of regular prismal and tetrahedral cells. A mesh convergence study was led. It demonstrated that 4440 cells is the optimum.

4.4.2 Governing equations

The model is built around the three main equations: mass, momentum and heat conservations.

4.4.2.1 Mass balance

Solid species are immobile. They are governed by classical balance equations (Eq. 4.7):

$$\frac{\partial \rho_J}{\partial t} = \sum_{K=1}^{O} \nu_{J,K}\omega_K \tag{4.7}$$

Gaseous species move through convection and diffusion. They are governed by classical convection-diffusion equations (Eq. 4.8):

$$\frac{\partial \zeta \rho_g Y_I}{\partial t} + \nabla.(\rho_g \boldsymbol{u_g} Y_I) = -\nabla.(-\rho_g \boldsymbol{D_s} \times \boldsymbol{q_g} \nabla Y_I) + \sum_{K=1}^{O} \nu_{I,K}\omega_K \tag{4.8}$$

The sample boundaries considered as purely convective outlets (Eq. 4.9).

$$\nabla Y_I.\boldsymbol{n} = 0 \tag{4.9}$$

Initial wood and water densities are set as measured in Section 2.2.2. One should note that for convenience reasons, $Y_{steam,\ ini}$ is calculated by the model. Species initial values are summed up in Table 4.2.

$$\rho_J(r, z, t = 0) = \rho_{J,\ ini} \tag{4.10}$$

$$Y_I(r, z, t = 0) = Y_{I,\ ini} \tag{4.11}$$

Species	Initial density (kg/m^3)	Initial mass fraction
Wood	Variable (Table 2.3)	-
Water	Variable (Table 2.3)	-
Intermediate solid	0	-
Char	0	-
Gas	-	0
Tar	-	0
Refractory tar	-	0
Steam	-	Model calculated
Air	-	1 – $Y_{steam,\ ini}$

TABLE 4.2: Solid, liquid and gaseous phases initial conditions

4.4.2.2 Momentum balance

Gas flow through the sample is described using continuity (Eq. 4.12) combined with ideal gas assumption and Darcy's law.

$$\frac{\partial \zeta \rho_g}{\partial t} + \nabla.(\rho_g \boldsymbol{u_g}) = \sum_{K=1}^{O} \omega_K \tag{4.12}$$

The gas is assumed to behave as an ideal gas, thus its density can be expressed as:

$$\rho_g = \frac{pM_g}{\Re T} \tag{4.13}$$

Combining Eq. 4.12 and 4.13, we obtain Eq. 4.14:

$$\frac{\partial}{\partial t}\frac{\zeta M_g}{\Re T} p + \nabla.(\rho_g \boldsymbol{u_g}) = \sum_{K=1}^{O} \omega_K \tag{4.14}$$

$$\boldsymbol{u_g} = -\frac{\boldsymbol{\kappa_g} \times \boldsymbol{q_g}}{\mu_g}(\nabla p - \rho_g \boldsymbol{g}) \tag{4.15}$$

Then, combining Eq. 4.14 and 4.15, we obtain Eq. 4.16:

$$\frac{\partial}{\partial t}\frac{\zeta M_g}{\Re T} p - \nabla.(\rho_g \frac{\boldsymbol{\kappa_g} \times \boldsymbol{q_g}}{\mu_g}(\nabla p - \rho_g \boldsymbol{g})) = \sum_{K=1}^{O} \omega_K \tag{4.16}$$

The sample boundaries are considered to be outlets at atmospheric pressure (Eq. 4.17).

$$p = 101325 \text{ Pa} \tag{4.17}$$

Initially, the pressure inside of the sample is equal to the atmospheric pressure (Eq. 4.18).

$$p(r, z, t = 0) = 101325 \text{ Pa} \tag{4.18}$$

4.4.2.3 Heat balance

Temperature inside of the medium is governed by Eq. 4.19. It takes into account: heat convection, conduction, radiation with a special formulation of $\boldsymbol{\lambda_{eff}}$, heat sources and sinks associated with the medium transformation, radiation penetration into the medium as a source term (Q_{pen}, see Section 4.7.2) and heat transported by mass diffusive flux.

$$\begin{aligned}\frac{\partial(c_{p_s}\rho_s+\zeta c_{p_g}\rho_g+c_{p_{lw}}(\rho_{lw}+\rho_{bw}))T}{\partial t}+\nabla.(c_{p_{lw}}\rho_{lw}\boldsymbol{u_{lw}}T)+\nabla.(c_{p_g}\rho_g\boldsymbol{u_g}T)=\\ -\nabla.(-\boldsymbol{\lambda_{eff}}\nabla T)+\sum_{K=1}^{O}\omega_K\Delta h_K-\sum_{I=1}^{N}\nabla.(-c_{p_g}T\rho_g\boldsymbol{D_s}\times\boldsymbol{q_g}\nabla Y_I)\\ -\nabla.(-c_{p_{lw}}T\boldsymbol{D_{bw}}\nabla\rho_{bw})+Q_{pen}\end{aligned} \tag{4.19}$$

Properly predicting temperature is important because it has an impact on biomass degradation rate and thus on the global behaviour of the model. Therefore, a special care was taken in selecting the medium thermal conductivity model. A wide variety of models exist, ranging from simple classical weighed average estimation [149] to complex consideration on wood pore structure [150]. It was chosen to rely on the most advanced model (Eq. 4.20 [143]), which is a modified version of Saastamoinen and Richard model, in order to include high temperature char thermal conductivity measurements.

$$\boldsymbol{\lambda_{eff}}=\begin{pmatrix}(1-\zeta^{2/3})\frac{\lambda_s}{1.9}+\frac{\zeta^{2/3}}{\frac{1-\zeta^{1/3}}{2\frac{\lambda_s}{1.9}}+\frac{\zeta^{1/3}}{\lambda_g}} & 0\\ 0 & (1-\zeta^{2/3})\lambda_s+\frac{\zeta^{2/3}}{\frac{1-\zeta^{1/3}}{2\lambda_s}+\frac{\zeta^{1/3}}{\lambda_g}}\end{pmatrix} \tag{4.20}$$

The temperature top boundary condition accounts for radiative heating, as well as radiative and convective losses (Eq. 4.21). Coefficients multiplying the incident heat flux account for radiation absorption and penetration into the medium (see Section 4.7). $\Psi(r,z,T^4,T_{sur}^4)$ account for radiative losses. Yet, Ψ is a function taking into account the top surface shape. Indeed, when a the crater forms, the cells inside of the crater to do not have the same view factor toward the surrounding. They also emit and receive energy from the crater inner surface. In order to take this phenomenon into account, the crater internal view factor are computed assuming it has a cone shape [151]. The convective heat loss coefficient was chosen as $h = 7.0$ W/m^2/K according to the correlation for average heat transfer coefficient over flat plate for a laminar flow provided in [152].

$$-\boldsymbol{\lambda_{eff}}.\nabla T.\boldsymbol{n}=-(1-\zeta)(1-\xi)\alpha_s\phi(r,z)-\Psi(\alpha_s,\epsilon_s,r,z,T^4,T_{sur}^4)-h(T_{sur}-T) \tag{4.21}$$

Side and bottom boundaries are considered to be adiabatic (Eq. 4.22).

$$\nabla T.\boldsymbol{n}=0 \tag{4.22}$$

Initially, the temperature is the ambient temperature throughout the sample (Eq. 4.23).

$$T(r,z,t=0)=20\ ^\circ\text{C} \tag{4.23}$$

4.4.3 Drying model

During a run, water vaporises and moves through the sample. Some of the produced steam travels to a colder area where it could condense. It was thought that thermal models and Arrhenius type models would be too simplistic to accurately describe these phenomena. Drying was therefore modelled using liquid-vapour equilibrium featuring liquid, bound water and steam transport. This model is extensively described in [89]. Only its main features will be described here.

The liquid-vapour equilibrium was described using Eq. 4.24:

$$p_{sat}(T(K)) = \exp(7.3649\ 10^{1} + \frac{-7.2582\ 10^{3}}{T} - 7.3037\ \log(T) + 4.1653\ 10^{-6} T^{2})\ \text{Pa} \tag{4.24}$$

Water motion throughout the sample can be divided into bound water diffusion (according to the diffusion coefficient $\boldsymbol{D_{bw}}$) and liquid water convection under liquid pressure gradient (Eq. 4.25, with δp_{cap} the capillary pressure drop).

$$\boldsymbol{u_{lw}} = -\frac{\boldsymbol{\kappa_{lw}} \times \boldsymbol{q_{lw}}}{\mu_{lw}} (\nabla(p - \delta p_{cap}) - \rho_{lw} \boldsymbol{g}) \tag{4.25}$$

Where $\boldsymbol{q}$ represents the relative permeability tensors (Eq. 4.26 and 4.27). q_g and q_{lw} take into account the fact that when a pore is full of water ($S = 1$), the gas permeability tends toward 0.

$$\boldsymbol{q_g} = \begin{pmatrix} 1 + (2S - 3)S^2 & 0 \\ 0 & 1 + (4S - 5)S^4 \end{pmatrix} \tag{4.26}$$

$$\boldsymbol{q_{lw}} = \begin{pmatrix} S^3 & 0 \\ 0 & S^8 \end{pmatrix} \tag{4.27}$$

4.4.4 Biomass degradation scheme

Four alternative models are available to describe beech wood degradation: pseudo-species models, cellulose, hemicellulose and lignin models, Ranzi model and FG-DVC models. Among them, the two last options seemed over qualified for the task at hand. Indeed, given the uncertainty associated with medium physical properties, the quality of their predictions would be hindered by slight misprediction of the temperature field and species transport. Between, the two first options, it was chosen to resort on comparison led in literature [104] which advised a pseudo-species model.

Pyrolysis is described using a pseudo-species model which is the combination of existing models (Fig. 4.3). One should note that even if the degradation model components were chosen with care, it was not possible to find in literature kinetic parameters derived for our conditions, i.e. 250 K/min heating rate and high final temperature. The closest available kinetic parameters were therefore chosen

[55, 63, 103, 104]. These parameters been validated against 50 to 100 K/min heating rates experiments, with a pyrolysis final temperature around 600 °C. Furthermore, this model does not predict gas nor tar compositions.

The specificity of the chosen model is the use of an *intermediate solid* pseudo-specie to mimic lignin. Indeed, lignin is the main precursor of char and its degradation is known to be exothermic. Intermediate solid behaviour is set accordingly, i.e. it degrades into char releasing heat.

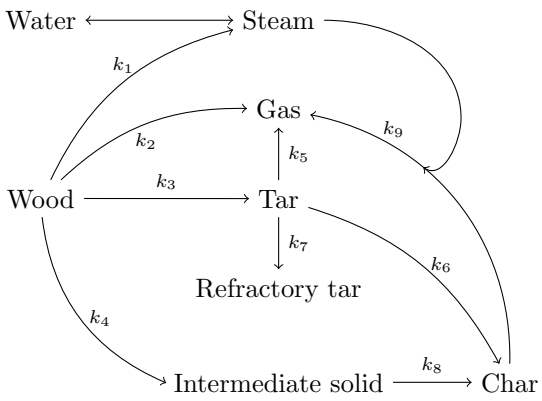

FIGURE 4.3: Biomass drying model and pyrolysis scheme

Number	Reaction	A (1/s)	Ea (kJ/mol)	Δh (kJ/kg)	Reference
1	Wood $\mapsto$ steam	4.38 10^9 $\times$ a	152.7	-80	[63, 104]
2	Wood $\mapsto$ gas	4.38 10^9	152.7	-80	[104]
3	Wood $\mapsto$ tar	1.08 10^{10} $\times$ (1-a)	148.0	-80	[63, 104]
4	Wood $\mapsto$ intermediate solid	3.75 10^6 $\times$ b	111.7	-80	[104]
5	Tar $\mapsto$ gas	2.15 10^{11}	141.0	42	[103]
6	Tar $\mapsto$ char	1.0 10^5	108.0	42	[103]
7	Tar $\mapsto$ refractory tar	1.16 10^{11}	141.0	42	[103]
8	Intermediate solid $\mapsto$ char	1.38 10^{10}	161.0	300	[104]

TABLE 4.3: Kinetic parameter for beech wood pyrolysis. a = 0.219 [63] and b = 2

Reaction rates follow first order kinetics. They are therefore obtained by multiplying reaction rate coefficients (Eq. 4.28) by reagent density and $\nu_{I,J}$ coefficients, according to Eq. 4.29 for gases reagents and to Eq. 4.30 for solid reagents. $\nu_{I,J,K}$ are stoichiometric coefficients taking the value of 0 or 1 according to the degradation scheme (Fig. 4.3).

$$k_K = A_K \exp(\frac{Ea_K}{\Re T}) \tag{4.28}$$

$$\omega_K = k_K \rho_g \prod_{I=1}^{N} \nu_{I,K} \zeta Y_I \tag{4.29}$$

$$\omega_K = k_K \prod_{J=1}^{M} \nu_{J,K} \rho_J \tag{4.30}$$

Gasification reaction rate features both char density and steam mass fraction dependency (Eq. 4.31). It was established for the steam gasification of char obtained from flash beech wood pyrolysis [113].

$$\omega_{gasi} = \omega_9 = 4.20\ 10^4\ \exp(\frac{150750}{\Re T})\rho_{char}^{0.58}\zeta Y_{steam} \tag{4.31}$$

Modifications were applied to the kinetic schemes found in literature. The first one is the introduction of water production in the pyrolysis scheme. According to [63], 21.9 % of the tar produced by beech wood flash pyrolysis is in fact water. A repartition factor, called a, was therefore applied to derive pyrolysis water production.

In order to get credible results, it was mandatory to modify pyrolysis scheme char production. Indeed, the initially produced amount of char was extremely low and led to a 98 % porosity char, which is not credible. One should keep in mind that the used kinetic scheme has not been tested for high pyrolysis final temperature. The char production kinetic parameter was corrected by a factor called b, taken as 2. Given the intrinsic weakness that is the dependency on these kinetic schemes, it was chosen to keep the correction factor with only one significant digit. This correction yields char with 95 % porosity, which is in agreement with the literature dealing with high temperature pyrolysis [42].

4.5 Physical properties

In order to accurately model the solar pyro-gasification of wood, it is key to know its physical properties. As stated before, there is a wide range of variability hidden behind the name *wood*. Physical properties can vary by one order of magnitude from species to species [18].

The model developed in this work is based on heat, momentum and mass balances. Therefore, the physical properties of interest are : porosity, density, thermal conductivity, specific heat capacity, radiation absorptivity, permeability and mass diffusivity. As for other porous media, porosity is the central physical property because is has an impact on every other physical properties at the Darcy's scale.

Finally, one should keep in mind that wood is an anisotropic material. Heat and mass transfers are favoured in the fiber direction. Yet, the apparition of cracks in the structure can locally modify heat and mass transfer patterns [153].

4.5.1 Solid phases

4.5.1.1 Wood

Dry wood porosity ranges from 40 to 60% [121]. Regarding beech wood, the pore mean diameter is 55.3 ± 11.7 μm [154] while the largest pores have a diameter of 500 μm [34].

Because of its anisotropy, measuring wood thermal conductivity is a challenging task that was undertaken by several authors. Thermal conductivity is deduced from heat diffusion coefficient and specific heat capacity measurements [155]. Authors have gathered measurements over a wide range of wood species and conditions such as temperature or moisture [32]. Some of them make an explicit difference between the directions, others not. As a general rule, one can state that wood thermal conductivity is around 0.1 W/m/K in the fiber direction. This value can be divided by 2 in the two other directions.

Wood radiation absorptivity is usually considered to be high. Measurements in both IR and visible ranges show a wide spectral variation of the absorptivity. In the IR range, absorptivity was reported to vary between 0.80 and 0.90 depending on the radiation source temperature [82, 156]. While is was reported to be close to 0.50 in the visible range [157]. It was therefore chosen to rely on the values that were calculated based on our measurements (Section 2.2.2). Wood absorptivity was also examined with respect to wood thermal breakdown level. It was shown to flatten dramatically by increasing in the visible range while slightly decreasing in the IR [157].

The chosen values of beech wood the physical properties are available in Table 4.4. The properties that could not be measured were taken from literature. When a choice had to be made between two correlations, the one with the wider validity range was preferred. A summary of a wood physical properties literature survey can be found in Tables B.1 and B.2 in Appendix B.

4.5.1.2 Char

Char is a porous material. Its porosity is therefore a key parameter that controls every physical property of this material. However, char porosity is known to vary with pyrolysis conditions, i.e. heating rate and final temperature. For instance, for the same final temperature, a porosity of 88 was reported % with a heating rate of 900 K/min while it was 73 % for a heating rate of 2.6 K/min [47]. Furthermore, during gasification char porosity increases until char is fully consumed.

Classically, reported value of char thermal conductivity are about 0.1 W/m/K at room temperature. It is important to note that because char is a very porous material, radiative heat transfer occurs inside of it and thus increases its effective thermal conductivity. For an insulating material similar to char, a multiplication by 6 of the thermal conductivity between 20 and 1127 °C was reported [159]. There is

a wide variety of models taking this contribution into account ranging from basic Rossland [160] and to more complex models [150, 161]. To this date, only one study reports measurement of char thermal conductivity at high temperature (900 °C) [143]; others are limited to 300 °C.

Char physical properties are also modified by its geometry at a higher level than the pore scale. At the macroscopic scale, both high heating rate and gasification can induce cracks [14, 47]. These cracks have an impact on local thermal and hydrodynamic properties, yet no work could be found on that subject.

Char emissivity is considered to be close to 1 because of its dark color and the numerous cavities it exhibits on its surface. Nevertheless, only two measurements for beech could be found in literature: 0.94 in [162] and 0.88 [109]. These values are coherent with an in depth study led on plywood [163].

The chosen values of char physical properties are available in Table 4.5. Except absorptivity, all the values come from literature. A summary of a char physical properties literature survey can be found in Tables B.3 and B.4 in Appendix B. Some needed physical properties of char are not readily available in literature; they have therefore been estimated.

Char porosity being unknown and varying thoughout the medium, is calculated using char intrinsic density taken as $\rho_{char,\ intrinsic} = 1700$ kg/m^3 [49] according to Eq. 4.32.

$$\zeta_{char} = 1 - \frac{\rho_{char}}{\rho_{char,\ intrinsic}} \tag{4.32}$$

Only longitudinal values were available for char permeability [48]. It was chosen to keep wood permeability anisotropic ratio to build char permeability tensor (Eq. 4.33).

$$\boldsymbol{\kappa_{char}} = 1\ 10^{-11} \begin{pmatrix} 99.7\ 10^{-6} & 0 \\ 0 & 1 \end{pmatrix} \tag{4.33}$$

Char mass diffusion coefficient was not available in literature. It was chosen to keep wood diffusivity tensor and correct it by char/wood porosity ratio (Eq. 4.34).

$$\boldsymbol{D_{char}} = \frac{\zeta_{char}}{\zeta_{wood}} \boldsymbol{D_{wood}} \tag{4.34}$$

4.5.1.3 Solid phase properties evaluation

Solid phase properties are calculated as the weighed average of wood and char properties (Eq. 4.35). Intermediate solid phase is considered as char when calculating the physical properties.

$$\boldsymbol{\kappa_s} = \frac{\rho_{wood}\boldsymbol{\kappa_{wood}} + (\rho_{is} + \rho_{char})\boldsymbol{\kappa_{char}}}{\rho_{wood} + \rho_{is} + \rho_{char}} \tag{4.35}$$

$\boldsymbol{D_s}$ is the mass diffusion coefficient. Being directly measured in wood [34], it does not need to be multiplied by the classical ζ/τ correction that is used to evaluate the diffusion coefficient in porous medium based on gas diffusivity. Mass diffusion coefficient are known to evolve with temperature [164]. Unfortunately, no law governing the evolution of this coefficient was found in literature. It was therefore chosen to affect a classical temperature dependency for diffusion coefficient (Eq. 4.36 [165]).

$$\boldsymbol{D_s}(T(K)) = \boldsymbol{D_s}|_{293\ K}(\frac{T}{293})^{1.5} \tag{4.36}$$

4.5.2 Gas phase

Gas phase properties are calculated as the weighed average of every single gaseous species properties (Eq. 4.37). Individual gas phase properties are available in Appendix C.

$$c_{p_g} = \sum_{I=1}^{N} c_{p_I} Y_I \tag{4.37}$$

In order to take into account the fact that the pore can be full of water ($S = 1$), a special equation is used for gas phase thermal conductivity (Eq. 4.38).

$$\lambda_g = S\lambda_{lw} + (1 - S)\sum_{I=1}^{N} \lambda_I Y_I \tag{4.38}$$

4.6 Moving mesh strategy

As experimentally observed, steam gasification consumes the char produced by pyrolysis, leading to a disappearance of the medium. In terms of numerical modelling, this translates into the fact that solid phase density can reach 0 kg/m^3 at the top boundary cells. In order to correctly take this phenomenon into account, a solid medium deformation strategy has to be implemented.

Phase field method has successfully been used in literature for a similar case [115]. This kind of method assigns a field to the solid medium, generally varying between 0 and 1. This field can move on a fixed mesh, describing the solid medium shape evolution. Yet, it did not seem adapted to radiative heat transfer in the way it is described in this model. Indeed, in order to properly take into account the radiative heating contribution, penalized cells with very high thermal conductivity would be required in order to transfer radiative heat to the solid medium boundary as fast as possible.

Symbol	Property	Value	Dimension	Note
α_{wood}	Absorptivity	0.37	-	Measured
ϵ_{wood}	Emissivity	0.37	-	Assumed
$c_{p_{wood}}$	Specific heat capacity	2300 - 1150 exp(-0.0055 T(°C))	J/kg/K	[88]
$\lambda_{long,\ wood}$	Thermal conductivity	0.291 + 2.759 10^{-4}T(°C)	W/m/K	[155]
$\boldsymbol{\kappa_{wood}}$	Permeability tensor	$\begin{pmatrix} 367\ 10^{-18} & 0 \\ 0 & 742\ 10^{-15} \end{pmatrix}$	m^2	[158]
$\boldsymbol{D_{wood}}$	Mass diffusivity tensor	$\begin{pmatrix} 4.8\ 10^{-10} & 0 \\ 0 & 86\ 10^{-10} \end{pmatrix}$	m^2/s	[158]
ζ_{wood}	Porosity	Variable (Table 2.3)	-	Measured

TABLE 4.4: Chosen physical properties for beech wood

Symbol	Property	Value	Dimension	Note
α_{char}	Char absorptivity	0.88	-	Measured
ϵ_{char}	Char emissivity	0.88	-	Assumed
$c_{p_{char}}$	Char specific heat capacity	1430 + 0.355 T(K) - $\frac{7.3210\ 10^7}{T(K)^2}$	J/kg/K	[88]
$\lambda_{long,\ char}$	Char longitudinal thermal conductivity	2.3584 – 1.4962 10^{-2}T(°C) + 3.8483 10^{-5}T(°C)^2 - 4.3292 10^{-8}T(°C)^3 + 1.8595 10^{-11}T(°C)^4	W/m/K	[143]
$\boldsymbol{\kappa_{char}}$	Char permeability tensor	Eq. 4.33	m^2	Estimated [48]
$\boldsymbol{D_{char}}$	Char mass diffusivity tensor	Eq. 4.34	m^2/s	Estimated
ζ_{char}	Char porosity	Eq. 4.32	-	Estimated

TABLE 4.5: Chosen physical properties for char

Arbitrary Lagrangian Eulerian technique [117] allows to deform a mesh and can therefore be a solution to property take into account the radiative boundary condition. With this technique, the velocity is affected to mesh cells and solved fields are corrected to prevent the mesh velocity from inducing errors. This approach was successfully used to model space shuttle ablative thermal shield behaviour [116]. Yet, it requires an heavy reformulation of the model equations and the determination of a mesh velocity properly describing solid phase geometry evolution.

A third way was chosen: mesh interpolation, for it does not require governing equations reformulation nor mesh velocity determination. With this technique an ablation criterion is set, in our case when char porosity exceeds 0.975 (or $\rho_{char} < 42.5$ kg/m^3, Fig. 4.4, A). When a cell satisfies this criterion, the mesh evolves in such a way that it simulates solid phase ablation (Fig. 4.4, B and C).

Once the mesh has been updated, the solved fields need to be recalculated so that they would reflect char ablation. First, the cells overlapping volumes between the former and the current mesh are computed. Then, the solved fields are interpolated based on the overlapping volumes (Fig. 4.4, D). In order to ensure that mass and energy are conserved, the special treatment has to be applied to the top row cells. The solid mass and energy remaining in the ablated cell is added to the cell below, therefore, no mass nor energy disappears. The same is done with the two cells that neighbours the ablated cell. Indeed, in the process of moving the ablated cell, half of their volumes disappears. It is taken into account to prevent mass or energy disappearance. Finally, when interpolating the solved fields, gaseous species are left free to escape the medium.

Once the mesh has been updated and the solved fields interpolated, the simulation carries on using the modified geometry (Fig. 4.4, E).

This technique is quite easy to understand and allows for great flexibility. Yet, it has one main drawback: it is heavy to implement (or even impossible to implement in closed-source solvers). Implementing this technique required to use a numerical solver allowing for a great level of freedom in terms of source code modifying. This is why the open source OpenFOAM CFD framework was chosen to implement the model.

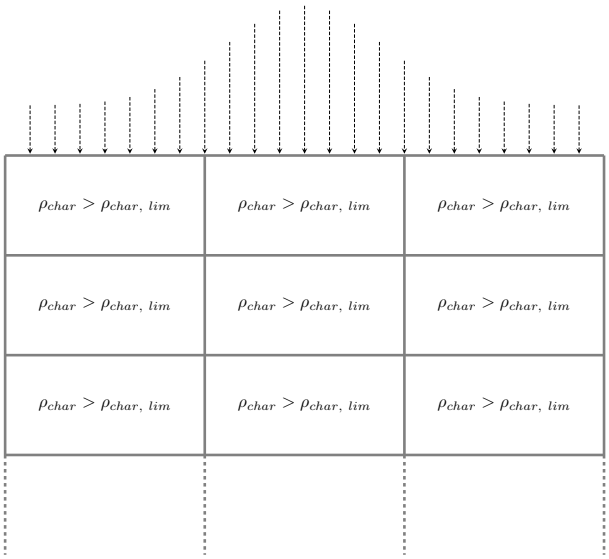

(A) No cell satisfies the ablation criterion

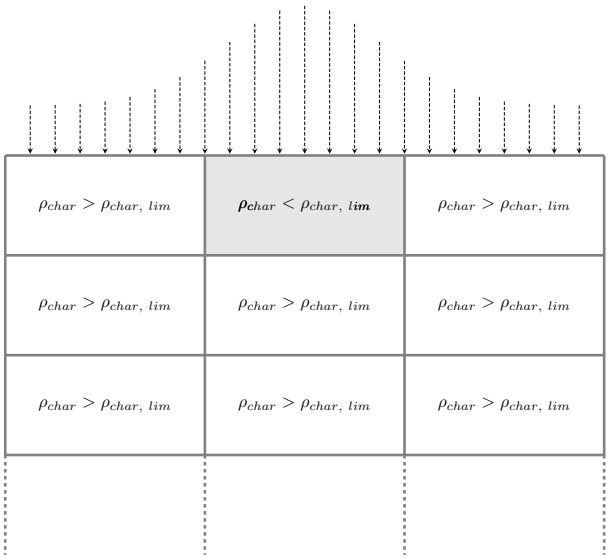

(B) Gray cell satisfies the ablation criterion

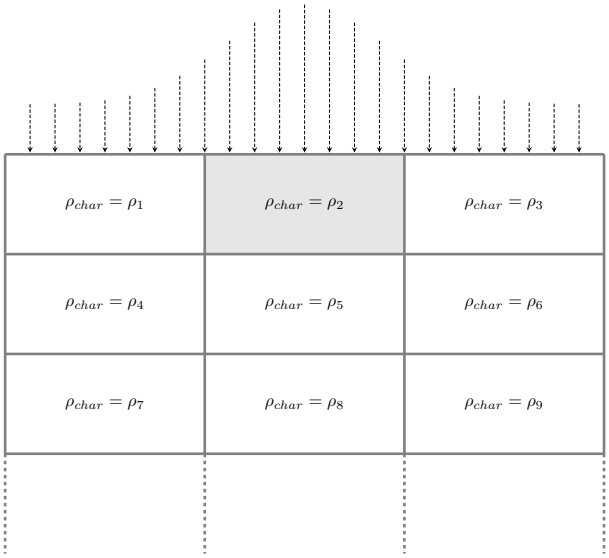

(C) Fields before mesh motion are stored for future recalculation

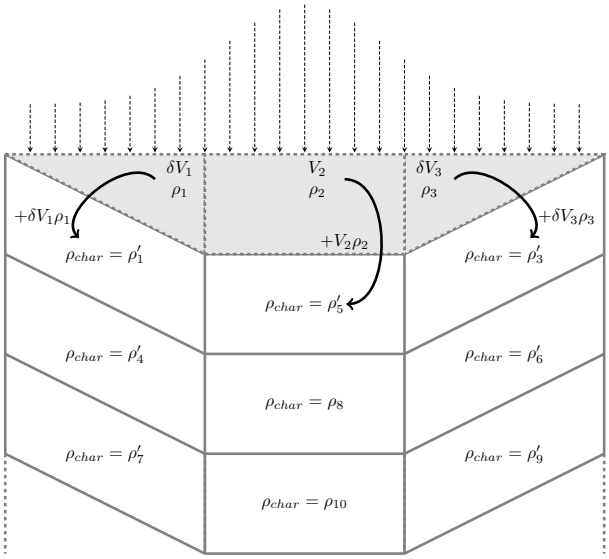

(D) Mesh is moved and fields are interpolated

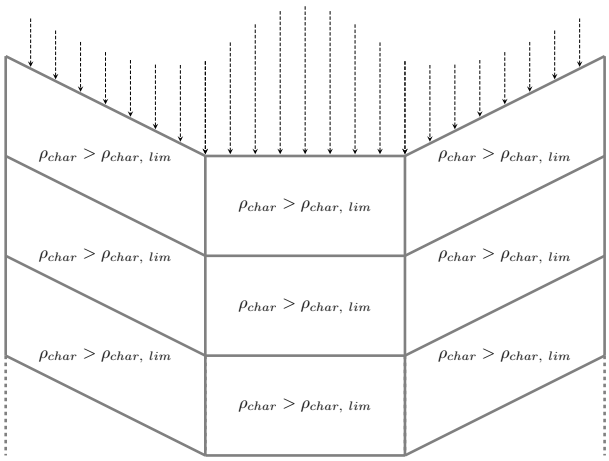

(E) No cell satisfies the ablation criterion, the simulation carries on

FIGURE 4.4: Mesh motion technique

4.7 Radiation penetration strategies

Radiation penetrates the medium at two levels: close to the surface, inside of wood and char porosity (referred as *near surface penetration*); in between char rods directly to the bottom of the crater (referred as *in depth penetration*). The radiative power that penetrates the medium is taken into account as a source term: Q_{pen}.

4.7.1 Near surface penetration

The incident radiation penetrates the medium thought wood and char porosity. Indeed, beech wood pores mean diameter (55.3 μm [154]) is much greater than the incident radiation wavelength: radiation behaves ballistically in the medium porous geometry.

Radiation penetration length was estimated to be around 52 μm into wood and 66 μm into char (Appendix D). Near surface penetration has been implemented into model. If the penetration depth is larger than the cell height, the penetrating incident power is uniformly distributed over the cells until the penetration depth is reached.

4.7.2 In depth penetration

The incident radiation also penetrates the medium in between char rods. Deforming the mesh in order to describe each and every rod was not accessible. Therefore, an homogeneous approach was chosen. The crater is considered to be char and is described using char physical properties. A volume field (Q_{pen}) is built in order to take into account, in the heat balance equation, the radiative power which penetrates into the sample. This field is constructed considering that a fraction (ξ) of the incident power reaching the top boundary of the sample propagates ballistically through the char crater. The remaining fraction ($1-\xi$) of the incident radiative power is distributed between the top boundary and the char upper surface porosity following the near surface penetration model (see Section 4.7.1). The in depth penetrating power propagates into the medium until it reaches the pyrolysis front, defined as the first cell where $\rho_{wood} > \rho_{is} + \rho_{char}$. Half of it is uniformly absorbed on its way to the bottom of the crater. The remaining half is absorbed once it reaches the pyrolysis front. There, it is distributed following the radiation near surface penetration model. Then, the Q_{pen} field is built by dividing, in every cell, the local amount of penetrating power by the cell volume. Once built, the Q_{pen} field is treated as a source term in the heat balance equation (Eq. 4.19).

Four different approaches were tested in order to model in depth radiation penetration. These approaches are detailed in Figure 4.5. Then their results are compared to experimental observations (Fig. 3.9). For the sake of simplicity, mesh motion was deactivated while producing illustrating results (Fig. 4.6). 0 %wb initial

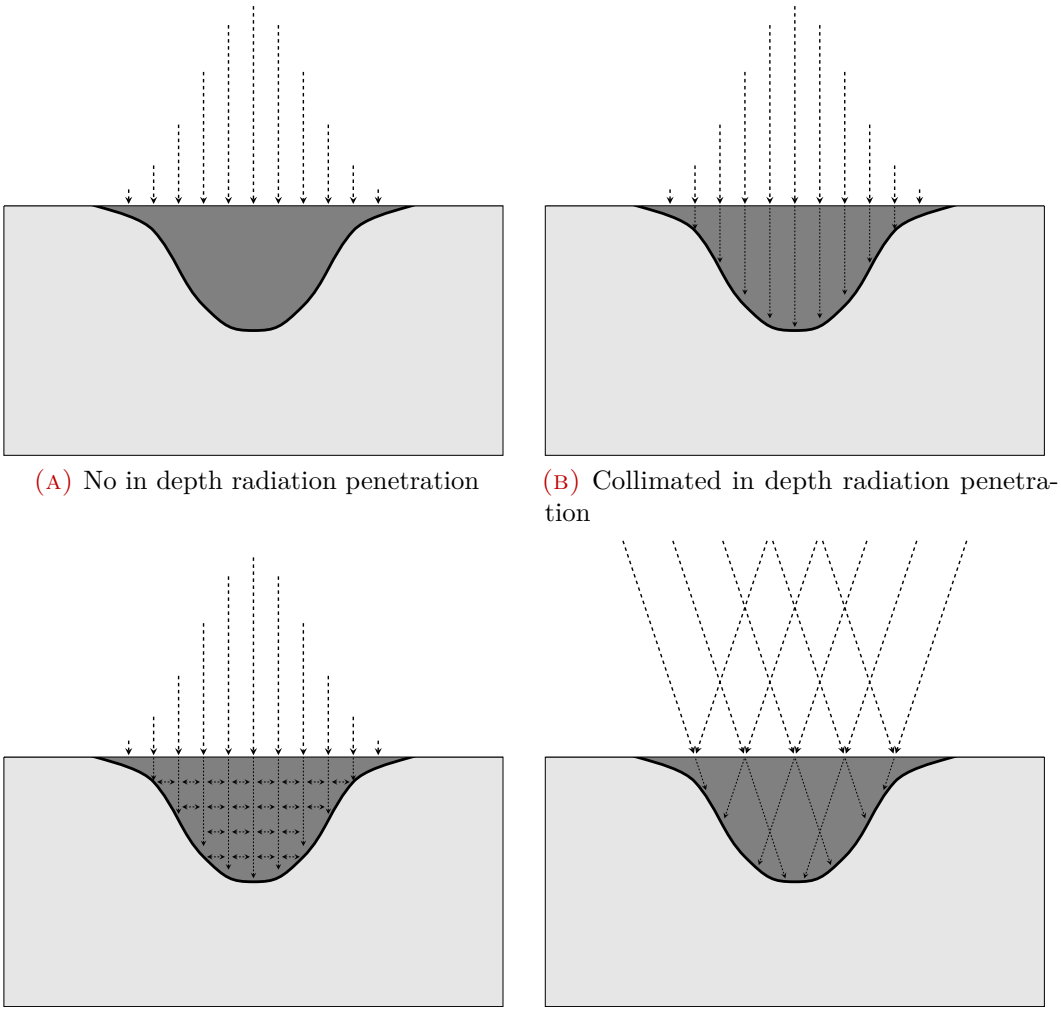

(A) No in depth radiation penetration

(B) Collimated in depth radiation penetration

(C) Collimated in depth radiation penetration with internal emission

(D) Uncollimated in depth radiation penetration

FIGURE 4.5: Radiation penetration strategies. Light gray: wood, dark gray: char

moisture content cases were chosen to illustrate the different penetration strategies because the initial lack for water reduces the error induced by mesh deformation and char gasification deactivation.

At first, no radiation penetration was considered (Fig. 4.5 A), i.e. $\xi = 0$ and $Q_{pen}(r, z, t) = 0$. As a result, a layer of char appears on the upper part of the sample (Fig. 4.6 A). This layer has a low thermal conductivity and acts as a thermal shield, preventing the pyrolysis of the major part of the sample. This approach fails to reproduce experimentally observed sample behaviour.

Then, radiation is considered to be vertical and collimated. It is allowed to penetrate the medium until it reaches the pyrolysis front (Fig. 4.5 B). The amount of radiation penetrating the medium is determined considering usual wood to char shrinkage proportion. It is known that char volume is 65 % lower than the initial wood volume. Thus, for a surface, the contraction would be around 50 %

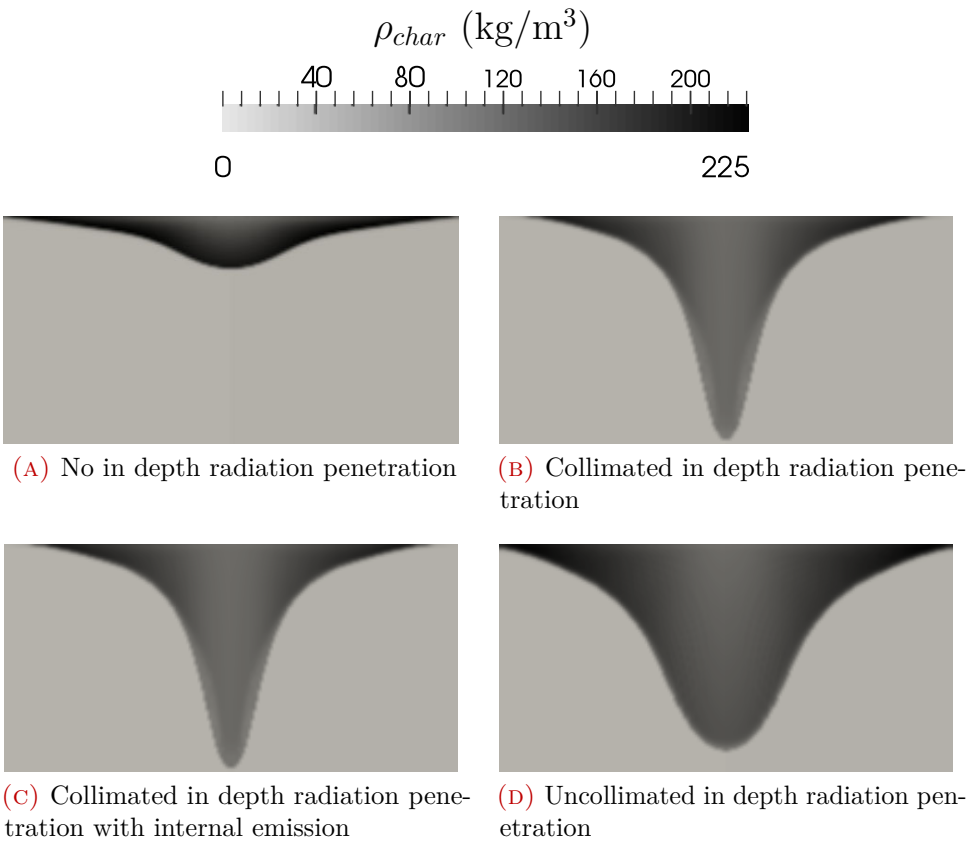

(A) No in depth radiation penetration

(B) Collimated in depth radiation penetration

(C) Collimated in depth radiation penetration with internal emission

(D) Uncollimated in depth radiation penetration

FIGURE 4.6: Radiation penetration strategies results for 0 %wb initial moisture content bois de bout cases after a 5 minutes exposure (mesh deformation and char gasification deactivated). Colormap: char density

($\xi = 0.50$). This value was confirmed by image processing method of char crater picture (Fig. 3.8). The numerical results show a char crater (Fig. 4.6 B). Yet, its shape and depth do not match experimental observations. The crater is too sharp.

Two mechanisms were envisioned to explain the flattening of the crater. The first one is internal rod to rod radiation which could greatly enhance radial heat transfer (Fig. 4.5 C). By considering that the gap between the char rods is negligible before their height and by linearising radiative heat transfer, using Rossland model [160], it is possible to associate a thermal conductivity to internal radiation. Then, an effective radial thermal conductivity is built considering that char and radiative thermal conductivities are in serial configuration. Taking internal radiation into account did change the results by 2 % in terms of crater depth (Fig. 4.6 C). It is therefore thought that it is not the main crater flattening mechanism.

Finally, in the actual configuration, the incident radiation is not collimated. The 12.98° aperture angle of the incident beam was taken into account (Fig. 4.5 D). Considering that all the beams cross at the same point and knowing the beam aperture angle and the focal spot radius, it is possible to determine this crossing point. This point is used as a homothetic center (H) to project the incident heat flux on the pyrolysis front (Fig. 4.7). The predicted crater shape is in good agreement

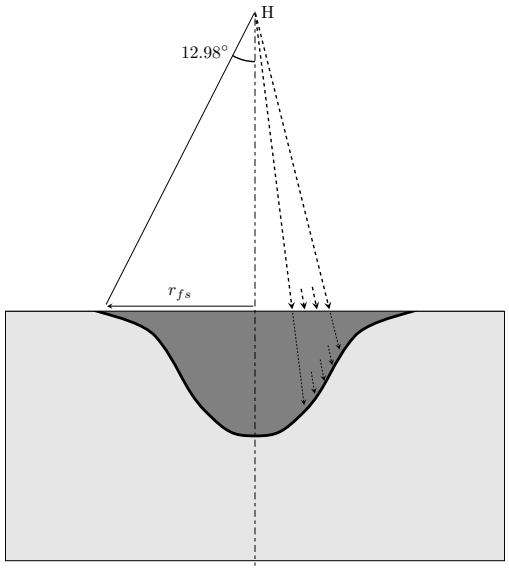

FIGURE 4.7: Radiation in depth penetration strategy. On the left: homothetic center construction, on the right: incident heat flux projection

with experimental observations (Fig. 4.6 D). It is therefore though that incident radiation aperture angle is the crater flattening phenomenon.

4.8 Numerical methods

The governing equations were implemented and solved using the open source OpenFOAM CFD framework [166, 167]. It was chosen because the accessibility of its source code allowed for the implementation of moving mesh and radiation penetration strategies.

OpenFOAM offers a wide variety of numerical schemes for time and space differencing. A second order backward scheme was chosen for time integration. Source terms were solved implicitly when possible.

Linear differencing was used for spatial differencing. Regarding divergence differencing, off-centred limited schemes, such as Van Leer or Gamma schemes, were tried. Despite their high computational cost, they did not improve the results quality.

After a solver tolerance convergence study, equations solvers tolerances were set to 10^{-12}, except for pressure which was set to 10^{-18}. Solving pressure equation is a challenging task in this particular case. Indeed, sharp porosity discontinuity, induced by the pyrolysis front, creates spurious fluxes in the pressure matrix. These fluxes can, in turn, lead to artefacts in the pressure fields (Fig. 4.8). This problem can be solved for a given range of Darcy's number in the case isotropic porous media, without mass source term [168]. The method mainly consists in

implicitly solving the flow resistance. Applying this method to our case did not produce any improvement. According to the creator of the proposed method, it remains a state of the art problem for anisotropic cases with mass source terms. Nevertheless, it was checked that, at the sample scale, mass conversation was not hindered by this problem. Yet, regarding individual mass fractions, 10 % errors may be induced with a sum of the mass fractions varying between 0.90 and 1.10.

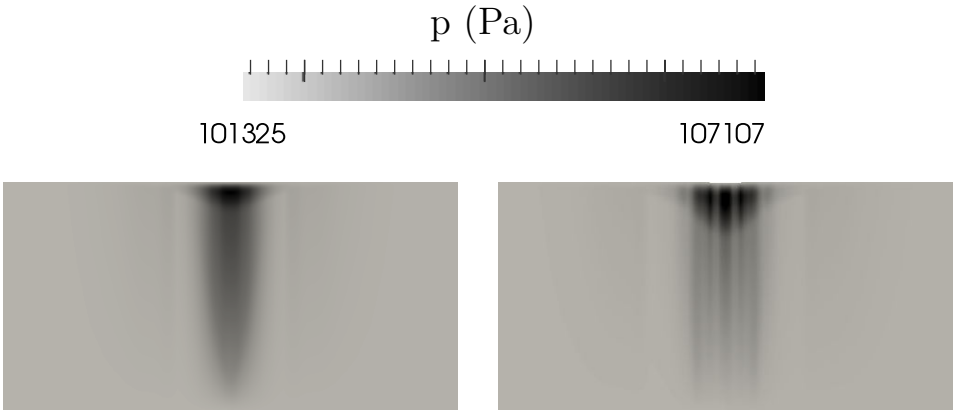

(A) A pressure field without artefact (B) A pressure field with artefacts

FIGURE 4.8: Two pressure fields in the reference case (9 %wb, bois de bout)

Time step was constrained by a Courant number and a maximum vaporisation rate. The Courant number was the most restrictive criterion. A time step convergence study showed that no further improvement could be obtained by lowering the maximum Courant number below 0.5, which was therefore chosen as maximum Courant number value.

Conclusion

This chapter presented the numerical model used in the modelling part of this work. This model is based on three main conservation equations: mass, momentum and heat balances. These equations are coupled with liquid-vapour equilibrium drying model and pseudo-species biomass degradation model. Assumptions made to write these equations are defended using dimensionless numbers. Because of biomass solar pyro-gasification specific nature, i.e. medium gasification and radiation penetration, special strategies have been implemented to describe medium shape evolution and incident heat flux penetration into the crater geometry. Finally, it was shown that beam spreading is the mechanism that controls the crater shape.

CHAPTER 5

Numerical results

Introduction

This chapter presents the results produced by the numerical model. The two first parts assess the validity of the model predictions. Once the validity of the model has been established, further insights on biomass solar pyro-gasification are derived from its predictions. Finally, the robustness of the choices made for the construction of the model is assessed through sensitivity analyses.

The first part deals with the validation of the assumptions that were made in order to build the model. Key dimensionless number values are verified to be within reasonable bounds so that assumptions validity is not hindered.

The second part compares numerical model predictions with experimental observations. The numerical model results are analysed qualitatively by comparing numerical and experimental geometries and quantitatively by confronting predicted and observed temperature and time averaged production/consumption rates.

The third part analyses the predicted behaviour of biomass. Using the model, further insights on biomass behaviour under high solar heat flux are derived and couplings between different phenomena at stake are highlighted.

The last part reports the results of different sensitivity analyses. Drying and pyrolysis models were modified in order to assess their impact on the model results. Furthermore, the impact of the fitting parameter b on the general behaviour of the model was analysed using a sensitivity analysis.

5.1 Assumptions validation

In order to assess the model construction assumptions validity, key dimensionless numbers were extracted at every time step. Their maximum values were then confronted with the critical values that they should not exceed.

The maximum reported value for pore Reynolds number is 0.15. It remains below the critical value of 1 and thus validates the choice of the uncorrected Darcy's law for deriving velocity from pressure gradient.

The maximum value taken by the pore Péclet number is 7.1 10^{-2} which is below 1. It validates the use of one temperature field to describe both solid and gas phase temperatures.

The highest reported value of Knudsen is 3.3 10^{-3}. This value being below 0.01; the laws of continuum mechanics could be used without any need for corrections.

In addition, and as a token of the quality of this model, mass and energy

conservation were checked at the sample scale. Over a run, mass and energy are conserved at more than 99.9 %.

5.2 Comparison with experimental observations

Before analysing model predictions in depth, numerical results are compared to experimental observations in order to assess their validity.

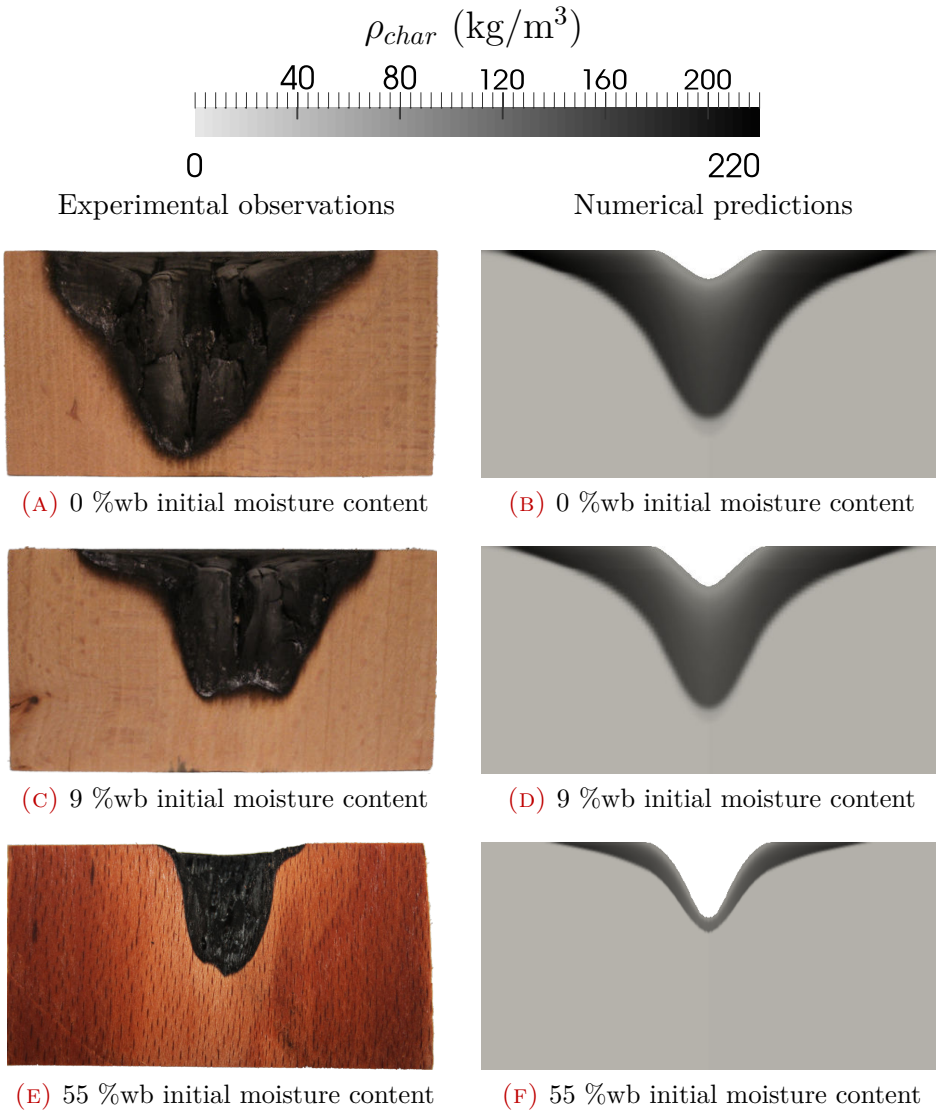

(A) 0 %wb initial moisture content

(B) 0 %wb initial moisture content

(C) 9 %wb initial moisture content

(D) 9 %wb initial moisture content

(E) 55 %wb initial moisture content

(F) 55 %wb initial moisture content

FIGURE 5.1: Experimental and numerical crater cut views. Colormap: char density

On a qualitative level, the predicted sample geometries and the char density fields are compared with the experimental observations for the three different initial moisture contents (Fig. 5.1). The predicted crater depths and widths are close to the ones experimentally observed. It is a token of the quality of the solid fields

evolution prediction.

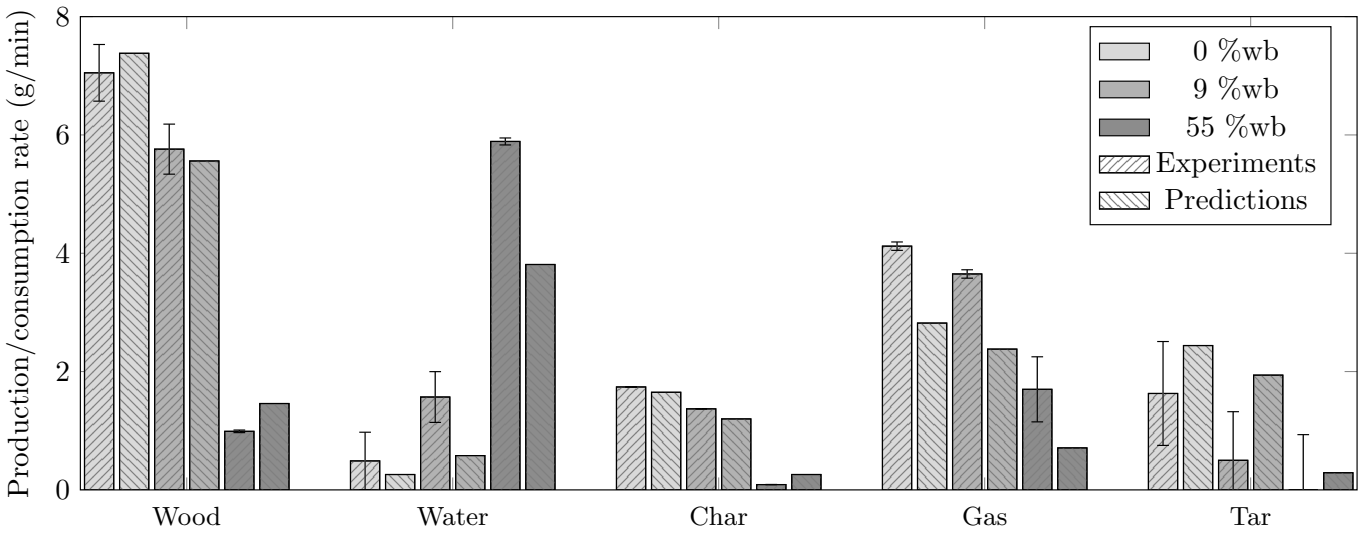

FIGURE 5.2: Experimental and numerical time averaged production/consumption rates for the bois de bout configurations

Time averaged rates (g/min)	0 %wb		9 %wb		55 %wb	
	Exp.	Num.	Exp.	Num.	Exp.	Num.
Wood	7.05 ± 0.48	7.38	5.76 ± 0.42	5.56	0.99 ± 0.02	1.46
Water	0.49 ± 0.49	0.26	1.57 ± 0.43	0.58	5.89 ± 0.06	3.81
Char	1.74 ± 0.002	1.65	1.37 ± 0.002	1.20	0.09 ± 0.002	0.26
Gas	4.12 ± 0.07	2.82	3.65 ± 0.07	2.38	1.70 ± 0.55	0.71
Tar	1.63 ± 0.88	2.44	0.50 ± 0.82	1.94	0 ± 0.93	0.29

TABLE 5.1: Observed and predicted time averaged production/consumption rates

On a quantitative level, the predicted time averaged production/consumption rates can be compared with the experimental ones (Table 5.1). The numerical time averaged production/consumption rates were calculated using the same method as the experimental ones, in order to allow for a more direct comparison. Figure 5.2 reports the predicted versus observed time averaged production/consumption rates. Wood consumption and char production rates are very well predicted by the model. Gas production rate is underestimated by the model in all cases, while tar production rate is overestimated. Nevertheless, the evolution of these rates with initial moisture content is well captured. Three factors may explain these discrepancies. First, the biomass degradation model may excessively favour tar production over gas production. Second, tar may undergo steam reforming inside of the sample, which is not accounted for in the model. Third, in the experiments, tar may undergo thermal cracking and steam reforming outside of the sample, therefore increasing gas production. These extra-particular chemical reactions are not taken into account in the model, hindering the possibility of a direct comparison between experimental

observations and numerical predictions.

The model underestimates the water production rate in all cases, while its evolution with sample initial moisture content is well captured. The explanation of this discrepancy could be challenging. Indeed, numerous factors could contribute to a misprediction of the amount of water leaving the sample, e.g. hydrodynamic properties, pyrolysis water yield, ... Identifying the relevant one might be out of reach without experimental observations of the water distribution inside of the sample.

Because it mediates the transformation of wood into char, intermediate solid field can be used as a marker of pyrolysis progress throughout the sample. The intermediate solid field exhibits a front shape (Fig. 5.3). It is therefore used as a flag for pyrolysis front: its position and thickness are compared with the experimental observations. Table 5.2 reports the model predictions for the surface temperature, the crater depth and the pyrolysis front thickness. The predicted values for the surface temperature and the pyrolysis front thickness are close to the experimental ones. Regarding the char crater depth, discrepancies of 15 % exist. Yet, the trends are well captured for wide variations of initial moisture content.

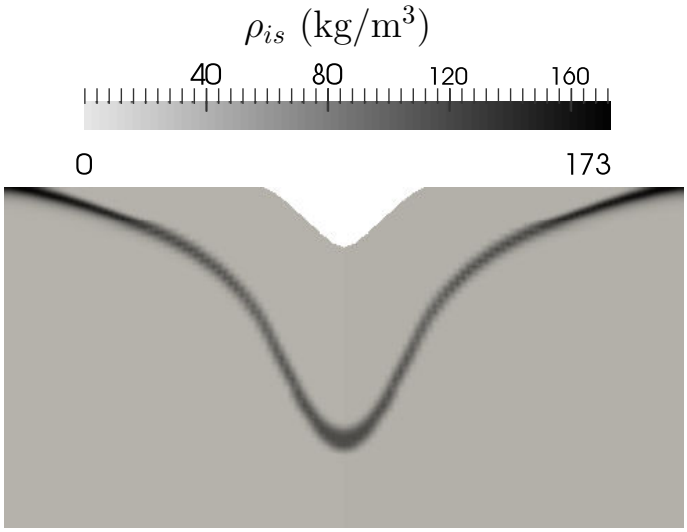

FIGURE 5.3: Intermediate solid density field after 5 minutes, for the reference case (9 %wb, bois de bout). Colormap: intermediate solid density

5.3 General behaviour

Given the good agreement between the numerical model predictions and the experimental observations, it is thought to be possible to further analyse biomass behaviour under high solar heat flux using the model predictions.

As a general comment, the degradation of a thermally thick sample of biomass under high solar heat flux induces drying, pyrolysis and gasification fronts inside of

	0 %wb		9 %wb		55 %wb	
	Exp.	Num.	Exp.	Num.	Exp.	Num.
Surface temperature (°C)	1594 ± 123	1515	1530 ± 120	1526	1317 ± 98	1337
Crater depth (cm)	4.5	3.9	3.2	3.7	2.4	2.2
Pyrolysis front thickness (mm)	4	4	3	4	0.5	0.5

TABLE 5.2: Observed and predicted surface temperature, crater depth and pyrolysis front final thickness

the sample. This general behaviour is in good agreement with the dimensionless number predictions. The main part (about 90 %) of the produced gases are forced toward the top boundary and therefore go through a high temperature char layer before escaping from the medium. This configuration is very likely to lead to physical couplings between the phenomena at stake during biomass degradation under high solar heat flux.

5.3.1 Drying

During a run, a drying front can be observed for the three initial moisture contents. The water density field exhibits the same shape in all cases. The field can be divided into three zones (Fig. 5.4 and Fig. 5.5):

- a dry zone (in light gray on Fig. 5.4), where the temperature is far above 100 °C
- a condensation zone (in black on Fig. 5.4), in which steam is forced by the pressure gradient. In this zone, steam condenses. Condensation being exothermic, steam condenses until the temperature reaches a value close to 100 °C and moisture content rises to an equilibrium value of 84 kg/m^3
- an unmodified zone (in dark gray on Fig. 5.4), where the moisture is equal to the initial moisture content, because no steam has condensed in this zone

For 0 %wb initial moisture content samples, water originates from wood pyrolysis only. Indeed, pyrolysis produces steam that is forced, for a part, toward cold regions of the sample where it condenses. For 9 and 55 %wb initial moisture content samples, water is both initially present in the medium and produced by pyrolysis. Nevertheless, one should keep in mind that, even if it is credible, this described behaviour cannot be validated by direct experimental observation.

Finally, as experimentally observed, the overpressures induced by fast drying remain low, with a characteristic value of 10000 Pa which remains far below beech wood radial tensile strength of 75 MPa [169]. These overpressures are therefore not sufficient to lead to sample mechanical failure.

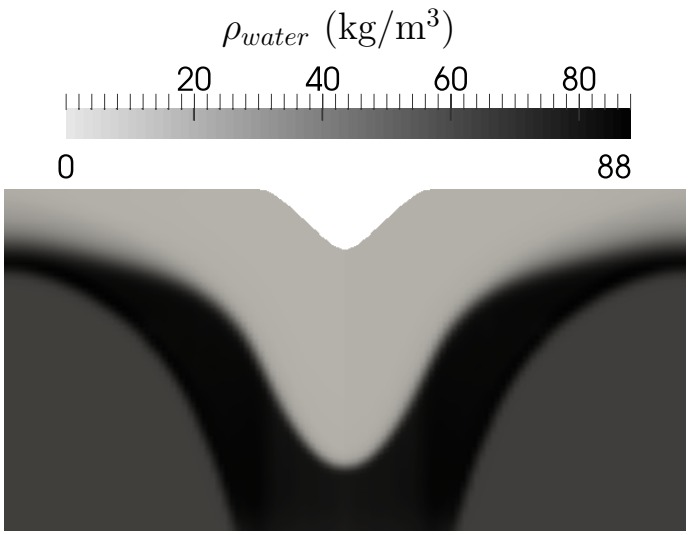

FIGURE 5.4: Water density field after 5 minutes, for the reference case (9 %wb, bois de bout). Colormap: water density

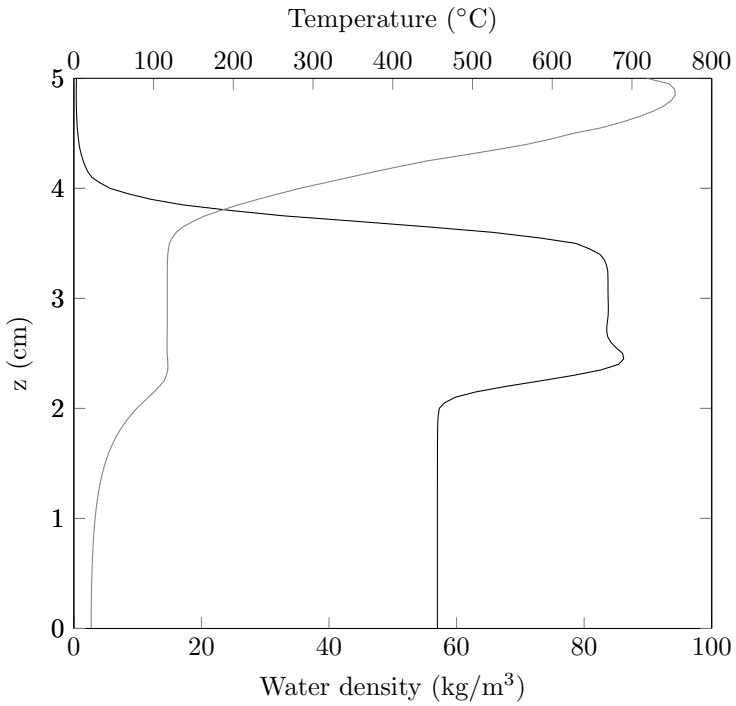

FIGURE 5.5: Water density and temperature along the vertical axis at r = 2.5 cm after 5 minutes, for the reference case (9 %wb, bois de bout). Black line: water density, gray line: temperature

5.3.2 Tar production

During a run, the degrading sample releases tar. If temperature is high enough, tar can undergo thermal cracking, turning them into gas and refractory tar. The model reports that both tar and refractory tar are produced during a run. The cohabitation of tar and refractory tar could result from:

- partial thermal cracking, because residence time and temperature would not be sufficient to fully crack the tar before they escape the sample
- the coexistence of a low temperature tar producing zone and a high temperature zone cracking tar into refractory tar

Figure 5.6 reports tar and refractory tar mass fractions, as well as temperature, along the top boundary of the sample after 2 minutes and 30 seconds of exposure for the reference case (9 %wb, bois de bout). The surface of the sample can be divided into two zones: an inner, high temperature zone ($r < 3.7$ cm and $T > 450$ °C) and an outer low temperature zone ($r > 3.7$ cm and $T < 450$ °C). The model predicts that uncracked tar escapes the sample by the low temperature zone at the periphery of the sample, while tar crossing the center of the sample undergoes thermal cracking and escapes the medium as refractory tar and gas.

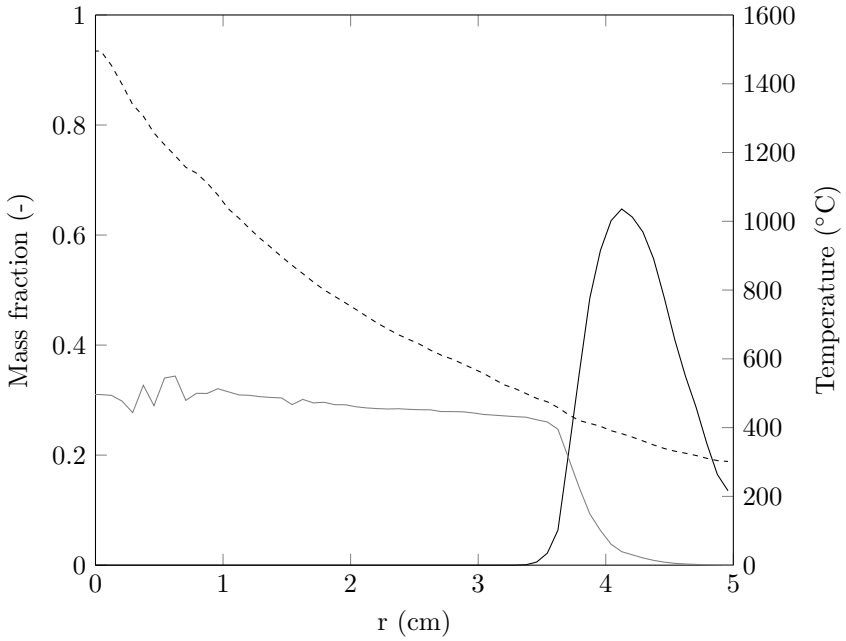

FIGURE 5.6: Temperature, tar and refractory tar mass fractions along the top boundary after 2 minutes and 30 seconds, for the reference case (9 %wb, bois de bout). Black line: tar, gray line: refractory tar, dashed line: temperature

Time dependent gas productions, experimentally observed and numerically predicted, are reported in Figure 5.7. As stated before, the model underpredicts sample gas production. Furthermore, the model does not capture the trend of the experimental curve. Indeed, the experimentally reported gas production increases with time while the numerically predicted one flattens. The difference between the two trends can be used to derive indirect insights on tar history. The experimentally reported increase in sample gas production could lead to an acceleration of pyrolysis. Yet, the model which properly predicts solid fields evolution negates such a possibility. This rise may therefore come from an increase of the tar thermal cracking and steam reforming. This increase is made possible by the deepening of the crater which

induces a higher tar residence time in a high temperature medium. Yet, the model, which only accounts for intra-particular tar thermal cracking, does not predict this increase. Altogether, this leads to think that extra particular tar cracking and tar steam reforming play a major role in the evolution of the gaseous products distribution. External CFD study would thus be required in order to improve gaseous products distribution prediction.

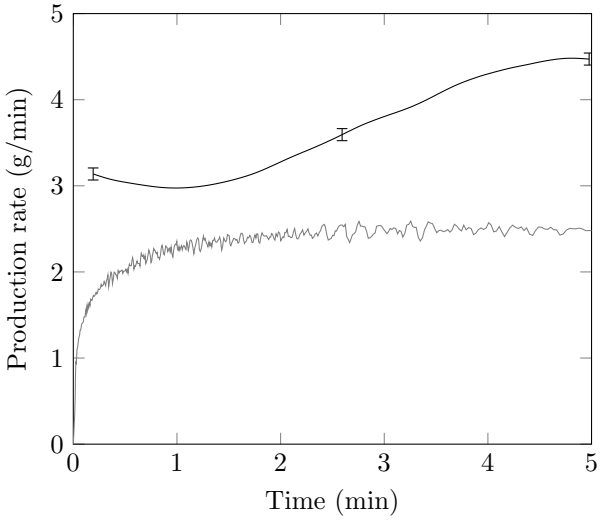

FIGURE 5.7: Experimental and numerical time dependent gas productions, for the reference case (9 %wb, bois de bout). Black line: experimental result, gray line: numerical prediction

Figures 5.6 and 5.7 exhibit oscillations on the numerically predicted tar curves. They are thought to come from pressure solving artefacts presented in Section 4.8. It is especially true for Figure 5.6, where oscillations are limited to the left part of the curve. Indeed, this part corresponds to a zone where biomass has undergone pyrolysis and therefore a strong porosity gradient exists.

5.3.3 Char steam gasification

The numerical model confirms that water is forced out of the sample through the high temperature char layer. This configuration could allow char steam gasification to take place inside of the char crater.

Two different mechanisms could explain the computational domain deformation: very low char production, i.e. the produced amount of char would not be sufficient to overpass the deformation criterion ($\zeta > 0.975$) or steam gasification of the char produced by pyrolysis.

In order to differentiate the importance of the two phenomena, gasification was deactivated for a set of simulations. In this condition, no deformation of the computational domain could be observed. It can therefore be concluded that the amount of char produced by pyrolysis is sufficient to prevent the porosity to exceed

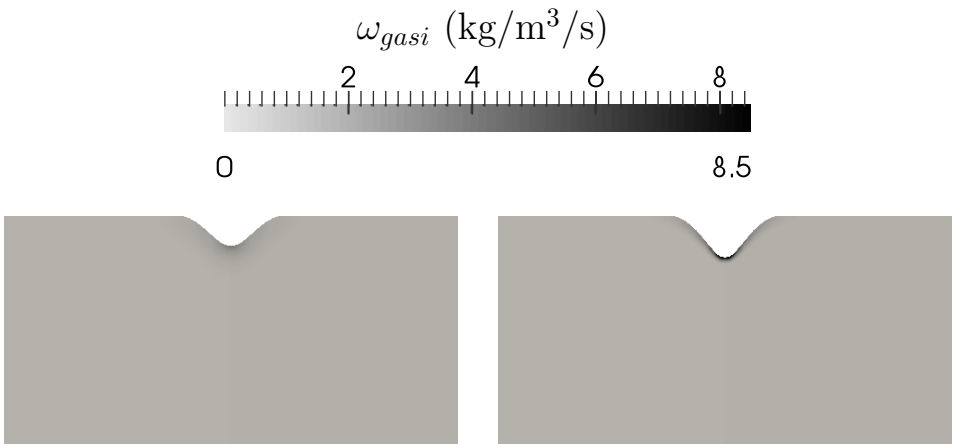

(A) 9 %wb initial moisture content (B) 55 %wb initial moisture content

FIGURE 5.8: Gasification reaction rate fields for 9 and 55 %wb initial moisture content cases, after 2 minutes and 30 seconds. Colormap: gasification reaction rate

0.975.

Figure 5.8 reports the char steam gasification reaction rate for both 9 and 55 %wb initial moisture content cases after 2 minutes and 30 seconds of exposure. Char steam gasification exclusively consumes char very close to the upper boundary, where temperature is high enough. Gasification is therefore the main phenomenon behind medium ablation.

Char steam gasification is much more intense for high initial moisture content samples, with a maximum rate of 8.5 kg/m^3/s, while it peaks at 2.5 kg/m^3/s for 9 %wb initial moisture content samples. Given char steam gasification endothermicity, this difference of intensity explains the lower top surface temperature both experimentally observed and numerically predicted for high initial moisture content samples (Table 5.2).

5.4 Sensitivity analyses

Three key choices were made during the building steps of the model: the choice of the drying model, the choice of the pyrolysis model and the correction to the chosen pyrolysis model. The impact of these choices is here investigated through sensitivity analyses. For the model choices, it was done by implementing other models and comparing their predictions. For the correction factor, it was done, classically, by modifying its value.

5.4.1 Sensitivity to the drying model

The chosen drying model is based on a liquid-vapour equilibrium approach. It is known to produce high quality results at the price of an heavy implementation and a considerable CPU time load during the simulation. It was chosen to compare

its predictions to an Arrhenius type drying model featuring vaporisation and condensation [94]. This model uses a temperature threshold of 95 °C above which water evaporates and below which it can condense (Eq. 5.1 and 5.2). Yet, this model does not make the distinction between bound and free waters and does not consider their motions. Finally, in this model, mass transport physical properties are not affected by pore water content, i.e. $\boldsymbol{q_g} = \boldsymbol{I}$.

$$\omega_{lw \mapsto steam} = 5.13\ 10^6\ \exp(\frac{87900}{\Re T})\rho_{lw} \quad \text{if T} > 95\ ^\circ\text{C} \tag{5.1}$$

$$\omega_{steam \mapsto lw} = 21500\ \|\boldsymbol{u_g}\|\rho_g Y_{steam} \quad \text{if T} < 95\ ^\circ\text{C} \tag{5.2}$$

Table 5.3 reports the results of the benchmark between the two drying models (variations being calculated according to Eq. 5.3). For 0 %wb initial moisture content case, only minor differences (under 4 %) appear on a global level between the two predictions. Figure 5.9 shows the repartition of the water inside of the sample predicted by the two models. The Arrhenius type model overpredicts the thickness of the area where water condenses inside of the sample, while the total amount of water retained in the sample is in agreement with liquid-vapour equilibrium model prediction.

$$\text{Variation} = \frac{\text{Altertative value - Reference value}}{\text{Reference value}} \tag{5.3}$$

	Initial moisture content		
	0 %wb	9 %wb	55 %wb
Surface temperature	-0.4	-0.9	3.5
Crater depth	-2.6	0.0	5
Pyrolysis front thickness	0.0	0.0	0.0
Time averaged rates:			
Wood	-1.9	-0.5	4.1
Water	3.8	-22.4	-38.4
Char	-1.8	0.0	3.8
Gas	-1.4	-2.5	5.8
Tar	-2.5	-1.0	45.2

TABLE 5.3: Variations (in %) between liquid-vapour equilibrium model and Arrhenius type model

For 9 and 55 %wb initial moisture content cases, Arrhenius type model substantially underpredicts the amount of water leaving the sample (-22.4 and -38.4 %, respectively). These underpredictions are explained by the fact that for these cases Arrhenius type model overpredicts the amount of water that condenses inside of the sample (Fig. 5.10). Indeed, the Arrhenius type model is not capable of limiting the amount that condenses at a given point because it does not take into account the limit imposed by the liquid-vapour equilibrium. Therefore, even if the same amount of water is initially vaporised, a higher amount of water is retained by the sample

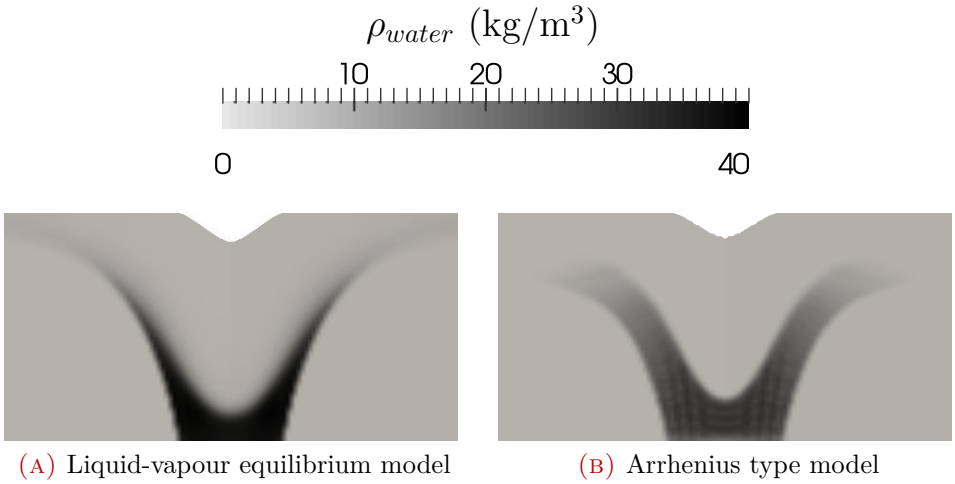

(A) Liquid-vapour equilibrium model (B) Arrhenius type model

FIGURE 5.9: Water density fields predicted by the two drying models after 5 minutes, for 0 %wb initial moisture content case

when Arrhenius type model is used to describe water behaviour.

Regarding tar production relative increase for 55 %wb initial moisture content case, its importance (+ 45.2 %) has to be mitigated by the initial low absolute value (0.29 g/min). The increase in tar production is thought to come from minor changes in the wood heating rate prediction which leads to a small absolute increase of the tar production rate prediction.

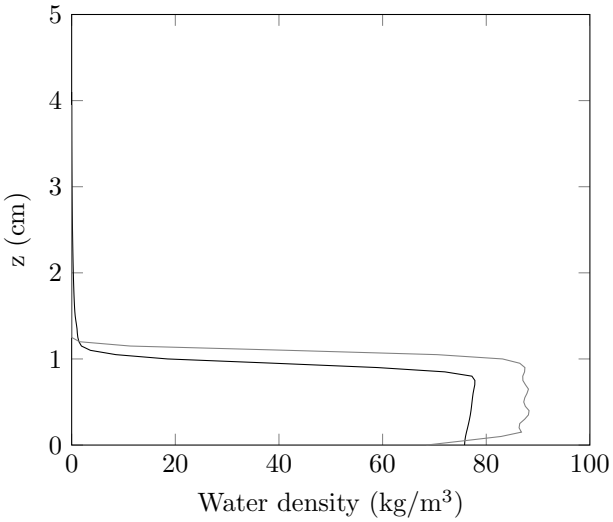

FIGURE 5.10: Water density along the sample revolution axis after 5 minutes, for the two drying models, 9 %wb bois de bout. Black line: liquid-vapour equilibrium model, gray line: Arrhenius type model

To conclude, it can be stated that Arrhenius type models can describe water vaporisation while they are not capable of properly describing water condensation inside of the sample.

5.4.2 Sensitivity to b fitting parameter

During the building of the model a fitting parameter b was added to correct the char yield predicted by the pyrolysis scheme (Fig. 4.3 and Table 4.3). In order to assess for the impact of this choice, a sensitivity analysis to this parameter was led. The b parameter was varied between -50 to +50 %, with a reference value of 2. One should note that the -50 % case corresponds to $b = 1$, which is the actual pyrolysis scheme without modification.

	b factor variation					
	-50 %	-20 %	-10 %	+10 %	+20 %	+50 %
Surface temperature	-5.0	-1.0	0.0	0.0	0.0	-1.0
Crater depth	5.0	3.0	0.0	0.0	-3.0	-3.0
Pyrolysis front thickness	-25	0	0	25	25	50
Time averaged rates:						
Wood	-6.0	-2.0	-1.0	1.0	2.0	5.0
Water	-5.0	-1.0	-1.0	1.0	1.0	3.0
Char	-49.0	-19.0	-9.0	10.0	19.0	46.0
Gas	5.0	2.0	1.0	-1.0	-2.0	-5.0
Tar	8.0	2.0	1.0	-1.0	-2.0	-6.0

TABLE 5.4: Variations (in %) for different b parameter values with respect to the reference value $b = 2$

Table 5.4 reports variations for different b parameter values in the reference case conditions, i.e. 9 %wb, bois de bout. The observed outputs can be divided into two broad categories: the ones strongly varying with b and the ones robust with respect of b.

b factor has a strong impact on char production rate and pyrolysis front thickness. An increase of b implies, as expected, an increase in char production rate. The dependency between b and the char production is linear. The pyrolysis front also thickens with an increase of the b factor. These two results are explained by the fact that the b factor directly increase the intermediate solid production and therefore the char production. Pyrolysis front thickness exhibits strong variations. Even though the trend is reasonable, absolute variation values have to be mitigated considering their front thickness calculation method. Indeed front thickness is evaluated with only one significant digit, therefore rounding error can yield important variation. e.g. +25 % for an increase from 4 to 5 mm.

b factor has a minor, yet existing, impact on crater depth, wood consumption rate and water, gas and tar production rates. An increase of b induces a reduction in the crater depth, which is thought to be a consequence of the thickening of the pyrolysis front. It also modifies the product distribution: with an increase of b, more wood in consumed, more water is released while less gas and tar are produced. The increase in wood consumption and water release can be explained by the exothermicity

of the intermediate solid to char conversion reaction. Therefore, producing more intermediate solid leads to an increase of the heat released inside of the sample. This heat, in turn, is used to power drying and pyrolysis.

b factor impact on gas and tar production rate is surprisingly low. Even if b modifies the distribution of wood pyrolysis primary products, gas and tar production rates are very robust, with variations below 8 % for ±50 % variations of b value. This result shows that the addition of b did not drastically modify the model results. Therefore, it can be stated that the b factor modifies the char production with no side effects on the simulation results.

The next step would be to determine a best fitting value for the correction factor b. Yet, given the fact that b lacks experimental validation, it was chosen not to determine it with more than one significant digit. It was therefore chosen to keep its value to 2.

5.4.3 Sensitivity to the pyrolysis model

Similarly to the impact of the choice of the drying model, the importance of the choice of the pyrolysis model has been assessed by using an alternative pyrolysis model (Fig. 5.11 and Table 5.5). The alternative model was derived for beech wood and was validated against experimental results for lower pyrolysis temperatures and heating rates than the one chosen to build the model [20]. The production of water by wood pyrolysis was taken into account using the same method as for the reference model [63]. Except for the frequency factors and activation energy values, several differences exists between the two models, the second model:

- does not feature an intermediate solid pseudo-specie that mediates char production
- describes pyrolysis as an entirely endothermic process with no exothermic lignin degradation
- does not take tar repolymerisation reactions into account

Number	Reaction	A (1/s)	Ea (kJ/mol)	Δh (kJ/kg)	Reference
1'	Wood ↦ steam	$2.0\ 10^8 \times$ a	133	-418	[20, 63]
2'	Wood ↦ gas	$1.3\ 10^8$	140	-418	[20]
3'	Wood ↦ tar	$2.0\ 10^8 \times$ (1-a)	133	-418	[20, 63]
4'	Wood ↦ char	$1.08\ 10^7$	121	-418	[20]
5'	Tar ↦ gas	$9.6\ 10^5$	144	42	[20, 55]
6'	Tar ↦ refractory tar	$5.2\ 10^5$	144	42	[20, 55]

TABLE 5.5: Alternative kinetic parameters for beech wood pyrolysis. a = 0.219 [63]

Table 5.6 reports the results of the benchmark between the two pyrolysis models. Significant discrepancies arise from this comparison. The alternative model

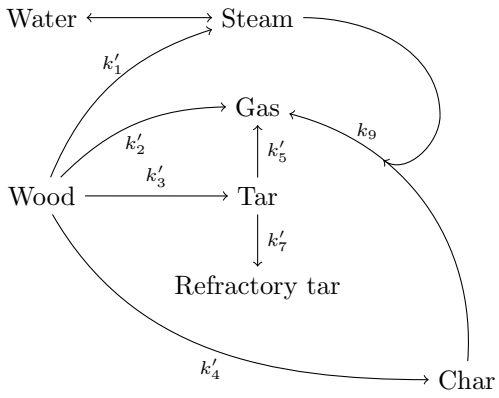

FIGURE 5.11: Alternative biomass pyrolysis scheme

substantially underpredicts wood consumption, water, char and gas production rates, as well as crater depth, while it overpredicts tar production rate.

The poor quality of the predictions is attributed to the endothermic latent heats associated with biomass degradation in the alternative model. Indeed, the alternative model does not take into account lignin exothermic degradation. Hence, the pyrolysis is endothermic, while it should be athermic. Pyrolysis acting as an heat sink, it reduces the amount of power available to dry the medium and degrade wood. Hence, wood consumption, water, char and gas production rates and crater depth are lowered.

Tar production rate overprediction is thought to be linked to a skewed repartition of the pyrolysis gaseous products highly favouring tar over gas.

	Initial moisture content		
	0 %wb	9 %wb	55 %wb
Surface temperature	0.0	-0.1	3.7
Crater depth	-17.9	-18.9	-20.0
Pyrolysis front thickness	0.0	0.0	100
Time averaged rates:			
Wood	-26.7	-23.7	-15.8
Water	-26.9	-10.3	-3.4
Char	-18.2	-14.2	-3.8
Gas	-67.0	-66.4	-61.3
Tar	13.5	22.2	66.6

TABLE 5.6: Variations (in %) between the two pyrolysis models

Conclusion

This chapter presented the numerical model predictions. First, the model construction assumptions were validated. Key dimensionless numbers were shown

not to exceed critical values. Then, numerical predictions were confronted to the experimental observations. The agreement between the numerical and experimental results is good. Based on the model predicted behaviour of biomass, further understanding of biomass degradation under high solar heat flux was derived.

Drying, pyrolysis and gasification fronts are present at the same time inside of the sample. The coexistence of these three thermochemical fronts leads to physical couplings. The major coupling being char gasification by the steam produced from drying of the sample. The model confirms that char-steam gasification is the main phenomenon behind medium ablation. The model also allows to envision the fact that tar thermal history is not limited to the residence time inside of the sample. It is very likely that they undergo thermal cracking and steam reforming after leaving the sample.

From a modelling perspective, it can be concluded from sensitivity analyses results that Arrhenius type models are not fitted for precise intra-particular water behaviour description. Indeed, they tend to mispredict the amount of water that condenses in the cold zones of the sample. These models may still be useful to describe high temperature drying whenever steam condensation is not possible.

Furthermore, the influence of the char yield correction factor was assessed. This adjustment has only a minor impact on the model behaviour, i.e. it modifies the amount of char that is produced by the sample with no side-effects on the other outputs predicted by the model. Sensitivity analyses have also shown that the choice of the biomass degradation scheme is key to properly model biomass behaviour under high solar heat flux. The use of a model validated for experimental conditions which are far from the simulated conditions leads to erroneous predictions.

Conclusion

Conclusion

Over the last three years, this PhD work tried to offer a better understanding of the interaction between biomass and concentrated solar energy. It started with an idea: combining these two energy sources so that they could compensate one another's weaknesses, i.e. biomass endothermic gasification and solar energy intermittence. In addition to the general behaviour of biomass in itself, the potentiality of this combination raised several questions. Biomass high heating rates could indeed lead to:

- fast sample drying, inducing to high internal pressure and potential mechanical failure
- very little char production and therefore rapid ablation of the medium

High achieved temperatures could enable:

- tar thermal cracking and steam reforming, while produced char could undergo steam gasification
- char thermal annealing
- carbon sublimation

It was chosen to resort on a classical approach to tackle these questions. First, literature on biomass and concentrated solar energy was reviewed. As a first step, an experimental device allowing to expose the biomass to concentrated radiative power was built. Then, this device was calibrated and operated and experimental results were analysed. As a second step, a numerical model describing biomass degradation under high solar heat flux was developed. This model was validated against the experimental results before being used to derive a better understanding of biomass behaviour under high solar heat flux.

The review of existing literature showed a lack of previous work on the specific subject of biomass degradation under high solar heat flux at the sample scale. It nevertheless emphasizes the three steps of biomass degradation: drying, pyrolysis

and gasification. These three main steps are complex in essence and influencing one another. Each of them has been widely studied. Yet, few studies focuses on two at the same time, while none encompassed the three of them in their scopes. This review of literature has allowed for a better understanding of these individual steps and the potential couplings between them. It has also been the opportunity to highlight the different modelling strategies developed to describe these phenomena. Finally, on a very practical level, this review of literature has oriented toward to use beech wood (*Fagus sylvatica*) as model biomass, because it is commonly used, which has two considerable advantages: allowing for comparison with other studies and increasing the availability of thermo-physical properties mandatory for numerical modelling.

A new experimental device allowing to expose thermally thick beech wood samples to radiative heat flux higher than 1000 kW/m^2 was built from scratch. Samples were designed in such a way that they would allow to explore the impact of fiber orientation and initial moisture content on beech wood behaviour under high solar heat flux. Samples representing two extreme wood fiber orientations were designed: bois de bout and bois de fil configurations. Samples with three different initial moisture contents were produced: 0 %wb corresponding to oven dried samples, 9 %wb accounting for samples stabilized under ambient conditions and 55 %wb emulating wood after cutting. Finally, special care was taken in calibrating this device, leading to the development of a new method of calibration for solar concentrating systems.

Using this experimental device, an original behaviour has been highlighted. Under high radiative heat flux, sample geometry evolves dramatically over a run. A crater which mirrors incident heat flux distribution is formed. Two mechanisms of crater formation have been proposed: one involving sample shrinkage and mechanical failure for low initial moisture content sample, the other relying on char steam gasification for high initial moisture content samples. Furthermore, produced chars do not undergo thermal annealing and exhibit high oxygen and hydrogen contents. Finally, achieved temperatures were high enough to promote tar thermal cracking, but not sufficient to achieve carbon sublimation.

Regarding the effect of wood fiber orientation relative to the incident heat flux, the produced results show that varying the sample orientation between the two extrema has only a minor effect on the sample behaviour. On the contrary, sample initial moisture content was shown to be of considerable importance. It was highlighted that samples containing high initial moisture content undergo char gasification. They produce 2.6 times more gas - per unit of converted dry wood - than low initial moisture content samples. Furthermore, this gas is richer in H_2. Nevertheless, the input power retained in the products of high initial moisture content samples is quite low, around 59 %. The tar yield is close to zero. It has also been shown that samples containing no water produce much more tar than moist samples. For these samples solar pyro-gasification exhibits a very good energy conversion efficiency: the recoverable products contain 90 % of the inputs (solar + wood) power. Furthermore, the power recovered in the outputs exceeds the wood input power alone, in every

configuration. It means that some of the incident radiative power has been converted into chemical form. The fraction of the incident radiative power captured can be as high as 72 % for 0 %wb, bois de bout samples.

In order to derive further insights on biomass behaviour under high solar heat flux, a numerical model describing samples under high heat flux exposure was developed. This model is based on three main conservation equations: mass, momentum and heat balances. These equations are coupled with liquid-vapour equilibrium drying model and pseudo-species biomass degradation model. Assumptions made to write these equations are defended using dimensionless numbers. Because of biomass solar gasification specific nature, i.e. medium gasification and radiation penetration, it was mandatory to develop and implement special strategies to describe medium shape evolution and incident heat flux penetration into the crater geometry.

As a validation step, the model construction assumptions were validated and the numerical predictions were confronted to the experimental observations. The agreement between the numerical and experimental results is good. Based on the model predicted behaviour, further understanding of biomass behaviour under high solar heat flux was derived. The model confirms that the gasification of char by the steam produced during drying of the sample is the main phenomenon behind medium ablation. It also allows to envision the fact that tar thermal history is not limited to the residence time inside of the sample. It is very likely that they undergo thermal cracking and steam reforming after leaving the sample. In addition, sensitivity analyses revealed that Arrhenius type models are not fitted for precise intra-particular water behaviour description and that the choice of the pyrolysis scheme is key to properly model biomass behaviour under high solar heat flux.

In this attempt to better understand beech wood behaviour under high solar heat flux, it was shown that:

- even for high initial moisture content samples, water vaporisation did not suffice to lead to sample mechanical failure
- the achieved heating rates were not high enough for the pyrolysis to yield almost no char
- tar thermal cracking and steam reforming, as well as char gasification play a major role during biomass exposition to high solar heat flux
- an exposure time of several minutes is too short for char to undergo thermal annealing even under high radiative heat flux
- reached temperatures were not high enough to enable carbon sublimation

As a general conclusion, based on the results of this work, it can be stated that the solar pyro-gasification of moist biomass is interesting for enhanced direct H_2 production with reduced tar yield, while solar pyro-gasification of dry biomass is advantageous in the perspective of solar to fuel energy conversion. In any of these

configurations, solar pyro-gasification process allows to capture solar energy in chemical form.

Appendices

APPENDIX A

Tar analysis

Tar collected in the cotton trap were analysed at CIRAD laboratory. They were first desorbed in acetone then analysed using gas chromatography coupled with mass spectrometry. Cotton was analysed to provide blank test results (Fig. A.1). 0 and 9 %wb initial moisture content samples tar were analysed twice in order to asses for run to tun repeatability (Fig. A.2 to A.5).

cirad

RAPPORT D'ANALYSE GC-MS

Nom de l'échantillon :	**Blanc**
Date de l'expérience :	24 février 2015
Date de l'analyse :	24 février 2015
Date de traitement :	15 juillet 2015
Colonne :	DB1701 - Cpsil19CB 14% cyanopropylphényl et 86% dimethylpolysiloxanne
Chromatographe :	GC Agilent 6890
Détecteur :	Spectromètre de Masse Agilent 5975

CAS	Alcools	[] mg/L
67-56-1	Methanol	<LQ (200)
	Total Alcools	**0.00**

CAS	Aldehydes et cétones	[] mg/L
50-00-0	Formaldehyde	68.71
75-07-0	Acetaldehyde	40.67
23147-58-2	Glycolaldehyde	<LQ (50)
116-09-6	2-Propanone,1-hydroxy-	<LQ (50)
930-30-3	2-cyclopenten-1-one	<LQ (1)
2758-18-1	2-cyclopenten-1-one-3-methyl	<LQ (1)
5077-67-8	2-Butanone,1-hydroxy-	<LQ (50)
765-70-8	3-methyl-1,2-cyclopentanedione	<LQ (1)
10493-98-8	2-hydroxy-2-cyclopenten-1-one	<LQ (1)
592-20-1	1-acetyloxy-2-propanone	<LQ (1)
	Total Aldehydes et cétones	**109.38**

CAS	Acides	[] mg/L
64-18-6	Formic_acid	<LQ (100)
64-19-7	Acetic_acid	<LQ (50)
79-09-4	Propionic_acid	<LQ (50)
	Total acides	**0.00**

CAS	Furanes	[] mg/L
98-01-1	Furfural	<LQ (1)
98-00-0	2-furanmethanol	<LQ (1)
271-89-6	Benzofuran	<LQ (1)
620-02-0	2-furancarboxaldehyde,5-methyl	<LQ (1)
625-86-5	2,5-dimethylfuran	<LQ (1)
67-47-0	5-hydroxymethylfurfural	<LQ (10)
	Total furanes	**0.00**

CAS	Aromatiques azotés	[] mg/L
110-86-1	Pyridine	<LQ (4)
109-06-8	Pyridine-2-methyl	<LQ (1)
91-22-5	Quinoline	<LQ (1)
119-65-3	Isoquinoline	<LQ (1)
	Total aromatiques azotés	**0.00**

CAS	Aromatiques	[] mg/L
71-43-2	Benzene	<LQ (2)
108-88-3	Toluene	<LQ (1)
100-41-4	Ethylbenzene	<LQ (2)
108-38-3 et 106-42-3	(m+p)-xylene	<LQ (1)
95-47-6	O-xylene	<LQ (1)
100-42-5	Styrene	<LQ (1)
95-13-6	Indene	<LQ (1)
2177-47-1	2-methylindene	<LQ (1)
536-74-3	Phenylethyne	<LQ (1)
	Total aromatiques	**0.00**

CAS	Sucres	[] mg/L

CAS	Phenols	[] mg/L
108-95-2	Phenol	<LQ (1)
95-48-7	Phenol-2-methyl	<LQ (1)
106-44-5 et 108-39-4	Phenol-3-methyl+Phenol-4-methyl	<LQ (2)
95-65-8	3,4-dimethylphenol	<LQ (1)
105-67-9	2,4-dimethylphenol	<LQ (1)
90-15-3	1-naphthalenol	<LQ (1)
135-19-3	2-naphthalenol	<LQ (1)
123-31-9	Hydroquinone	<LQ (1)
	Total phénols	**0.00**

CAS	Guaiacols	[] mg/L
90-05-1	Phenol-2-methoxy	<LQ (1)
93-51-6	Phenol-2-methoxy-4-methyl	<LQ (1)
91-10-1	2,6-dimethoxyphenol	<LQ (1)
2785-89-9	Phenol-4-ethyl-2-methoxy	<LQ (1)
97-53-0	Eugenol	<LQ (1)
97-54-1	Isoeugenol	<LQ (1)
7786-61-0	2-methoxy-4-vinylphenol	<LQ (1)
4812-20-8	2-isopropoxyphenol	<LQ (1)
	Total Guaiacols	**0.00**

CAS	HAPs	[] mg/L
91-20-3	Naphthalene	<LQ (1)
90-12-0	Naphthalene-1-methyl	<LQ (1)
91-57-6	Naphthalene-2-methyl	<LQ (1)
208-96-8	Acenaphthylene	<LQ (1)
83-32-9	Acenaphthene	<LQ (1)
86-73-7	Fluorene	<LQ (1)
85-01-8	Phenanthrene	<LQ (1)
120-12-7	Anthracene	<LQ (1)
206-44-0	Fluoranthene	<LQ (1)
129-00-0	Pyrene	<LQ (1)
56-55-3	Benzo(a)anthracene	<LQ (1)
218-01-9	Chrysene	<LQ (1)
205-99-2	Benzo(b)fluoranthene	<LQ (1)
207-08-9	Benzo(k)fluoranthene	<LQ (1)
50-32-8	Benzo(a)pyrene	<LQ (1)
191-24-2	Benzo(ghi)perylene	<LQ (1)
53-70-3	Dibenzo(ah)anthracene	<LQ (1)
193-39-5	Indeno(123cd)pyrene	<LQ (1)
	Total HAPs	**0.00**

CAS	Terpenes	[] mg/L
7785-70-8	1-R-a-pinene	<LQ (1)
	Total Sucres	**0.00**

	[] mg/L
Total général	**109.38**

FIGURE A.1: Virgin cotton analysis

cirad

RAPPORT D'ANALYSE GC-MS

Nom de l'échantillon :	**Run 68**
Date de l'expérience :	29/06/2015
Date de l'analyse :	29 juin 2015
Date de traitement :	15 juillet 2015
Colonne :	DB1701 - Cpsil19CB 14% cyanopropylphényl et 86% dimethylpolysiloxanne
Chromatographe :	GC Agilent 6890
Détecteur :	Spectromètre de Masse Agilent 5975

CAS	Alcools	[] mg/L
67-56-1	Methanol	<LQ (200)
	Total Alcools	**0.00**

CAS	Aldehydes et cétones	[] mg/L
50-00-0	Formaldehyde	<LQ (50)
75-07-0	Acetaldehyde	30.34
23147-58-2	Glycolaldehyde	<LQ (200)
116-09-6	2-Propanone,1-hydroxy-	<LQ (50)
930-30-3	2-cyclopenten-1-one	6.47
2758-18-1	2-cyclopenten-1-one-3-methyl	3.44
5077-67-8	2-Butanone,1-hydroxy-	<LQ (50)
765-70-8	3-methyl-1,2-cyclopentanedione	9.14
10493-98-8	2-hydroxy-2-cyclopenten-1-one	<LQ (4)
592-20-1	1-acetyloxy-2-propanone	<LQ (1)
	Total Aldehydes et cétones	**49.39**

CAS	Acides	[] mg/L
64-18-6	Formic_acid	<LQ (100)
64-19-7	Acetic_acid	198.54
79-09-4	Propionic_acid	<LQ (50)
	Total acides	**198.54**

CAS	Furanes	[] mg/L
98-01-1	Furfural	5.76
98-00-0	2-furanmethanol	<LQ (1)
271-89-6	Benzofuran	<LQ (1)
620-02-0	2-furancarboxaldehyde,5-methyl	1.38
625-86-5	2,5-dimethylfuran	<LQ (1)
67-47-0	5-hydroxymethylfurfural	<LQ (10)
	Total furanes	**7.14**

CAS	Aromatiques azotés	[] mg/L
110-86-1	Pyridine	<LQ (4)
109-06-8	Pyridine-2-methyl	<LQ (1)
91-22-5	Quinoline	<LQ (1)
119-65-3	Isoquinoline	<LQ (1)
	Total aromatiques azotés	**0.00**

CAS	Aromatiques	[] mg/L
71-43-2	Benzene	<LQ (2)
108-88-3	Toluene	<LQ (1)
100-41-4	Ethylbenzene	<LQ (2)
108-38-3 et 106-42-3	(m+p)-xylene	<LQ (1)
95-47-6	O-xylene	<LQ (1)
100-42-5	Styrene	<LQ (1)
95-13-6	Indene	<LQ (1)
2177-47-1	2-methylindene	<LQ (1)
536-74-3	Phenylethyne	<LQ (1)
	Total aromatiques	**0.00**

CAS	Sucres	[] mg/L

CAS	Phenols	[] mg/L
108-95-2	Phenol	31.39
95-48-7	Phenol-2-methyl	6.05
106-44-5 et 108-39-4	Phenol-3-methyl+Phenol-4-methyl	10.98
95-65-8	3,4-dimethylphenol	<LQ (1)
105-67-9	2,4-dimethylphenol	2.42
90-15-3	1-naphthalenol	<LQ (1)
135-19-3	2-naphthalenol	<LQ (1)
123-31-9	Hydroquinone	2.80
	Total phénols	**53.64**

CAS	Guaiacols	[] mg/L
90-05-1	Phenol-2-methoxy	1.83
93-51-6	Phenol-2-methoxy-4-methyl	1.44
91-10-1	2,6-dimethoxyphenol	3.97
2785-89-9	Phenol-4-ethyl-2-methoxy	0.74
97-53-0	Eugenol	<LQ (1)
97-54-1	Isoeugenol	0.62
7786-61-0	2-methoxy-4-vinylphenol	2.29
4812-20-8	2-isopropoxyphenol	<LQ (1)
	Total Guaiacols	**10.89**

CAS	HAPs	[] mg/L
91-20-3	Naphthalene	1.27
90-12-0	Naphthalene-1-methyl	<LQ (1)
91-57-6	Naphthalene-2-methyl	<LQ (1)
208-96-8	Acenaphthylene	2.02
83-32-9	Acenaphthene	0.84
86-73-7	Fluorene	<LQ (1)
85-01-8	Phenanthrene	4.05
120-12-7	Anthracene	1.04
206-44-0	Fluoranthene	3.11
129-00-0	Pyrene	3.56
56-55-3	Benzo(a)anthracene	<LQ (1)
218-01-9	Chrysene	<LQ (1)
205-99-2	Benzo(b)fluoranthene	<LQ (1)
207-08-9	Benzo(k)fluoranthene	<LQ (1)
50-32-8	Benzo(a)pyrene	<LQ (1)
191-24-2	Benzo(ghi)perylene	<LQ (1)
53-70-3	Dibenzo(ah)anthracene	<LQ (1)
193-39-5	Indeno(123cd)pyrene	<LQ (1)
	Total HAPs	**15.89**

CAS	Terpenes	[] mg/L
7785-70-8	1-R-a-pinene	<LQ (1)
	Total Sucres	**0.00**

	[] mg/L
Total général	**352.81**

FIGURE A.2: 0 %wb initial moisture content sample tar analysis, run 1

cirad

RAPPORT D'ANALYSE GC-MS

Nom de l'échantillon :	**Run 69**
Date de l'expérience :	29/06/2015
Date de l'analyse :	29 juin 2015
Date de traitement :	15 juillet 2015
Colonne :	DB1701 - Cpsil19CB 14% cyanopropylphényl et 86% dimethylpolysiloxanne
Chromatographe :	GC Agilent 6890
Détecteur :	Spectromètre de Masse Agilent 5975

CAS	Alcools	[] mg/L
67-56-1	Methanol	<LQ (200)
	Total Alcools	**0.00**

CAS	Aldehydes et cétones	[] mg/L
50-00-0	Formaldehyde	<LQ (50)
75-07-0	Acetaldehyde	<LQ (50)
23147-58-2	Glycolaldehyde	<LQ (200)
116-09-6	2-Propanone,1-hydroxy-	<LQ (50)
930-30-3	2-cyclopenten-1-one	6.46
2758-18-1	2-cyclopenten-1-one-3-methyl	2.22
5077-67-8	2-Butanone,1-hydroxy-	<LQ (50)
765-70-8	3-methyl-1,2-cyclopentanedione	<LQ (1)
10493-98-8	2-hydroxy-2-cyclopenten-1-one	<LQ (4)
592-20-1	1-acetyloxy-2-propanone	<LQ (1)
	Total Aldehydes et cétones	**8.68**

CAS	Acides	[] mg/L
64-18-6	Formic_acid	<LQ (100)
64-19-7	Acetic_acid	195.87
79-09-4	Propionic_acid	<LQ (50)
	Total acides	**195.87**

CAS	Furanes	[] mg/L
98-01-1	Furfural	5.74
98-00-0	2-furanmethanol	<LQ (1)
271-89-6	Benzofuran	<LQ (1)
620-02-0	2-furancarboxaldehyde,5-methyl	1.12
625-86-5	2,5-dimethylfuran	<LQ (1)
67-47-0	5-hydroxymethylfurfural	<LQ (10)
	Total furanes	**6.87**

CAS	Aromatiques azotés	[] mg/L
110-86-1	Pyridine	<LQ (4)
109-06-8	Pyridine-2-methyl	<LQ (1)
91-22-5	Quinoline	<LQ (1)
119-65-3	Isoquinoline	<LQ (1)
	Total aromatiques azotés	**0.00**

CAS	Aromatiques	[] mg/L
71-43-2	Benzene	<LQ (2)
108-88-3	Toluene	<LQ (1)
100-41-4	Ethylbenzene	<LQ (2)
108-38-3 et 106-42-3	(m+p)-xylene	<LQ (1)
95-47-6	O-xylene	<LQ (1)
100-42-5	Styrene	<LQ (1)
95-13-6	Indene	<LQ (1)
2177-47-1	2-methylindene	<LQ (1)
536-74-3	Phenylethyne	<LQ (1)
	Total aromatiques	**0.00**

CAS	Sucres	[] mg/L

CAS	Phenols	[] mg/L
108-95-2	Phenol	27.51
95-48-7	Phenol-2-methyl	5.12
106-44-5 et 108-39-4	Phenol-3-methyl+Phenol-4-methyl	8.71
95-65-8	3,4-dimethylphenol	<LQ (1)
105-67-9	2,4-dimethylphenol	1.78
90-15-3	1-naphthalenol	<LQ (1)
135-19-3	2-naphthalenol	<LQ (1)
123-31-9	Hydroquinone	3.27
	Total phénols	**46.40**

CAS	Guaiacols	[] mg/L
90-05-1	Phenol-2-methoxy	<LQ (1)
93-51-6	Phenol-2-methoxy-4-methyl	0.88
91-10-1	2,6-dimethoxyphenol	4.16
2785-89-9	Phenol-4-ethyl-2-methoxy	<LQ (1)
97-53-0	Eugenol	<LQ (1)
97-54-1	Isoeugenol	0.37
7786-61-0	2-methoxy-4-vinylphenol	<LQ (1)
4812-20-8	2-isopropoxyphenol	<LQ (1)
	Total Guaiacols	**5.41**

CAS	HAPs	[] mg/L
91-20-3	Naphthalene	1.21
90-12-0	Naphthalene-1-methyl	<LQ (1)
91-57-6	Naphthalene-2-methyl	<LQ (1)
208-96-8	Acenaphthylene	1.10
83-32-9	Acenaphthene	<LQ (1)
86-73-7	Fluorene	<LQ (1)
85-01-8	Phenanthrene	4.65
120-12-7	Anthracene	1.09
206-44-0	Fluoranthene	3.92
129-00-0	Pyrene	4.55
56-55-3	Benzo(a)anthracene	<LQ (1)
218-01-9	Chrysene	<LQ (1)
205-99-2	Benzo(b)fluoranthene	<LQ (1)
207-08-9	Benzo(k)fluoranthene	<LQ (1)
50-32-8	Benzo(a)pyrene	<LQ (1)
191-24-2	Benzo(ghi)perylene	<LQ (1)
53-70-3	Dibenzo(ah)anthracene	<LQ (1)
193-39-5	Indeno(123cd)pyrene	<LQ (1)
	Total HAPs	**16.51**

CAS	Terpenes	[] mg/L
7785-70-8	1-R-a-pinene	<LQ (1)
	Total Sucres	**0.00**

	[] mg/L
Total général	**295.93**

FIGURE A.3: 0 %wb initial moisture content sample tar analysis, run 2

cirad

RAPPORT D'ANALYSE GC-MS

Nom de l'échantillon :	**Run 42**
Date de l'expérience :	25 février 2015
Date de l'analyse :	25 février 2015
Date de traitement :	15 juillet 2015
Colonne :	DB1701 - Cpsil19CB 14% cyanopropylphényl et 86% dimethylpolysiloxanne
Chromatographe :	GC Agilent 6890
Détecteur :	Spectromètre de Masse Agilent 5975

CAS	Alcools	[] mg/L
67-56-1	Methanol	<LQ (200)
	Total Alcools	**0.00**

CAS	Aldehydes et cétones	[] mg/L
50-00-0	Formaldehyde	<LQ (50)
75-07-0	Acetaldehyde	<LQ (50)
23147-58-2	Glycolaldehyde	<LQ (50)
116-09-6	2-Propanone,1-hydroxy-	<LQ (50)
930-30-3	2-cyclopenten-1-one	<LQ (1)
2758-18-1	2-cyclopenten-1-one-3-methyl	0.96
5077-67-8	2-Butanone,1-hydroxy-	<LQ (50)
765-70-8	3-methyl-1,2-cyclopentanedione	5.54
10493-98-8	2-hydroxy-2-cyclopenten-1-one	<LQ (1)
592-20-1	1-acetyloxy-2-propanone	<LQ (1)
	Total Aldehydes et cétones	**6.50**

CAS	Acides	[] mg/L
64-18-6	Formic_acid	<LQ (100)
64-19-7	Acetic_acid	142.37
79-09-4	Propionic_acid	<LQ (50)
	Total acides	**142.37**

CAS	Furanes	[] mg/L
98-01-1	Furfural	<LQ (1)
98-00-0	2-furanmethanol	<LQ (1)
271-89-6	Benzofuran	<LQ (1)
620-02-0	2-furancarboxaldehyde,5-methyl	<LQ (1)
625-86-5	2,5-dimethylfuran	<LQ (1)
67-47-0	5-hydroxymethylfurfural	<LQ (10)
	Total furanes	**0.00**

CAS	Aromatiques azotés	[] mg/L
110-86-1	Pyridine	<LQ (4)
109-06-8	Pyridine-2-methyl	<LQ (1)
91-22-5	Quinoline	<LQ (1)
119-65-3	Isoquinoline	<LQ (1)
	Total aromatiques azotés	**0.00**

CAS	Aromatiques	[] mg/L
71-43-2	Benzene	<LQ (2)
108-88-3	Toluene	<LQ (1)
100-41-4	Ethylbenzene	<LQ (2)
108-38-3 et 106-42-3	(m+p)-xylene	<LQ (1)
95-47-6	O-xylene	<LQ (1)
100-42-5	Styrene	<LQ (1)
95-13-6	Indene	<LQ (1)
2177-47-1	2-methylindene	<LQ (1)
536-74-3	Phenylethyne	<LQ (1)
	Total aromatiques	**0.00**

CAS	Sucres	[] mg/L

CAS	Phenols	[] mg/L
108-95-2	Phenol	9.40
95-48-7	Phenol-2-methyl	<LQ (1)
106-44-5 et 108-39-4	Phenol-3-methyl+Phenol-4-methyl	4.52
95-65-8	3,4-dimethylphenol	<LQ (1)
105-67-9	2,4-dimethylphenol	0.71
90-15-3	1-naphthalenol	0.86
135-19-3	2-naphthalenol	0.77
123-31-9	Hydroquinone	2.21
	Total phénols	**18.48**

CAS	Guaiacols	[] mg/L
90-05-1	Phenol-2-methoxy	<LQ (1)
93-51-6	Phenol-2-methoxy-4-methyl	<LQ (1)
91-10-1	2,6-dimethoxyphenol	3.56
2785-89-9	Phenol-4-ethyl-2-methoxy	<LQ (1)
97-53-0	Eugenol	<LQ (1)
97-54-1	Isoeugenol	1.96
7786-61-0	2-methoxy-4-vinylphenol	<LQ (1)
4812-20-8	2-isopropoxyphenol	<LQ (1)
	Total Guaiacols	**5.52**

CAS	HAPs	[] mg/L
91-20-3	Naphthalene	<LQ (1)
90-12-0	Naphthalene-1-methyl	<LQ (1)
91-57-6	Naphthalene-2-methyl	<LQ (1)
208-96-8	Acenaphthylene	6.08
83-32-9	Acenaphthene	1.15
86-73-7	Fluorene	3.26
85-01-8	Phenanthrene	12.83
120-12-7	Anthracene	3.16
206-44-0	Fluoranthene	5.93
129-00-0	Pyrene	6.24
56-55-3	Benzo(a)anthracene	<LQ (1)
218-01-9	Chrysene	<LQ (1)
205-99-2	Benzo(b)fluoranthene	<LQ (1)
207-08-9	Benzo(k)fluoranthene	<LQ (1)
50-32-8	Benzo(a)pyrene	<LQ (1)
191-24-2	Benzo(ghi)perylene	<LQ (1)
53-70-3	Dibenzo(ah)anthracene	<LQ (1)
193-39-5	Indeno(123cd)pyrene	<LQ (1)
	Total HAPs	**38.64**

CAS	Terpenes	[] mg/L
7785-70-8	1-R-a-pinene	<LQ (1)
	Total Sucres	**0.00**

	[] mg/L
Total général	**211.50**

FIGURE A.4: 9 %wb initial moisture content sample tar analysis, run 1

cirad

RAPPORT D'ANALYSE GC-MS

Nom de l'échantillon :	**Run 44**
Date de l'expérience :	25 février 2015
Date de l'analyse :	25 février 2015
Date de traitement :	15 juillet 2015
Colonne :	DB1701 - Cpsil19CB 14% cyanopropylphényl et 86% dimethylpolysiloxanne
Chromatographe :	GC Agilent 6890
Détecteur :	Spectromètre de Masse Agilent 5975

CAS	Alcools	[] mg/L
67-56-1	Methanol	<LQ (200)
	Total Alcools	**0.00**

CAS	Aldehydes et cétones	[] mg/L
50-00-0	Formaldehyde	<LQ (50)
75-07-0	Acetaldehyde	<LQ (50)
23147-58-2	Glycolaldehyde	149.37
116-09-6	2-Propanone,1-hydroxy-	48.01
930-30-3	2-cyclopenten-1-one	1.37
2758-18-1	2-cyclopenten-1-one-3-methyl	1.78
5077-67-8	2-Butanone,1-hydroxy-	<LQ (50)
765-70-8	3-methyl-1,2-cyclopentanedione	9.92
10493-98-8	2-hydroxy-2-cyclopenten-1-one	<LQ (1)
592-20-1	1-acetyloxy-2-propanone	<LQ (1)
	Total Aldehydes et cétones	**210.45**

CAS	Acides	[] mg/L
64-18-6	Formic_acid	<LQ (100)
64-19-7	Acetic_acid	244.03
79-09-4	Propionic_acid	<LQ (50)
	Total acides	**244.03**

CAS	Furanes	[] mg/L
98-01-1	Furfural	<LQ (1)
98-00-0	2-furanmethanol	<LQ (1)
271-89-6	Benzofuran	<LQ (1)
620-02-0	2-furancarboxaldehyde,5-methyl	<LQ (1)
625-86-5	2,5-dimethylfuran	<LQ (1)
67-47-0	5-hydroxymethylfurfural	<LQ (10)
	Total furanes	**0.00**

CAS	Aromatiques azotés	[] mg/L
110-86-1	Pyridine	<LQ (4)
109-06-8	Pyridine-2-methyl	<LQ (1)
91-22-5	Quinoline	<LQ (1)
119-65-3	Isoquinoline	<LQ (1)
	Total aromatiques azotés	**0.00**

CAS	Aromatiques	[] mg/L
71-43-2	Benzene	<LQ (2)
108-88-3	Toluene	1.20
100-41-4	Ethylbenzene	<LQ (2)
108-38-3 et 106-42-3	(m+p)-xylene	<LQ (1)
95-47-6	O-xylene	<LQ (1)
100-42-5	Styrene	<LQ (1)
95-13-6	Indene	<LQ (1)
2177-47-1	2-methylindene	<LQ (1)
536-74-3	Phenylethyne	<LQ (1)
	Total aromatiques	**1.20**

CAS	Sucres	[] mg/L

CAS	Phenols	[] mg/L
108-95-2	Phenol	13.05
95-48-7	Phenol-2-methyl	0.77
106-44-5 et 108-39-4	Phenol-3-methyl+Phenol-4-methyl	6.25
95-65-8	3,4-dimethylphenol	<LQ (1)
105-67-9	2,4-dimethylphenol	1.02
90-15-3	1-naphthalenol	1.07
135-19-3	2-naphthalenol	1.07
123-31-9	Hydroquinone	3.64
	Total phénols	**26.87**

CAS	Guaiacols	[] mg/L
90-05-1	Phenol-2-methoxy	<LQ (1)
93-51-6	Phenol-2-methoxy-4-methyl	<LQ (1)
91-10-1	2,6-dimethoxyphenol	5.91
2785-89-9	Phenol-4-ethyl-2-methoxy	<LQ (1)
97-53-0	Eugenol	0.33
97-54-1	Isoeugenol	2.93
7786-61-0	2-methoxy-4-vinylphenol	<LQ (1)
4812-20-8	2-isopropoxyphenol	<LQ (1)
	Total Guaiacols	**9.17**

CAS	HAPs	[] mg/L
91-20-3	Naphthalene	<LQ (1)
90-12-0	Naphthalene-1-methyl	<LQ (1)
91-57-6	Naphthalene-2-methyl	<LQ (1)
208-96-8	Acenaphthylene	10.33
83-32-9	Acenaphthene	1.78
86-73-7	Fluorene	5.50
85-01-8	Phenanthrene	20.66
120-12-7	Anthracene	4.64
206-44-0	Fluoranthene	8.80
129-00-0	Pyrene	9.34
56-55-3	Benzo(a)anthracene	1.10
218-01-9	Chrysene	0.97
205-99-2	Benzo(b)fluoranthene	<LQ (1)
207-08-9	Benzo(k)fluoranthene	<LQ (1)
50-32-8	Benzo(a)pyrene	<LQ (1)
191-24-2	Benzo(ghi)perylene	<LQ (1)
53-70-3	Dibenzo(ah)anthracene	<LQ (1)
193-39-5	Indeno(123cd)pyrene	<LQ (1)
	Total HAPs	**63.12**

CAS	Terpenes	[] mg/L
7785-70-8	1-R-a-pinene	<LQ (1)
	Total Sucres	**0.00**

	[] mg/L
Total général	**554.83**

FIGURE A.5: 9 %wb initial moisture content sample tar analysis, run 2

APPENDIX B

Wood, char and ash physical properties

In order to chose the physical properties correlations that are used in the model, a survey of literature was conducted. Tables B.1 and B.2 sum up wood thermal and hydrodynamic physical properties, while Tables B.3 and B.4 deal with those of char.

Ashes are known to be able to agglomerate and form a radiative heat shield at reactor scale because of their low absorptivity and thermal conductivity. Values of their physical properties were encountered during the survey, it was though to be interesting to report them, even though ashes were not taken into account in the developed model.

Ash thermal conductivity dramatically depends on ash geometry. In the porous configuration, it has been reported to be 0.31 W/m/K with a porosity of 0.72. These measurements were done at 650 °C [170]. In bulk configuration, thermal conductivity was estimated to be around 3 W/m/K [170]. A short review of ash specific heat capacity and thermal conductivity is proposed in [81].

Ash emissivity varies dramatically with temperature, from 0.7 at 327 °C to 0.3 at 1527 °C. It also exhibits a strong spectral variability as demonstrated by the reported dependency with heat source temperature [83]. Finally, when taken into account, ash emissivity is taken a flat value of 0.4 [82].

c_p (kJ/kg/K)	λ (W/m/K)		D_{th} (10^{-6} m^2/s)		ρ (kg/m^3)	α (absorptivity)	Wood type (species number)	Note and reference
	Long.	Radial/Ortho.	Long.	Radial/Ortho.				
1.2 - 1.8	0.094 - 0.21	-	0.16	-	310 - 780	-	Both (68)	f(T) [32]
1.0 - 1.7	-	0.05 - 0.20	0.15 - 0.23		360 - 504	-	Softwood (5)	f(T, ρ_{wood}) [155]
1.0 - 1.7	-	0.05 - 0.20	0.15 - 0.23		286 - 788	-	Hardwood (8)	f(T, ρ_{wood}) [155]
-	-	-	-	-	-	0.50 - 0.86	? (2)	f(T) [157]
2.3	0.1046		-		-	-	-	[171]
0.670 - 2.50	-	0.0986 - 0.2050	-		360 -482	0.8	Softwood (3)	f(T) [172]
1.51 - 1.60	0.156 - 0.278	0.074 - 0.176	1.95 - 3.57	0.92 - 2.32	510 - 690	-	Both (9)	[173]
-	-	-	-	-	-	0.5	Model material	[174]
-	-	-	-	-	-	0.93	-	[82, 156]

Table B.1: Wood thermal properties

κ (10^{-12} m^2)		D_{mass} (10^{-9} m^2/s)		Wood type (species number)	Reference
Long.	Radial/Ortho.	Long.	Radial/Ortho.		
9.4 10^{-2} - 1.75	4.82 10^{-6} - 1.65 10^{-3}	4.0 - 14.3	1.3 10^{-1} - 4.8 10^{-1}	Dur (4)	[34]
1.0 10^{-2}	-	-	-	-	[48]
1.0 10^{-2}	-	-	-	-	[94]
4 10^{-4} - 5.55 10^{-2}	3 10^{-9} - 8.6 10^{-6}	6 10^{-2} - 1.03	1 10^{-2} - 7 10^{-2}	Dur (4)	[158]
1 10^{-5}	-	-	-	-	[171]
2.3 10^{-2} - 5.4 10^{-1}	6.9 10^{-7} - 7.3 10^{-5}	-	-	? (4)	[175]

Table B.2: Wood hydrodynamic properties

c_p (kJ/kg/K)	λ (W/m/K) Long.	Radial/Ortho.	D_{th} (10^{-6} m^2/s)	ρ (kg/m^3)	α (absorptivity)	Wood type (species number)	Note and reference
-	0.04		-	710	-	Hardwood (1)	[125]
-	0.25 - 0.47	0.15 - 0.25	-	-	-	Hardwood (1)	f(T) [143]
1.1	0.1046		-	-	-	-	[171]
0.768 - 1.506	-	0.0946	-	299	0.95	Softwood (3)	f(T) [172]
-	0.7 - 1.7		-	1200	-	Coal	[176]

TABLE B.3: Char thermal properties

κ (10^{-12} m^2) Long.	Radial/Ortho.	D_{mass} (10^{-9} m^2/s) Long.	Radial/Ortho.	Reference
10	-	-	-	[48]
1	-	-	-	[94]
10	-	-	-	[171]

TABLE B.4: Char hydrodynamic properties

APPENDIX C

Gaseous species and liquid water physical properties

Given the wide temperature range covered by the model, gaseous species physical properties values have to evolve with temperature in order to get the best description possible. The correlations used in this work have been validated against experimental results. When possible, it was chosen to rely on JANAF correlations [177] because of their wide validity range and known quality. Yet, some of the correlations are used out of their validity range. To ensure that they provide plausible values, their trends were plotted and verified.

C.1 Nitrogen

λ_{N_2} = - 6.4704 10^{-9}T^2 + 6.9270 10^{-5}T + 4.7757 10^{-3}, W/m/K, [178]

For T $\leq$ 500 K:

$c_{p_{N_2}}$ = (28.98641 + 1.853978 x - 9.647459 x^2 + 16.63537 x^3 + 0.000117 x^{-2})/M_{N_2} with $x = T/1000$, J/kg/K [177]

For 500 < T $\leq$ 1300 K:

$c_{p_{N_2}}$ = (19.50583 + 19.88705 x - 8.598535 x^2 + 1.369784 x^3 + 0.527601 x^{-2})/M_{N_2} with $x = T/1000$, J/kg/K [177]

For T > 1300 K:

$c_{p_{N_2}}$ = (35.51872 + 1.128728 x - 0.196103 x^2 + 0.014662 x^3 - 4.553760 x^{-2})/M_{N_2} with $x = T/1000$, J/kg/K [177]

$\mu_{N_2} = \frac{14.002\ T^{3/2}}{T+106.9}\ 10^{-7}$, Pa.s [179]

C.2 Steam

$\lambda_{steam} = \sqrt{x}(0.0102811 + 0.029962\ \mathrm{x} + 0.0156146\ \mathrm{x}^2 - 0.00422464\ \mathrm{x}^3) + (-0.397070 + 0.400302\ \mathrm{E} + 1.060000\ \exp(-0.171587\ (\mathrm{E} + 2.392190)^2))$ with $x = T/647.3$ and $E = \rho_{vap}/317.7$, W/m/K [177]

For T $\leq$ 1700 K:

$c_{p_{steam}} = (30.09200 + 6.832514\ \mathrm{x} + 6.793435\ \mathrm{x}^2 - 2.534480\ \mathrm{x}^3 + 0.082139\ \mathrm{x}^{-2})/M_{steam}$ with $x = T/1000$, J/kg/K [177]

For T $>$ 1700 K:

$c_{p_{steam}} = (41.96426 + 8.622053\ \mathrm{x} - 1.499780\ \mathrm{x}^2 + 0.098119\ \mathrm{x}^3 - 11.15764\ \mathrm{x}^{-2})/M_{steam}$ with $x = T/1000$, J/kg/K [177]

$\mu_{steam} = \frac{39.73\ T^{3/2}}{3315-T+0.001158\ T^2}\ 10^{-7}$, Pa.s [179]

C.3 Carbon monoxide

Carbon monoxide and nitrogen are very close at a molecular level. They have the same structure, molar mass. It has been shown that they have the same thermal conductivity [180]. Nitrogen thermal conductivity was therefore used to describe carbon monoxide thermal conductivity.

$\lambda_{CO} = -6.4704\ 10^{-9}\mathrm{T}^2 + 6.9270\ 10^{-5}\mathrm{T} + 4.7757\ 10^{-3}$, W/m/K, [178]

For T $\leq$ 1300 K:

$c_{pCO} = (25.56759 + 6.096130\ \mathrm{x} + 4.054656\ \mathrm{x}^2 - 2.671301\ \mathrm{x}^3 + 0.131021\ \mathrm{x}^{-2})/M_{CO}$ with $x = T/1000$, J/kg/K [177]

For T $>$ 1300 K:

$c_{pCO} = (35.15070 + 1.300095\ \mathrm{x} - 0.205921\ \mathrm{x}^2 + 0.013550\ \mathrm{x}^3 - 3.282780\ \mathrm{x}^{-2})/M_{CO}$ with $x = T/1000$, J/kg/K [177]

$\mu_{CO} = 2.0260^{-14}\mathrm{T}^3 - 4.7989\ 10^{-11}\mathrm{T}^2 + 6.8955\ 10^{-8}\mathrm{T} + 9.2809\ 10^{-7}$, Pa.s [181]

C.4 Benzene

$\lambda_{benzene}$ = 2.3010 10^{-8}T^2 + 8.3038 10^{-5}T - 1.7156 10^{-2}, W/m/K [182]

$c_{p_{benzene}} = \frac{R_{GP}}{M_{benzene}}$ (4 + (34.383386 + 129.858849 x^{-1} + 415.777762 x^{-2} - 1066.57015 x^{-3} + 1697.12898 x^{-4}) exp(- 8.60/x)) with $x = T/100$, J/kg/K [183]

$\mu_{benzene}$ = 2.3289 10^{-11}T^2 + 7.3938 10^{-9}T + 3.3796 10^{-6}, Pa.s [184]

C.5 Liquid water

λ_{lw} = 0.6065 (- 1.48445 + 4.12292 $\frac{T}{298.15}$ - 1.63866 $\frac{T^2}{298.15^2}$), W/m/K, [185]

$c_{p_{lw}}$ = 4183, J/kg/K

μ_{lw} = 1.0 10^{-3}, Pa.s

APPENDIX D

Radiation near surface penetration model

Considering that the incident radiation wavelength is much smaller than the wood mean pore diameter, radiation ballistically penetrates into the porous medium. It is interesting to evaluate the depth of this penetration. To do this, basic geometrical considerations are used.

D.1 Penetration into the wood

Beech wood is considered to be made of parallel channels. Their mean diameter is $d_{pore,\ wood} = 55.3\ \mu m$ [154] and their tortuosity is $\tau = 1.5$ [34]. Radiation penetration is considered in two different geometrical configurations: a channel parallel to the incident heat flux with a geometrical accident (Fig. D.1 A) and a channel tilted relative to the incident heat flux (Fig. D.1 B). These two representations are, of course, ideal views of the actual geometry. Nevertheless, they allow to assess the radiation penetration depth (L_{pen}).

D.1.1 Geometrical accident

Considering the that L is the length of the porous medium and d_{pore} is the length of the geometrical accident, it is possible to link them to the tortuosity (Eq. D.1 and D.2). The probability of the geometrical accident is uniformly distributed along the channel length, following the distribution $\mathcal{U}$[0,L], with a mean of $L/2$. Radiation penetration depth has therefore to be evaluated taking the distribution into account (Eq. D.3).

$$\tau = \frac{L + d_{pore}}{L} \tag{D.1}$$

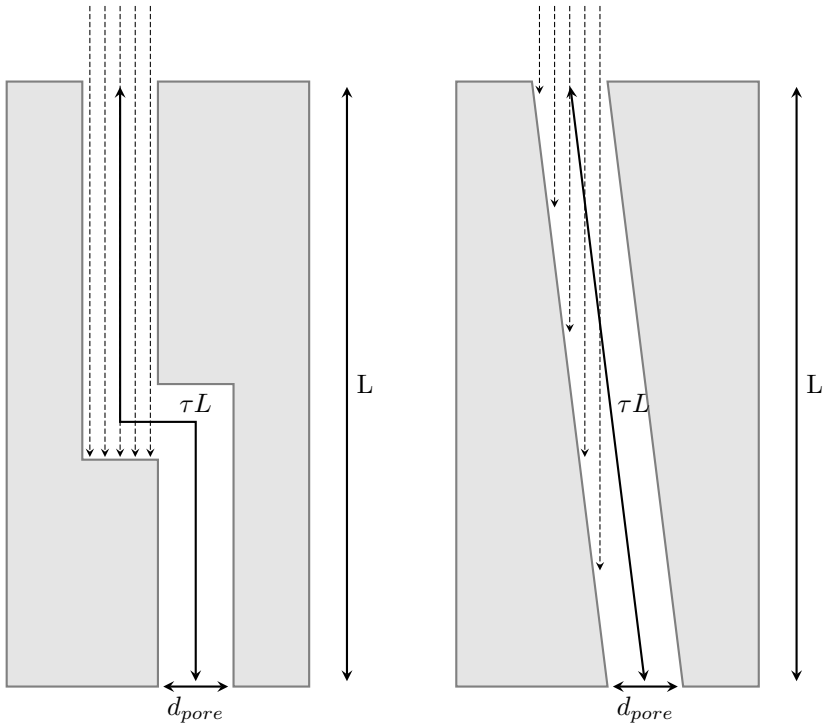

(A) Geometrical accident (B) Tilted channel

FIGURE D.1: Radiation near surface penetration geometrical configurations

$$L = \frac{d_{pore}}{\tau - 1} \tag{D.2}$$

$$< L_{pen} >= \frac{d_{pore}}{2(\tau - 1)} \tag{D.3}$$

In this configuration, the radiation penetration depth is around 55.3 μm.

D.1.2 Tilted channel

Using Pythagoras' theorem, on can express the tortuosity as a function of the medium length and pore diameter (Eq. D.4) and deduce the penetration length (Eq. D.5).

$$\tau = \frac{\sqrt{L^2 + d_{pore}^2}}{L} \tag{D.4}$$

$$L_{pen} = \frac{d_{pore}}{\sqrt{\tau^2 - 1}} \tag{D.5}$$

In this configuration, the radiation penetration depth is around 49.5 μm. This value is close to the one found in the first configuration. An order of magnitude of the radiation penetration depth can therefore be derived. Radiation penetration depth in wood is thus considered to be 53 μm.

D.2 Penetration into the char

Soon after the beginning of the transformation, the sample surface is charred. Therefore, it is important to assess the depth of the radiation penetration through the char layer. Char is considered to have the same parallel channels structure as wood, with the same tortuosity. Yet, its porosity differs which has an impact on its pore mean diameter. The char pore mean diameter is evaluated using Eq. D.6. Then, radiation penetration depth is calculated with the same method used for wood. The radiation penetration depth is about 69.6 μm in the first configuration and 62.2 μm in the second. Radiation penetration depth in char is considered to be 66 μm.

$$d_{pore,\ char} = d_{pore,\ wood}\sqrt{\frac{\zeta_{char}}{\zeta_{wood}}} \tag{D.6}$$

APPENDIX E

French extended abstract / Résumé long

Introduction

La consommation mondiale d'énergie primaire a considérablement augmenté durant les 30 dernières années, passant de 7.14 GTep (Giga tonne équivalent pétrole) en 1980 à 13.2 GTep en 2012 (Fig. 1). Cette augmentation s'est fortement appuyée sur les énergies fossiles ce qui a conduit à la libération de grandes quantités de gaz à effet de serre dans l'atmosphère [1]. Ces gaz ont induit le réchauffement global de la planète ainsi que le changement de son climat [2]. S'il n'est pas stoppé, le changement climatique conduira à une plus grande occurrence d'événements météorologiques extrêmes. Alors que, parallèlement, le réchauffement planétaire fera chuter les rendements agricoles dans les zones tropicales et tempérées, mettant ainsi en danger la sécurité alimentaire. A la lueur de ces projections, il est impératif de limiter au cours du siècle à venir le réchauffement climatique à 2 °C, par rapport au niveau préindustriel, pour en éviter les conséquences les plus lourdes.

Dans le même temps, une forte augmentation de la consommation d'énergie primaire est anticipée. Dans son scénario médian, l'*Agence Internationale de l'Energie* prévoit une croissance de 37 % de la demande en énergie primaire d'ici 2040. Sur la même période, *US Energy Information Administration* prévoit elle une augmentation de 56 % [4]. Un tel accroissement de la consommation, tiré par l'augmentation des besoins en Asie, Afrique, Moyen Orient et Amérique Latine, conduirait à un réchauffement global de 3.6 °C. L'humanité doit donc réduire sa dépendance vis à vis des énergies fossiles et avoir recours à des sources d'énergies renouvelables et neutre en gaz à effet de serre comme l'énergie éolienne, hydraulique, solaire ou la biomasse.

Parmi ces sources d'énergie, l'énergie solaire se détache par sa versatilité : elle peut aussi bien produire directement de l'électricité que de la chaleur à haute température.

De plus, l'énergie solaire à un fort potentiel croissance. Cependant, elle est par essence intermittente et son stockage reste un défit qu'il faudra relever dans les années à venir.

Le terme *biomasse* regroupe les matières premières carbonées d'origine renouvelable. La biomasse peut subir de nombreuses transformations (combustion, méthanisation, gazéification, ...) et être ainsi valorisée sous différentes formes, i.e. chaleur, biogaz, gaz de synthèse, ... Le gaz de synthèse est un mélange de dihydrogène et de monoxyde de carbone. Selon sa composition, il peut être utilisé comme carburant dans les piles à combustible, les turbines à gaz, les moteurs, les fours industriels ou pour synthétiser du carburant liquide via le procédé Fisher Tropsch [6]. Néanmoins, la gazéification de la biomasse est fortement endothermique et nécessite d'atteindre des températures d'au moins 800 °C. Habituellement, l'énergie nécessaire est fournie par la combustion d'une partie de la biomasse injectée dans le réacteur. Cette technique a deux inconvénients : le rendement par rapport à la biomasse en entrée est abaissé et le gaz de synthèse produit est dilué par l'azote provenant de l'air de combustion.

La combinaison de la biomasse et de l'énergie solaire pourrait répondre aux problèmes inhérents à chacune de ces sources d'énergie. En effet, l'énergie solaire concentrée pourrait être utilisée pour fournir de l'énergie à haute température à la réaction de gazéification. Le gaz de synthèse ainsi produit pourrait donc être considéré comme un vecteur de l'énergie solaire.

L'étude du couplage de ces deux sources d'énergie a débuté après le premier choc pétrolier, mais l'intérêt suscité est retombé avec la baisse du prix du baril de pétrole. Aujourd'hui, ce champ de recherche connaît un renouveau. La viabilité économique de cette approche a été établie [9] et des études techniques voient le jour [10, 11].

Cependant, les efforts de recherche se concentrent sur un couplage à l'échelle réacteur et ne permettent malheureusement pas une compréhension fine de l'interaction entre la biomasse et le rayonnement solaire concentré. Les rares études à l'échelle du laboratoire couplant biomasse et énergie solaire n'ont, pendant longtemps, considéré l'énergie solaire que comme une technique permettant d'atteindre de fortes vitesses de chauffes [20–24]. Ce n'est que récemment que la pyrolyse solaire a été étudiée en elle-même pour déterminer les propriétés des chars produits avec ce mode de chauffage particulier [25].

En plus du comportement général de la biomasse, la combinaison de ces deux sources d'énergie soulève des questions. Une forte vitesse de chauffe pourrait conduire à :

- une vaporisation rapide de l'eau contenue par l'échantillon, induisant une forte surpression interne qui pourrait engendrer une rupture mécanique de l'échantillon
- une pyrolyse rapide ne produisant que très peu de char et favorisant l'ablation rapide du solide produit

Des températures élevées pourraient mener à :

- des craquages thermiques et au reformage des goudrons, ainsi que la gazéification du char à l'intérieur même de l'échantillon
- la désactivation thermique du char
- la sublimation du carbone, si les températures atteintes sont suffisamment importantes

En plus de l'étude générale de l'interaction entre le rayonnement solaire concentré et la biomasse, ce travail a aussi pour but de répondre à ces questions. Dans un premier temps, l'état de l'art sur ce sujet a été dressé, ce qui a permis de choisir le hêtre comme biomasse modèle. Dans un second temps, un dispositif expérimental permettant d'exposer la biomasse à des flux supérieurs à 1000 kW/m^2 a été conçu et réalisé. Il a ainsi été possible d'explorer l'impact de l'orientation des fibres du bois par rapport au flux incident et l'influence de la teneur en eau initiale de la biomasse. Dans un troisième temps, un modèle numérique décrivant le comportement de la biomasse sous haute densité de flux solaire a été développé. L'accord entre les prédictions du modèle et les observations expérimentales est bon. Dans ces conditions, le modèle a été utilisé pour mieux comprendre les phénomènes mis en jeu lors de la dégradation de la biomasse sous haute densité de flux solaire.

Etat de l'art

Une revue de l'état de l'art met en lumière les trois étapes successives de la dégradation de la biomasse : le séchage, la pyrolyse et la gazéification du char (Fig. E.1).

Le séchage d'un échantillon peut avoir lieu selon deux processus différents :

- par diffusion, l'eau quittant le milieu sous l'effet d'un gradient de concentration en vapeur d'eau entre l'échantillon et son environnement
- par ébullition, la température de l'échantillon s'élevant à 100 °C, l'eau boue, crée une surpression et un courant gazeux éjectant la vapeur d'eau s'instaure

La pyrolyse a lieu entre 400 et 800 °C. Au cours de cette transformation, les polymères qui composent la biomasse se dégradent en trois grandes espèces : le char, un résidu carboné solide, les goudrons, un mélange plus de 300 molécules gazeuses à température de pyrolyse mais liquides à température ambiante (qui inclue l'eau le plus souvent) et les gaz légers, qui restent sous forme gazeuse à température ambiante (de H_2 à C_3H_8). Les proportions relatives et la compositions de ces trois produits varient selon les conditions dans lesquelles la pyrolyse a été menée [41, 44–50] (Fig. 1.3). Les grandes tendances sont :

- plus une pyrolyse est rapide, plus elle produit de goudrons au détriment du char et des gaz légers

FIGURE E.1: Les différentes étapes de la dégradation de la biomasse

- plus la température finale de la pyrolyse est élevée, plus la pyrolyse produit de char et de gaz légers

La gazéification regroupe des réactions chimiques hétérogènes qui consomment le composé carboné. Durant ces réactions, un agent oxydant, le plus souvent la vapeur d'eau ou le dioxyde de carbone, réagit avec le char pour produire du dihydrogène et du monoxyde de carbone. A la fin de cette étape, il ne reste plus que du gaz de synthèse et des cendres.

L'expérience a mis en lumière, qu'en plus de la complexité inhérente à chacun de ces trois phénomènes, chacun d'eux a une influence sur les étapes qui lui succèdent.

Tout comme leur compréhension intrinsèque, modélisation des trois étapes de dégradation de la biomasse est un défi. Pour chacun de ces phénomènes, différentes modélisations sont possibles selon le niveau de précision requis.

Il existe trois grandes catégories de modèle pour décrire le séchage de la biomasse. Les premiers basent leurs prédictions sur la courbe d'équilibre liquide-vapeur de l'eau. Ils sont connus pour donner de très bon résultats, mais au prix d'une implémentation lourde et d'un temps de calcul élevé. Les seconds considèrent le séchage comme un phénomène thermiquement activé décrit avec une loi d'Arrhenius permettant la vaporisation de l'eau liquide aux alentours de 100 °C. Le dernier type de modèle décrit le séchage comme un puits d'énergie à une température fixée de 100 °C, tant qu'il reste de l'eau liquide toute l'énergie apportée sert à vaporiser l'eau. Une fois l'eau vaporisée, le chauffage du milieu peut reprendre.

Il existe quatre grandes approches pour décrire la pyrolyse de la biomasse. La

première considère des pseudo-espèces. Elle décrit la transformation du bois en char, gaz et goudrons, mais n'est pas capable de prédire la composition de chacune de ces pseudo-espèces [104]. La seconde considère la biomasse comme un mélange de cellulose, hémicelluloses et lignines. Elle offre de meilleures prédictions, mais nécessite de connaître finement la composition de la biomasse [105]. La troisième est capable de prédire la production de différentes espèces en considérant entre 10 et 50 réactions chimiques. Le modèle le plus connu est le modèle de Ranzi [106]. La dernière catégorie, appelée FG-DVC (pour Functional Group-Depolymerization, Vaporisation, Crosslinking) a été initialement développée et appliquée aux charbons. Elle décrit la cellulose, les hémicelluloses et les lignines comme des groupes de monomères reliés par des liaisons chimiques. Sous l'effet de la température et de la pression, ces liaisons peuvent se rompre et se reformer ; c'est ainsi que sont pris en compte les réactions de dépolymérisation et de repolymérisation au sein de l'échantillon [107].

Cette revue de l'état de l'art a mis en lumière le manque d'étude, expérimentale comme numérique, sur le comportement de la biomasse sous haute densité de flux solaire. Ces travaux de thèse ont donc pour but de contribuer à la réduction de ce manque.

Matériels et méthodes

Pour mener à bien cette étude, il a été nécessaire de mettre au point un dispositif expérimental permettant d'exposer la biomasse à de fortes densités de flux (supérieures à 1000 kW/m^2) tout en contrôlant l'atmosphère autour de l'échantillon. Le dispositif expérimental se divise en trois parties : les échantillons, la chambre de réaction et la source radiative. Lors d'un essai, l'échantillon est placé dans la chambre de réaction qui l'isole de environnement, puis il est éclairé à l'aide d'un soleil artificiel (Fig. E.2).

Les échantillons ont été conçus de façon à être thermiquement épais et à se comporter comme un mur semi-infini lors d'une exposition durant 5 minutes. Ce sont des cylindres de hêtre de 10 cm de diamètre et 5 cm de haut. Le bois étant un matériaux anisotrope, une attention particulière a été apportée à l'orientation des fibres du bois par rapport à la direction du flux de chaleur incident. Pour déterminer l'impact de ce paramètre sur le comportement de la biomasse sous haute densité de flux solaire, deux séries d'échantillons ont été fabriquées (Fig. 2.1) : l'une en bois de bout, dont les fibres sont verticales et parallèles au flux de chaleur incident, et l'autre en bois de fil, dont les fibres sont horizontales et perpendiculaires au flux de chaleur incident. La teneur en eau initiale des échantillons étant un paramètre potentiellement important, son influence a aussi été étudiée. Ainsi, trois teneurs en eau initiales différentes ont été testées : 0 %wb (wet basis : base humide) correspondant à un bois séché en étuve, 9 %wb, représentant un bois séché en extérieur et 55 %wb simulant un bois après l'abattage. Les différents échantillons ont été caractérisés par des analyses immédiates et ultimes, mais aussi des mesures de densités (Tables 2.1, 2.2 et 2.3).

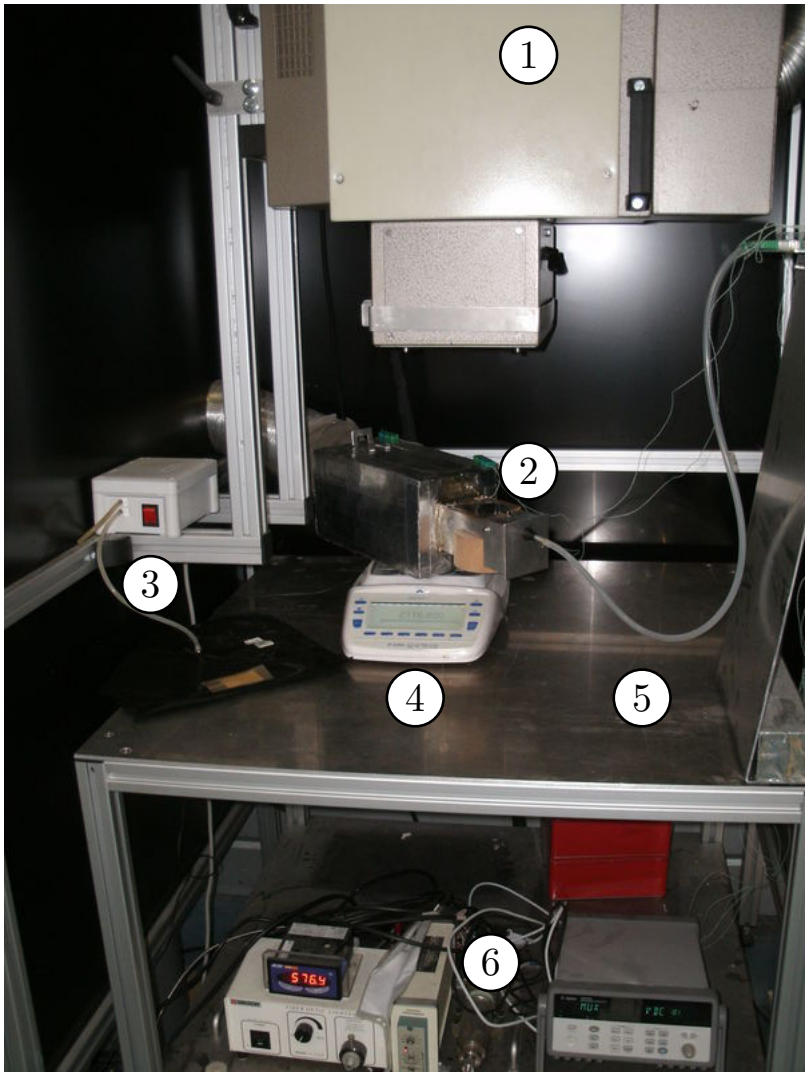

FIGURE E.2: Photographie du dispositif expérimental. 1: soleil artificiel, 2: chambre de réaction, 3: système d'échantillonnage des gaz, 4: balance, 5: table en acier, 6: système d'acquisition des températures

La chambre de réaction a été conçue avec une idée simple : placer l'échantillon dans un canal balayé par de l'azote permettrait d'exposer l'échantillon au travers d'une fenêtre, tout en évacuant les gaz produits vers un dispositif condensant les goudrons et analysant les gaz restants (Fig. 2.4 et 2.5).

La chambre de réaction est donc un canal balayé par un courant laminaire de diazote. Le caractère laminaire de l'écoulement permet de s'assurer que les goudrons produits par la pyrolyse de l'échantillon n'entrent pas en contact avec le hublot permettant le passage du flux radiatif. En effet, en s'y déposant, les goudrons l'obscurciraient, ce qui aurait pour conséquence de faire augmenter sa température jusqu'à sa rupture. Une fois évacués de la proximité immédiate de l'échantillon, les gaz produits traversent un mélangeur statique. Ce mélangeur a pour but d'homogénéiser la température de l'écoulement avant son passage au travers d'un condenseur à goudrons. Le condenseur à goudrons est une partie

amovible du dispositif. Il est principalement constitué de billes d'aluminium qui sont refroidies à l'azote liquide avant chaque essai. En traversant le condenseur, le courant gazeux refroidi et des gouttelettes de goudrons se forment ; ces gouttelettes sont ensuite arrêtées par un filtre en coton placé à la sortie du condenseur. Le gaz ainsi épuré des goudrons est analysé par une microGC. Enfin, le système est pesé en permanence par une balance, ce qui permet de suivre l'évolution de sa masse. Des thermocouples ainsi qu'un pyromètre bichromatique permettent quant à eux l'acquisition de différentes températures.

Pour des raisons pratique, un soleil artificiel a été utilisé pour mener cette étude. Ce dispositif est composé d'une lampe à arc au xénon et d'un miroir focalisant (Fig. 2.9). La lampe est placée au premier foyer d'un miroir elliptique. Ainsi, le rayonnement émis par la lampe est dirigé vers le second foyer, où se trouve la surface supérieure de l'échantillon. La lampe utilisée durant cette étude a une puissance électrique nominale de 4 kWe avec un rendement de conversion en énergie radiative de 50 %. Pour intercepter un maximum d'énergie, le miroir le plus grand du marché a été utilisé pour concentrer le rayonnement émis.

Il a été nécessaire d'étalonner le dispositif. Cependant, l'étalonnage d'un tel dispositif se révèle assez difficile. En effet, les méthodes conventionnelles de mesures de flux (telles que les fluxmètres Gardon) ne permettent pas de caractériser des flux aussi élevés que ceux produits par le soleil artificiel. Une nouvelle méthode d'étalonnage a donc été développée. Cette méthode consiste, dans un premier temps, à exposer au flux incident un écran en acier (acier inoxydable 304L) dont les propriétés physiques et radiatives sont connues. Une caméra infrarouge est utilisée pour suivre l'évolution de la température de l'acier au cours du temps. Dans un second temps, les cartes de température obtenues sont traitées par méthodes inverses, ce qui permet de décorréler l'élévation locale de température associée à la conduction de celle induite par le flux incident. Il est ainsi possible de déterminer le flux incident. Cette méthode a été validée par d'autres techniques de mesures pour des flux modérés ; elle donne de très bons résultats.

Après avoir conçu, réalisé et étalonné le dispositif expérimental, l'étape suivante a tout naturellement été la réalisation de campagnes d'essais.

Résultats expérimentaux

Six configurations différentes ont été testées : les trois teneurs en eau initiales (0, 9 et 55 %wb) pour chacune des deux orientations des fibres (bois de bout et bois de fil).

Après exposition, la géométrie de l'échantillon a fortement évolué. Un cratère, ayant une forme semblable à celle du flux incident, s'est développé au sein du milieu (Fig. E.3). Selon la teneur en eau initiale de la biomasse, ce cratère peut contenir ou non des bâtonnets de char (Fig. 3.8 et 3.9). Nous montrons que deux mécanismes différents de formation du cratère sont à l'œuvre selon les cas. Pour les échantillons

ne contenant que peu d'eau initialement (0 et 9 %wb), le char se contracte en se formant. Cette contraction induit des contraintes qui finissent par conduire à la rupture du milieu. Ainsi, le milieu se disloque laissant place à des bâtonnets. Pour les échantillons ayant une forte teneur en eau initiale (55 %wb), le char produit par la pyrolyse est consommé par la vapeur d'eau provenant du séchage au cours d'une réaction de gazéification. Ainsi, un cratère se forme, mais sans bâtonnets de char.

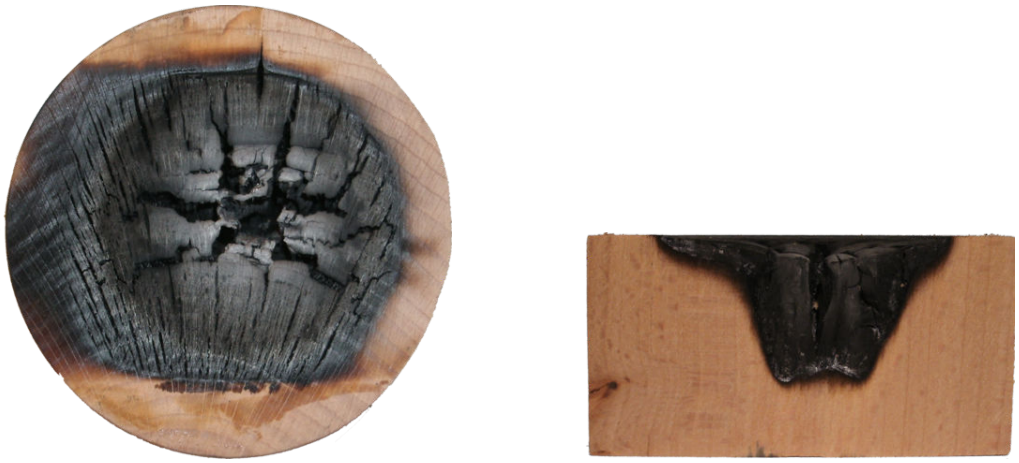

(A) Vue de dessus (B) Vue en coupe

FIGURE E.3: Vues de l'échantillon après 5 minutes d'exposition, pour le cas de référence (9 %wb, bois de bout)

Etonnement, l'orientation des fibres du bois par rapport au flux incident n'a qu'un effet mineur sur le comportement de la biomasse sous haute densité de flux solaire. Les taux de production/consommation entre les deux configurations extrêmes (bois de bout et bois de fil) sont proches (Fig. E.4). Il en va de même pour les températures relevées (Table 3.1) et la composition des gaz produits (Tables 3.4 et 3.5). Les rares différences sont : la forme du cratère, la taille des bâtonnets de char, ou leur structure interne (Table 3.3).

Quant à elle, la teneur en eau initiale de la biomasse a une influence importante sur son comportement lors de son exposition à un fort flux radiatif. Les échantillons ayant une forte teneur en eau initiale produisent plus de gaz - pour une même quantité de bois sec convertie - que les autres échantillons. Pas ailleurs, ce gaz est plus riche en dihydrogène. Cela s'explique par le fait que la gazéification du char par l'eau de séchage produit du dihydrogène. Enfin, les échantillons ayant une forte teneur en eau initiale ne produisent que très peu de goudrons, ce qui permet de penser que les goudrons produits par la pyrolyse subissent un reformage par l'eau de séchage.

Un bilan énergétique du système a été dressé. Il met en lumière que le rendement de conversion énergétique, i.e. la sommes des puissances utiles en sortie (contenues dans les gaz, les goudrons et le char) par rapport aux puissances en entrée (contenue dans la biomasse et l'énergie solaire), est de l'ordre de 90% pour les échantillons secs, là où il n'est que de 59 % pour les échantillons humides.

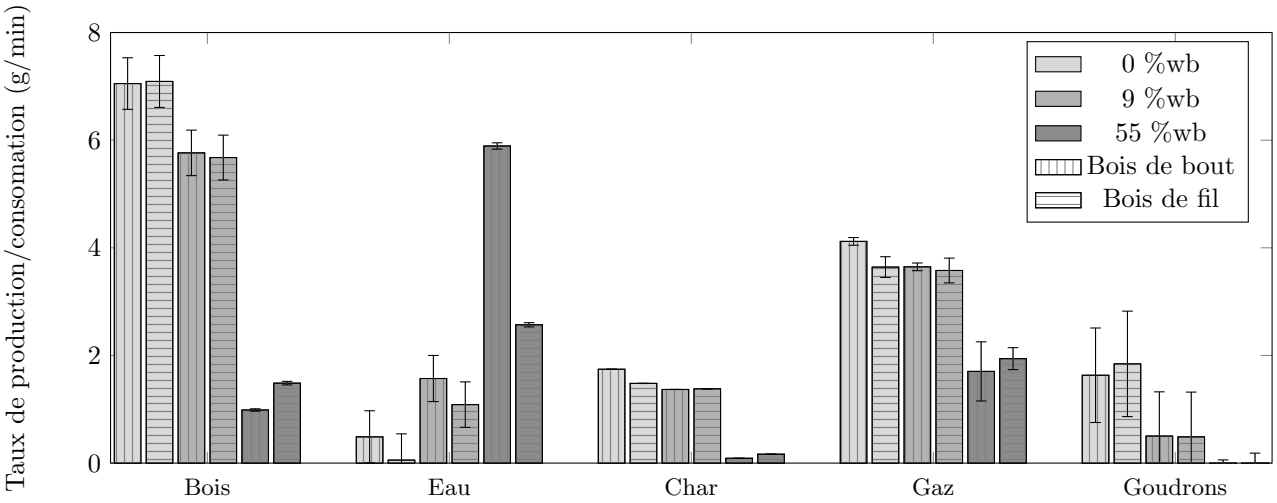

FIGURE E.4: Taux de production/consommation pour les six configurations

Modèle numérique

Un modèle numérique décrivant le comportement des échantillons a été construit dans le but de mieux comprendre les phénomènes mis en jeu lors de la dégradation de la biomasse sous haute densité de flux solaire (Fig. E.5).

Ce modèle s'appuie sur trois grandes équations de conservation : masse, quantité de mouvement et chaleur (Eq. 4.7, 4.8, 4.16 et 4.19). Les choix des formes utilisées (loi de Darcy, modèle à une température) sont défendus par des nombres adimensionnels (nombre de Reynolds de pores, nombre de Péclet de pores).

La dégradation de la biomasse est décrite en utilisant un schéma à pseudo-espèces [104] (Fig. E.6 et Table 4.3). Le séchage est décrit à l'aide d'une courbe d'équilibre liquide vapeur [89]. Deux modifications ont été apportées aux données issues de la littérature : le schéma a été modifié pour prendre en compte l'eau produite par la pyrolyse et la quantité de char produit prédite par le modèle a été corrigée à la hausse.

Au vue de l'étendue de la plage de température mise en jeu dans ce modèle, une attention particulière a été portée au choix des propriétés physiques décrivant le milieu. Autant que faire se peut, il a été choisi d'avoir recours à des corrélations décrivant l'évolution des propriétés physiques avec la température (Tables 4.4, 4.5 et Annexe B).

La construction de ce modèle a soulevé deux points cruciaux en terme de modélisation : la déformation du milieu, ainsi que la pénétration du rayonnement à l'intérieur du cratère, doivent être prise en compte pour prédire correctement le comportement de la biomasse sous haute densité de flux solaire. La déformation du domaine de calcul est basée sur un critère simple : quand la porosité excède 0.975, le domaine de calcul se déforme pour prendre en compte la consommation de la matière. Le maillage est alors déformé et les champs résolus sont interpolés entre

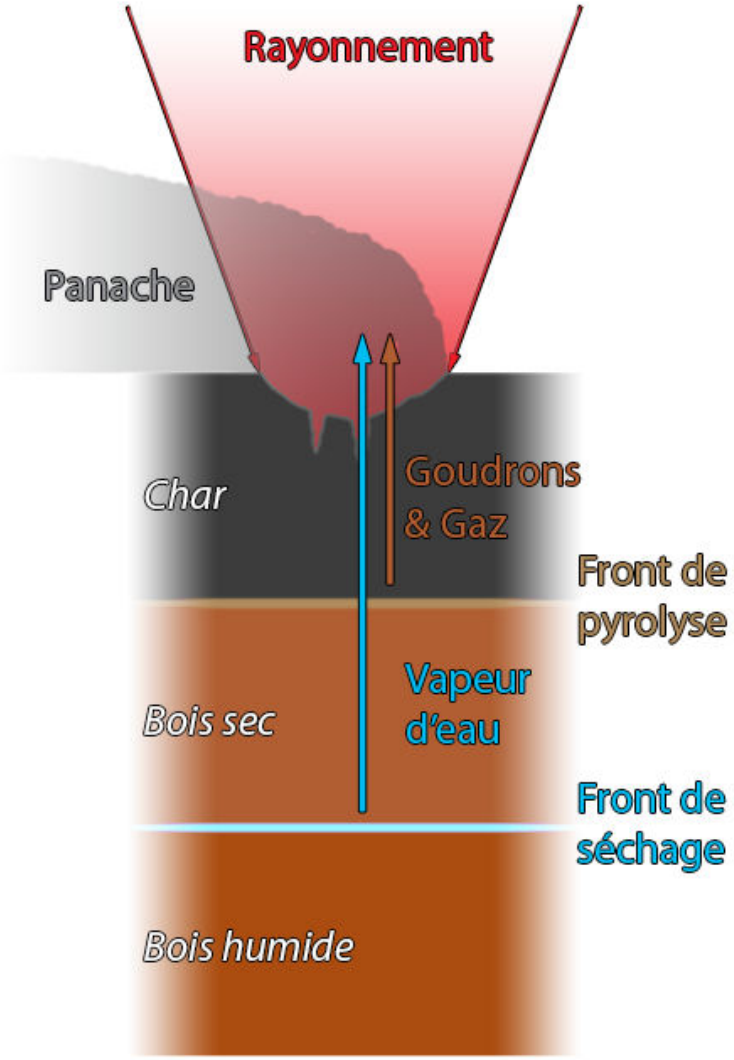

FIGURE E.5: Schéma de principe d'un échantillon lors de sa dégradation

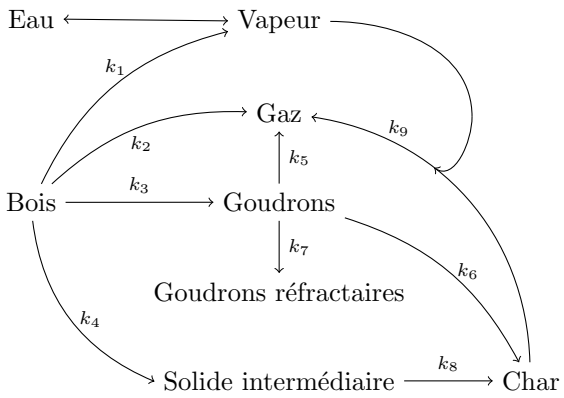

FIGURE E.6: Modèle de séchage et de pyrolyse de la biomasse

l'ancien et le nouveau maillage (Fig. 4.4).

Différentes stratégies ont été mises en œuvre pour prendre en compte la pénétration du rayonnement dans le milieu (Fig. 4.5 et 4.7). In fine, il est nécessaire de décrire la divergence du faisceau lumineux au sein de l'échantillon pour correctement prédire l'évolution de la géométrie du milieu (Fig. 4.6).

Résultats numériques

Dans un premier temps les hypothèses de construction du modèle ont été validées. Puis, les prédictions obtenues ont été confrontées aux observations expérimentales. L'accord entre le modèle et les expériences est bon sur un plan qualitatif, i.e. apparition de fronts de séchage, pyrolyse et gazéification, et correct sur un plan quantitatif (Fig. E.7 et Table 5.1). Le modèle capture bien l'évolution des champs solides, mais seulement la tendance pour les produits gazeux.

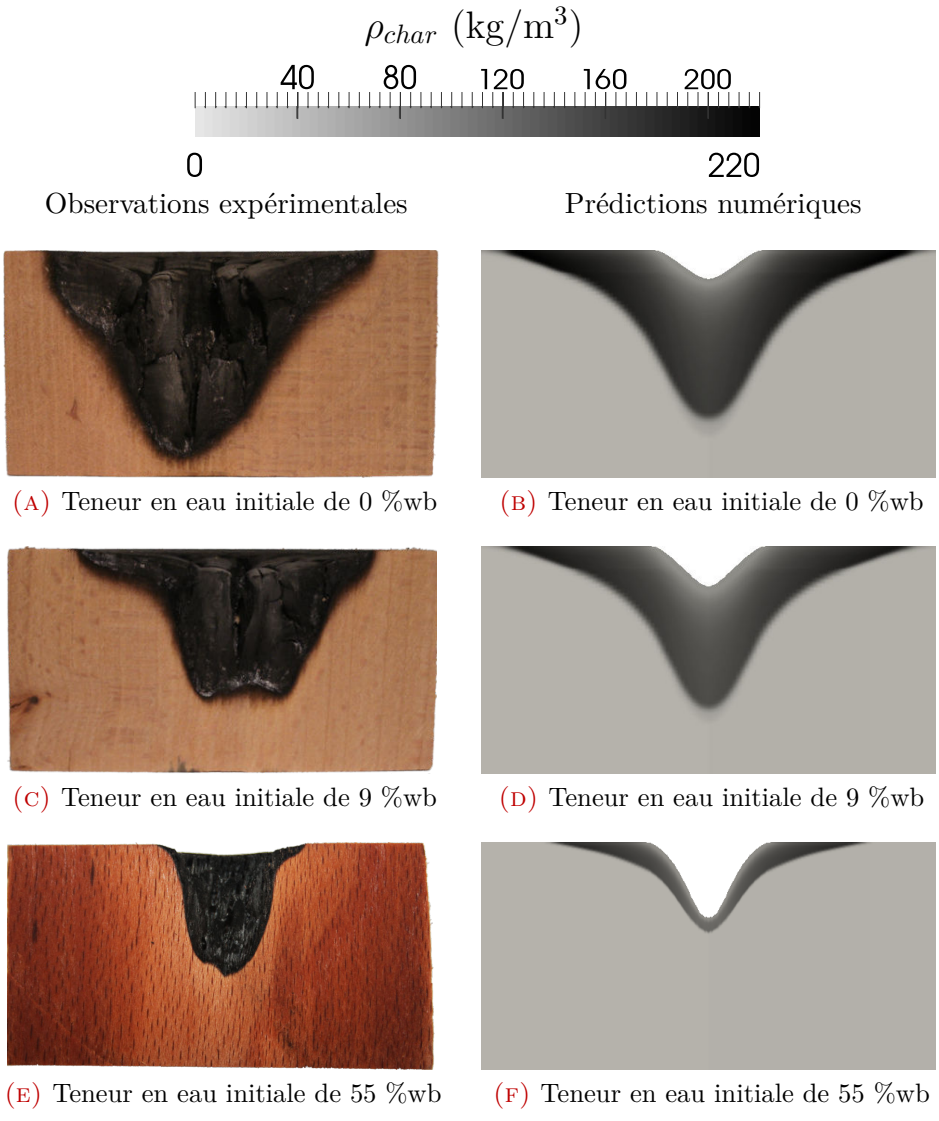

(A) Teneur en eau initiale de 0 %wb

(B) Teneur en eau initiale de 0 %wb

(C) Teneur en eau initiale de 9 %wb

(D) Teneur en eau initiale de 9 %wb

(E) Teneur en eau initiale de 55 %wb

(F) Teneur en eau initiale de 55 %wb

FIGURE E.7: Vues en coupe des cratères observés expérimentalement et prédis numériquement. Echelle de couleur : masse volumique du char

Les prédictions du modèle mettent en lumière la forte probabilité que l'histoire thermique des goudrons ne s'arrête pas à la sortie de l'échantillon. Ces derniers subissent très probablement des craquages thermiques et du reformage après avoir quitté l'échantillon. En outre, le modèle valide l'explication du creusement du cratère par la gazéification pour les échantillons à forte teneur en eau initiale.

Trois analyses de sensibilités, ayant pour but d'évaluer la pertinence des décisions prises lors de la construction du modèle, ont été menées. Le modèle de séchage choisi (équilibre liquide-vapeur) a été confronté à un modèle de type Arrhenius. Il apparaît que le modèle de type Arrhenius ne prédit pas correctement la condensation de la vapeur dans les zones froides de l'échantillon. Il surestime la quantité d'eau retenue par l'échantillon.

L'influence du facteur de correction appliqué à la production de char a été analysée. Cet ajustement n'a qu'un impact mineur sur le comportement du modèle. Il modifie effectivement la quantité de char produit, mais n'a pas d'effet indésirable sur les autres grandeurs prédites par le modèle.

Comme pour le modèle de séchage, l'importance du choix du modèle de pyrolyse a été évaluée en utilisant un autre modèle de dégradation de la biomasse. Les prédictions du modèle alternatif sont de nettement moins bonne qualité que celles du modèle choisi pour cette étude. Le choix du modèle de pyrolyse s'avère donc déterminant.

Conclusion

Durant ces trois dernières années, ce travail a essayé de contribuer à une meilleure compréhension du comportement de la biomasse sous haute densité de flux solaire. Au cours de ce travail, il a été montré que :

- même pour les échantillons ayant une forte teneur en eau initiale, les surpressions internes induites par le séchage ne provoquent pas rupture mécanique de l'échantillon
- les vitesses de chauffe atteintes ne sont pas assez importantes pour donner lieu à une pyrolyse ne produisant pas de char
- le craquage thermique et le reformage des goudrons, ainsi que la gazéification du char produit par la pyrolyse, ont lieu pendant l'exposition de la biomasse à de forts flux solaires
- un temps d'exposition de quelques minutes n'est pas suffisant pour que le char subisse une désactivation thermique, même sous de forts flux solaires
- les températures mises en jeu ne permettent pas la sublimation du carbone

De façon synthétique, ces travaux permettent de tirer deux grandes conclusions. D'une part, la pyro-gazéification solaire de biomasse humide promeut la production

d'un gaz riche en dihydrogène tout en réduisant la quantité de goudrons produits. D'autre part, la pyro-gazéification solaire de biomasse sèche offre un très bon rendement dans une optique de conversion énergétique.

Bibliography

[1] 2014 Key World Energy Statistics. Technical report, International Energy Agency, 2015.

[2] Climate change 2014 - Synthesis report. Technical report, International Panel on Climate Change, 2014.

[3] World Energy Outlook 2014. Technical report, International Energy Agency, November 2014.

[4] International Energy Outlook 2013. DOE/EIA-0484(2013), United States Energy Information Administration, Washington, D.C., 2013.

[5] Robert F. Service. Sunlight in Your Tank. *Science*, 326(5959):1472–1475, December 2009. WOS:000272623600010.

[6] Heidi C. Butterman and Marco J. Castaldi. CO2 as a Carbon Neutral Fuel Source via Enhanced Biomass Gasification. *Environmental Science & Technology*, 43(23):9030–9037, December 2009.

[7] Abdelhamid Belghit. *Etude théorique et expérimentale d'un gazéifieur solaire de matière carbonées en lit poreux mobile*. PhD thesis, Université de Perpignan, 1986.

[8] M Morris and L Waldheim. Energy recovery from solid waste fuels using advanced gasification technology. *Waste Management*, 18(6–8):557–564, October 1998.

[9] Edgar G. Hertwich and Xiangping Zhang. Concentrating-Solar Biomass Gasification Process for a 3rd Generation Biofuel. *Environmental Science & Technology*, 43(11):4207–4212, June 2009. WOS:000266546700039.

[10] Nicolas Piatkowski, Christian Wieckert, Alan W. Weimer, and Aldo Steinfeld. Solar-driven gasification of carbonaceous feedstock-a review. *Energy & Environmental Science*, 4(1):73–82, January 2011. WOS:000285748400006.

[11] Ange Nzihou, Gilles Flamant, and Brian Stanmore. Synthetic fuels from biomass using concentrated solar energy – A review. *Energy*, 42(1):121–131, June 2012.

[12] Nicolas Piatkowski, Christian Wieckert, and Aldo Steinfeld. Experimental investigation of a packed-bed solar reactor for the steam-gasification of carbonaceous feedstocks. *Fuel Processing Technology*, 90(3):360–366, March 2009.

[13] E.D. Gordillo and A. Belghit. A downdraft high temperature steam-only solar gasifier of biomass char: A modelling study. *Biomass and Bioenergy*, 35(5):2034–2043, 2011.

[14] Martin Flechsenhar and Christian Sasse. Solar gasification of biomass using oil shale and coal as candidate materials. *Energy*, 20(8):803–810, 1995.

[15] E.D. Gordillo and A. Belghit. A bubbling fluidized bed solar reactor model of biomass char high temperature steam-only gasification. *Fuel Processing Technology*, 92(3):314–321, March 2011.

[16] X.T. Li, J.R. Grace, C.J. Lim, A.P. Watkinson, H.P. Chen, and J.R. Kim. Biomass gasification in a circulating fluidized bed. *Biomass and Bioenergy*, 26(2):171–193, 2004.

[17] P.v. Zedtwitz and A. Steinfeld. The solar thermal gasification of coal — energy conversion efficiency and CO2 mitigation potential. *Energy*, 28(5):441–456, 2003.

[18] Colomba Di Blasi, Carmen Branca, Antonio Santoro, and Raul Alberto Perez Bermudez. Weight loss dynamics of wood chips under fast radiative heating. *Journal of Analytical and Applied Pyrolysis*, 57(1):77–90, January 2001.

[19] A. Z'Graggen and A. Steinfeld. Hydrogen production by steam-gasification of carbonaceous materials using concentrated solar energy – V. Reactor modeling, optimization, and scale-up. *International Journal of Hydrogen Energy*, 33(20):5484–5492, October 2008.

[20] Wai-Chun R. Chan, Marcia Kelbon, and Barbara B. Krieger. Modelling and experimental verification of physical and chemical processes during pyrolysis of a large biomass particle. *Fuel*, 64(11):1505–1513, November 1985.

[21] Antonio Galgano and Colomba Di Blasi. Modeling the propagation of drying and decomposition fronts in wood. *Combustion and Flame*, 139(1–2):16–27, October 2004.

[22] Jacques Lédé, Fabrice Blanchard, and Olivier Boutin. Radiant flash pyrolysis of cellulose pellets: products and mechanisms involved in transient and steady state conditions. *Fuel*, 81(10):1269–1279, 2002.

[23] Olivier Authier, Monique Ferrer, Guillain Mauviel, Az-Eddine Khalfi, and Jacques Lede. Wood Fast Pyrolysis: Comparison of Lagrangian and Eulerian Modeling Approaches with Experimental Measurements. *Industrial & Engineering Chemistry Research*, 48(10):4796–4809, May 2009. WOS:000266081300016.

[24] Mélina Christodoulou, Guillain Mauviel, Jacques Lédé, Pascal Beaurain, Mathieu Weber, Hervé Legall, and Francis Billaud. Novel vertical image furnace for fast pyrolysis studies. *Journal of Analytical and Applied Pyrolysis*, 103:255–260, September 2013.

[25] Kuo Zeng, Doan Pham Minh, Daniel Gauthier, Elsa Weiss-Hortala, Ange Nzihou, and Gilles Flamant. The effect of temperature and heating rate on char properties obtained from solar pyrolysis of beech wood. *Bioresource Technology*, 182:114–119, April 2015.

[26] Solar Energy Perspectives. Technical report, International Energy Agency, 2011.

[27] Department of Energy. SunShot Vision Study. Technical report, U.S. Department of Energy, Washington, D.C., 2012.

[28] A. Imhof. Decomposition of limestone in a solar reactor. *Renewable Energy*, 10(2–3):239–246, 1997.

[29] A IMHOF. THE CYCLONE REACTOR - AN ATMOSPHERIC OPEN SOLAR REACTOR. *Solar Energy Materials*, 24(1-4):733–741, December 1991. WOS:A1991HH26900065.

[30] A Meier, E Bonaldi, GM Celia, and W Lipinski. Multitube rotary kiln for the industrial solar production of lime RID A-3700-2010. *Journal of Solar Energy Engineering-Transactions of the Asme*, 127(3):386–395, August 2005. WOS:000231452400012.

[31] Anton Meier, Enrico Bonaldi, Gian Mario Cella, Wojciech Lipinski, and Daniel Wuillemin. Solar chemical reactor technology for industrial production of lime. *Solar Energy*, 80(10):1355–1362, October 2006.

[32] *Wood Handbook, Wood as an Engineering Material*. U.S. Department of Agriculture, usda edition, 2010.

[33] Donny L. Hamilton. *Methods of Conserving Underwater Archaeological Material Culture*. Texas A&M University, conservation of cultural resources i. nautical archaeology program edition, 1998.

[34] Eusebe Agoua and Patrick Perre. Mass Transfer in Wood: Identification of Structural Parameters from Diffusivity and Permeability Measurements. *Journal of Porous Media*, 13(11):1017–1024, 2010. WOS:000285561200008.

[35] Morten Gunnar Grønli. *A theoretical and experimental study of the thermal degradation of biomass*. dissertation, Norwegian University of Science and Technology, 1996. A theoretical and experimental study of the thermal degradation of biomass.

[36] Harvey D. Erickson and Western Dry Kiln Clubs. *Mechanisms of moisture movement in woods*. College of Forestry, 1954.

[37] Marc Borrega and Petri P. Karenlampi. Three mechanisms affecting the mechanical properties of spruce wood dried at high temperatures. *Journal of Wood Science*, 56(2):87–94, April 2010. WOS:000276910300001.

[38] F. Thuvander, L. Wallström, L. A. Berglund, and K. A. H. Lindberg. Effects of an impregnation procedure for prevention of wood cell wall damage due to drying. *Wood Science and Technology*, 34(6):473–480, 2001.

[39] Mihaela Campean, Ion Marinescu, and Mihai Ispas. Influence of drying temperature upon some mechanical properties of beech wood. *Holz Als Roh-Und Werkstoff*, 65(6):443–448, December 2007. WOS:000250631100005.

[40] Galina Dobele, Igors Urbanovich, Aleksandr Volpert, Valdis Kampars, and Eriks Samulis. FAST PYROLYSIS - EFFECT OF WOOD DRYING ON THE YIELD AND PROPERTIES OF BIO-OIL RID A-8235-2012. *Bioresources*, 2(4):699–706, November 2007. WOS:000263689700017.

[41] C. Branca, P. Giudicianni, and C. Di Blasi. GC/MS characterization of liquids generated from low-temperature pyrolysis of wood. *Industrial & Engineering Chemistry Research*, 42(14):3190–3202, July 2003. WOS:000183991400003.

[42] J. M. Commandré, H. Lahmidi, S. Salvador, and N. Dupassieux. Pyrolysis of wood at high temperature: The influence of experimental parameters on gaseous products. *Fuel Processing Technology*, 92(5):837–844, May 2011.

[43] Nicolas Piatkowski and Aldo Steinfeld. Solar gasification of carbonaceous waste feedstocks in a packed-bed reactor—Dynamic modeling and experimental validation. *AIChE Journal*, 57(12):3522–3533, December 2011.

[44] M. Guerrero, M.P. Ruiz, M.U. Alzueta, R. Bilbao, and A. Millera. Pyrolysis of eucalyptus at different heating rates: studies of char characterization and oxidative reactivity. *Journal of Analytical and Applied Pyrolysis*, 74(1–2):307–314, 2005.

[45] Ca Koufopanos, G Maschio, and A Lucchesi. Kinetic Modeling of the Pyrolysis of Biomass and Biomass Components. *Canadian Journal of Chemical Engineering*, 67(1):75–84, February 1989. WOS:A1989T381400010.

[46] Colomba Di Blasi. Combustion and gasification rates of lignocellulosic chars. *Progress in Energy and Combustion Science*, 35(2):121–140, 2009.

[47] Floriane Mermoud. *Gazéification de charbon de bois à la vapeur d'eau: de la particule isolée au lit fixe continu*. PhD thesis, Institut National Polytechnique de Toulouse, 2006.

[48] Morten G. Grønli and Morten C. Melaaen. Mathematical Model for Wood PyrolysisComparison of Experimental Measurements with Model Predictions. *Energy Fuels*, 14(4):791–800, 2000.

[49] F. Mermoud, S. Salvador, L. Van de Steene, and F. Golfier. Influence of the pyrolysis heating rate on the steam gasification rate of large wood char particles. *Fuel*, 85(10–11):1473–1482, July 2006.

[50] Rolando Zanzi, Krister Sjöström, and Emilia Björnbom. Rapid high-temperature pyrolysis of biomass in a free-fall reactor. *Fuel*, 75(5):545–550, 1996.

[51] Carole Couhert, Jean-Michel Commandre, and Sylvain Salvador. Is it possible to predict gas yields of any biomass after rapid pyrolysis at high temperature from its composition in cellulose, hemicellulose and lignin? *Fuel*, 88(3):408–417, March 2009.

[52] Heidi C. Butterman and Marco J. Castaldi. CO2 enhanced steam gasification of biomass fuels. In *16th Annual North American Waste-to-Energy Conference*, pages 157–172. American Society of Mechanical Engineers, 2008.

[53] Colomba Di Blasi, Carmen Branca, Antonio Santoro, and Elier Gonzalez Hernandez. Pyrolytic behavior and products of some wood varieties. *Combustion and Flame*, 124(1–2):165–177, January 2001.

[54] G. Varhegyi, Mj Antal, T. Szekely, and P. Szabo. Kinetics of the Thermal-Decomposition of Cellulose, Hemicellulose, and Sugar-Cane Bagasse. *Energy & Fuels*, 3(3):329–335, June 1989. WOS:A1989U746700012.

[55] Eric M. Suuberg, Ivan Milosavljevic, and Vahur Oja. Two-regime global kinetics of cellulose pyrolysis: The role of tar evaporation. *Symposium (International) on Combustion*, 26(1):1515–1521, 1996.

[56] Jacques Lédé. Comparison of contact and radiant ablative pyrolysis of biomass. *Journal of Analytical and Applied Pyrolysis*, 70(2):601–618, 2003.

[57] Anthony Dufour, Bajil Ouartassi, Roda Bounaceur, and André Zoulalian. Modelling intra-particle phenomena of biomass pyrolysis. *Chemical Engineering Research and Design*, 89(10):2136–2146, October 2011.

[58] Xavier Deglise and André Donnot. Bois énergie. *Techniques de l'ingénieur BE*, 8535:1–21, 2004.

[59] T. Cornelissen, J. Yperman, G. Reggers, S. Schreurs, and R. Carleer. Flash co-pyrolysis of biomass with polylactic acid. Part 1: Influence on bio-oil yield and heating value. *Fuel*, 87(7):1031–1041, June 2008.

[60] Ayhan Demirbas. Pyrolysis of ground beech wood in irregular heating rate conditions. *Journal of Analytical and Applied Pyrolysis*, 73(1):39–43, March 2005.

[61] Colomba Di Blasi. Dynamic behaviour of stratified downdraft gasifiers. *Chemical Engineering Science*, 55(15):2931–2944, August 2000.

[62] Yufu Xu, Wendong Li, Xianguo Hu, and Yinyan Shi. *Preparation and characterization of bio-oil from biomass*. INTECH Open Access Publisher, 2011.

[63] Olivier Beaumont and Yvan Schwob. Influence of physical and chemical parameters on wood pyrolysis. *Industrial & Engineering Chemistry Process Design and Development*, 23(4):637–641, 1984.

[64] Ayhan Demirbas. Oily products from mosses and algae via pyrolysis. *Energy Sources Part a-Recovery Utilization and Environmental Effects*, 28(10):933–940, July 2006. WOS:000239323200004.

[65] Pt Williams, S. Besler, and Dt Taylor. The Pyrolysis of Scrap Automotive Tires - the Influence of Temperature and Heating Rate on Product Composition. *Fuel*, 69(12):1474–1482, December 1990. WOS:A1990EL23500002.

[66] C. Guizani, F. J. Escudero Sanz, and S. Salvador. Influence of temperature and particle size on the single and mixed atmosphere gasification of biomass char with H2o and CO2. *Fuel Processing Technology*, 134:175–188, June 2015.

[67] Dong Zeng, Michael Clark, Todd Gunderson, William C. Hecker, and Thomas H. Fletcher. Swelling properties and intrinsic reactivities of coal chars produced at elevated pressures and high heating rates. *Proceedings of the Combustion Institute*, 30(2):2213–2221, January 2005.

[68] Tom Melchior, Christopher Perkins, Paul Lichty, Alan W. Weimer, and Aldo Steinfeld. Solar-driven biochar gasification in a particle-flow reactor. *Chemical Engineering and Processing: Process Intensification*, 48(8):1279–1287, 2009.

[69] Capucine Dupont, Timothée Nocquet, José Augusto Da Costa Jr., and Christèle Verne-Tournon. Kinetic modelling of steam gasification of various woody biomass chars: Influence of inorganic elements. *Bioresource Technology*, 102(20):9743–9748, October 2011.

[70] F. Marquez-Montesinos, T. Cordero, J. Rodrı?guez-Mirasol, and J.J. Rodrı?guez. CO2 and steam gasification of a grapefruit skin char. *Fuel*, 81(4):423–429, March 2002.

[71] I.I. Ahmed and A.K. Gupta. Kinetics of woodchips char gasification with steam and carbon dioxide. *Applied Energy*, 88(5):1613–1619, 2011.

[72] V Minkova, S.P Marinov, R Zanzi, E Björnbom, T Budinova, M Stefanova, and L Lakov. Thermochemical treatment of biomass in a flow of steam or in a mixture of steam and carbon dioxide. *Fuel Processing Technology*, 62(1):45–52, January 2000.

[73] Y.J. Lu, H. Jin, L.J. Guo, X.M. Zhang, C.Q. Cao, and X. Guo. Hydrogen production by biomass gasification in supercritical water with a fluidized bed reactor. *International Journal of Hydrogen Energy*, 33(21):6066–6075, November 2008.

[74] Thomas A. Milne, Nicolas Abatzoglou, and Robert J. Evans. *Biomass gasifier" tars": Their nature, formation, and conversion*, volume 570. National Renewable Energy Laboratory Golden, CO, 1998.

[75] T. Wongchang, S. Patumsawad, and B. Fungtammasan. An Analysis of Wood Pyrolysis Tar from High Temperature Thermal Cracking Process. *Energy Sources, Part A: Recovery, Utilization, and Environmental Effects*, 35(10):926–935, May 2013.

[76] Hirotatsu Watanabe, Yosuke Morinaga, and Ken Okazaki. Steam-Reforming Characteristics of Heavy and Light Tars Derived from Cellulose. *Journal of Thermal Science and Technology*, 7(1):180–189, 2012. WOS:000305075400013.

[77] Baofeng Zhao, Xiaodong Zhang, Lei Chen, Rongbo Qu, Guangfan Meng, Xiaolu Yi, and Li Sun. Steam reforming of toluene as model compound of biomass pyrolysis tar for hydrogen. *Biomass and Bioenergy*, 34(1):140–144, January 2010.

[78] M. Puig-Arnavat, E. A. Tora, J. C. Bruno, and A. Coronas. State of the art on reactor designs for solar gasification of carbonaceous feedstock. *Solar Energy*, 97:67–84, November 2013.

[79] G. Baud, J. J. Bezian, M. El Hafi, and G. Olalde. A theoretical and experimental study of the time-dependent radiative properties of a solar bubbling fluidized bed receiver. *Solar Energy*, 105:341–353, July 2014.

[80] X. Q. Wang, S. R. A. Kersten, W. Prins, and W. P. M. van Swaaij. Biomass pyrolysis in a fluidized bed reactor. Part 2: Experimental validation of model results. *Industrial & Engineering Chemistry Research*, 44(23):8786–8795, November 2005. WOS:000233214000040.

[81] Nicolas Piatkowski and Aldo Steinfeld. Solar-driven coal gasification in a thermally irradiated packed-bed reactor. *Energy & Fuels*, 22(3):2043–2052, June 2008. WOS:000256057600086.

[82] A. Gómez-Barea, P. Ollero, and R. Arjona. Reaction-diffusion model of TGA gasification experiments for estimating diffusional effects. *Fuel*, 84(12–13):1695–1704, September 2005.

[83] Tf Wall and Hb Becker. Total Absorptivities and Emissivities of Particulate Coal Ash from Spectral Band Emissivity Measurements. *Journal of Engineering for Gas Turbines and Power-Transactions of the Asme*, 106(4):771–776, 1984. WOS:A1984TP58000009.

[84] Jingwei Chen, Youjun Lu, Liejin Guo, Ximin Zhang, and Peng Xiao. Hydrogen production by biomass gasification in supercritical water using concentrated solar energy: System development and proof of concept. *International Journal of Hydrogen Energy*, 35(13):7134–7141, 2010.

[85] A. Z'Graggen, P. Haueter, G. Maag, A. Vidal, M. Romero, and A. Steinfeld. Hydrogen production by steam-gasification of petroleum coke using concentrated solar power—III. Reactor experimentation with slurry feeding. *International Journal of Hydrogen Energy*, 32(8):992–996, 2007.

[86] Syed Shabbar Raza and Isam Janajreh. Solar Assisted Gasification of Solid Feedstock: Optical Arrangement and Numerical Simulation. *International Journal of Thermal & Environmental Engineering*, 7(2):65–72, 2014.

[87] C. Guesdon, I. Alxneit, H. R. Tschudi, D. Wuillemin, and M. Sturzenegger. 1 kW imaging furnace with in situ measurement of surface temperature. *Review of Scientific Instruments*, 77(3):035102, March 2006. WOS:000236739100040.

[88] Julien Blondeau and Hervé Jeanmart. Biomass pyrolysis at high temperatures: Prediction of gaseous species yields from an anisotropic particle. *Biomass and Bioenergy*, 41:107–121, June 2012.

[89] Patrick Perré and Ian W. Turner. A 3-D version of TransPore: a comprehensive heat and mass transfer computational model for simulating the drying of porous media. *International Journal of Heat and Mass Transfer*, 42(24):4501–4521, December 1999.

[90] Gary L. Borman and Kenneth W. Ragland. *Combustion engineering*. McGraw-Hill, January 1998.

[91] Richard B. Bates and Ahmed F. Ghoniem. Modeling kinetics-transport interactions during biomass torrefaction: The effects of temperature, particle size, and moisture content. *Fuel*, 137:216–229, December 2014. WOS:000341303300027.

[92] S. Salvador, M. Quintard, and C. David. Combustion of a substitution fuel made of cardboard and polyethylene: Influence of the mix characteristics-Modeling. *Fire and Materials*, 32(7):417–444, November 2008. WOS:000261118100003.

[93] D. K. Shen, M. X. Fang, Z. Y. Luo, and K. F Cen. Modeling pyrolysis of wet wood under external heat flux. *Fire Safety Journal*, 42(3):210–217, April 2007.

[94] Kenneth M. Bryden, Kenneth W. Ragland, and Christopher J. Rutland. Modeling thermally thick pyrolysis of wood. *Biomass and Bioenergy*, 22(1):41–53, January 2002.

[95] Ramin Mehrabian, Selma Zahirovic, Robert Scharler, Ingwald Obernberger, Stefan Kleditzsch, Siegmar Wirtz, Viktor Scherer, Hong Lu, and Larry L. Baxter. A CFD model for thermal conversion of thermally thick biomass particles. *Fuel Processing Technology*, 95:96–108, March 2012.

[96] Saeed Danaei Kenarsari and Yuan Zheng. Fast Pyrolysis of Biomass Pellets Using Concentrated Solar Radiation: A Numerical Study. *Journal of Solar Energy Engineering-Transactions of the Asme*, 136(4):041004, November 2014. WOS:000344346600004.

[97] Adrian Bejan. *Convection Heat Transfer*. Wiley, August 1984.

[98] G Chauveteau and C Thirriot. *Sur les pertes de charge en écoulement laminaire dans quelques géométries simple et dans le milieu poreux.* Trieste, trieste edition, 1965.

[99] N. Puiroux, M. Prat, and M. Quintard. Non-equilibrium theories for macroscale heat transfer: ablative composite layer systems. *International Journal of Thermal Sciences*, 43(6):541–554, June 2004.

[100] Capucine Dupont. *Vapogazéification de la biomasse : contribution a létude de la phénomènologie entre 800 et 1000 °C*. PhD thesis, Université Claude Bernard, 2006.

[101] B. Moghtaderi. The state-of-the-art in pyrolysis modelling of lignocellulosic solid fuels. *Fire and Materials*, 30(1):1–34, February 2006. WOS:000235521800001.

[102] R. Chan and B. B. Krieger. Modeling of Physical and Chemical Processes During Pyrolysis of a Large Biomass Pellet with Experimental Verification. *Prepr. Pap., Am. Chem. Soc., Div. Fuel Chem.; (United States)*, 28:5, January 1983.

[103] Pious O. Okekunle, Teeranai Pattanotai, Hirotatsu Watanabe, and Ken Okazaki. Numerical and Experimental Investigation of Intra-Particle Heat Transfer and Tar Decomposition during Pyrolysis of Wood Biomass. *Journal of Thermal Science and Technology*, 6(3):360–375, 2011. WOS:000295920800004.

[104] Won Chan Park, Arvind Atreya, and Howard R. Baum. Experimental and theoretical investigation of heat and mass transfer processes during wood pyrolysis. *Combustion and Flame*, 157(3):481–494, March 2010.

[105] Dinesh Mohan, Charles U. Pittman, and Philip H. Steele. Pyrolysis of Wood/Biomass for Bio-oil: A Critical Review. *Energy & Fuels*, 20(3):848–889, May 2006.

[106] Eliseo Ranzi, Alberto Cuoci, Tiziano Faravelli, Alessio Frassoldati, Gabriele Migliavacca, Sauro Pierucci, and Samuele Sommariva. Chemical Kinetics of Biomass Pyrolysis. *Energy & Fuels*, 22(6):4292–4300, November 2008.

[107] J. M. Jones, M. Pourkashanian, A. Williams, and D. Hainsworth. A comprehensive biomass combustion model. *Renewable Energy*, 19(1–2):229–234, January 2000.

[108] Th. Damartzis, G. Ioannidis, and A. Zabaniotou. Simulating the behavior of a wire mesh reactor for olive kernel fast pyrolysis. *Chemical Engineering Journal*, 136(2–3):320–330, March 2008.

[109] Victor Pozzobon, Sylvain Salvador, Jean Jacques Bézian, Mouna El-Hafi, Yannick Le Maoult, and Gilles Flamant. Radiative pyrolysis of wet wood under intermediate heat flux: Experiments and modelling. *Fuel Processing Technology*, 128:319–330, December 2014.

[110] Colomba Di Blasi. Heat, momentum and mass transport through a shrinking biomass particle exposed to thermal radiation. *Chemical Engineering Science*, 51(7):1121–1132, April 1996.

[111] J. Larfeldt, B. Leckner, and M. C. Melaaen. Modelling and measurements of heat transfer in charcoal from pyrolysis of large wood particles. *Biomass & Bioenergy*, 18(6):507–514, 2000. WOS:000087546500007.

[112] T. Kojima, P. Assavadakorn, and T. Furusawa. Measurement and evaluation of gasification kinetics of sawdust char with steam in an experimental fluidized bed. *Fuel Processing Technology*, 36(1–3):201–207, December 1993.

[113] Hyung Chul Yoon, Peter Pozivil, and Aldo Steinfeld. Thermogravimetric pyrolysis and gasification of lignocellulosic biomass and kinetic summative law for parallel reactions with cellulose, xylan, and lignin. *Energy & Fuels*, 26(1):357–364, 2011.

[114] Capucine Dupont, Li Chen, Julien Cances, Jean-Michel Commandre, Alberto Cuoci, Sauro Pierucci, and Eliseo Ranzi. Biomass pyrolysis: Kinetic modelling and experimental validation under high temperature and flash heating rate conditions. *Journal of Analytical and Applied Pyrolysis*, 85(1–2):260–267, 2009.

[115] Kamil Kwiatkowski, Konrad Bajer, Agnieszka Celińska, Marek Dudyński, Jakub Korotko, and Marta Sosnowska. Pyrolysis and gasification of a thermally thick wood particle – Effect of fragmentation. *Fuel*, 132:125–134, September 2014.

[116] Jean Lachaud and Nagi Mansour. Porous-material Analysis Toolbox based on OpenFOAM-extend and Applications. In *44th AIAA Thermophysics Conference*, Fluid Dynamics and Co-located Conferences. American Institute of Aeronautics and Astronautics, June 2013.

[117] J. Donea, Antonio Huerta, J.-Ph Ponthot, and A. Rodriguez-Ferran. *Encyclopedia of Computational Mechanics Vol. 1: Fundamentals., Chapter 14: Arbitrary Lagrangian-Eulerian Methods*. Wiley & Sons, 2004.

[118] Victor Pozzobon and Sylvain Salvador. High heat flux mapping using infrared images processed by inverse methods: an application to solar concentrating systems. *Solar Energy*, 117C:29–.35, 2015.

[119] Ayhan Demirbas. Combustion characteristics of different biomass fuels. *Progress in energy and combustion science*, 30(2):219–230, 2004.

[120] K. W. Ragland, D. J. Aerts, and A. J. Baker. Properties of wood for combustion analysis. *Bioresource technology*, 37(2):161–168, 1991.

[121] Michael Ploetze and Peter Niemz. Porosity and pore size distribution of different wood types as determined by mercury intrusion porosimetry. *European Journal of Wood and Wood Products*, 69(4):649–657, November 2011. WOS:000295787600018.

[122] C. Guesdon, I. Alxneit, H. R. Tschudi, D. Wuillemin, J. Petrasch, Y. Brunner, L. Winkel, and M. Sturzenegger. PSI's 1 kW imaging furnace—A tool for high-temperature chemical reactivity studies. *Solar Energy*, 80(10):1344–1348, October 2006.

[123] Joerg Petrasch, Patrick Coray, Anton Meier, Max Brack, Peter Haeberling, Daniel Wuillemin, and Aldo Steinfeld. A novel 50 kW 11,000 suns high-flux solar simulator based on an array of xenon arc lamps. *Journal of Solar Energy Engineering-Transactions of the Asme*, 129(4):405–411, November 2007. WOS:000250637900008.

[124] Jawad Sarwar, Grigoris Georgakis, Robert LaChance, and Nesrin Ozalp. Description and characterization of an adjustable flux solar simulator for solar thermal, thermochemical and photovoltaic applications. *Solar Energy*, 100:179–194, February 2014. WOS:000331007700018.

[125] Li Chen. *Fast pyrolysis of millimetric wood particles between 800°C and 1000°C*. Lyon 1, December 2009.

[126] Christian Gueymard. *SMARTS2: a simple model of the atmospheric radiative transfer of sunshine: algorithms and performance assessment*. Florida Solar Energy Center Cocoa, FL, 1995.

[127] J. Llorente, J. Ballestrin, and A. J. Vazquez. A new solar concentrating system: Description, characterization and applications. *Solar Energy*, 85(5):1000–1006, May 2011. WOS:000290644000029.

[128] Daniel S. Codd, Andrew Carlson, Jennifer Rees, and Alexander H. Slocum. A low cost high flux solar simulator. *Solar Energy*, 84(12):2202–2212, December 2010.

[129] N.D. Kaushika and S. Kaneff. Flux distribution and intercept factors in the focal region of paraboloidal dish concentrators. In *Proc. ISES Solar World Congress*, volume 2, pages 1607–1611, Hamburg, 1987.

[130] M. Mohammadiun, A. B. Rahimi, and I. Khazaee. Estimation of the time-dependent heat flux using the temperature distribution at a point by conjugate gradient method. *International Journal of Thermal Sciences*, 50(12):2443–2450, December 2011.

[131] Zhaohong Fang, Donglai Xie, Nairen Diao, John R. Grace, and C. Jim Lim. A new method for solving the inverse conduction problem in steady heat flux measurement. *International Journal of Heat and Mass Transfer*, 40(16):3947–3953, October 1997.

[132] Helcio R. B. Orlande, Olivier Fudym, Denis Maillet, and Renato M. Cotta, editors. *Thermal Measurements and Inverse Techniques*. CRC Press, Boca Raton, FL, May 2011.

[133] D. Hernandez, G. Olalde, J. M. Gineste, and C. Gueymard. Analysis and experimental results of solar-blind temperature measurements in solar furnaces. *Journal of Solar Energy Engineering-Transactions of the Asme*, 126(1):645–653, February 2004. WOS:000189287100013.

[134] J. Ballestrín, M. Rodríguez-Alonso, J. Rodríguez, I. Cañadas, F. J. Barbero, L. W. Langley, and A. Barnes. Calibration of high-heat-flux sensors in a solar furnace. *Metrologia*, 43(6):495, December 2006.

[135] R. S. Graves, T. G. Kollie, D. L. McElroy, and K. E. Gilchrist. The thermal conductivity of AISI 304l stainless steel. *International Journal of Thermophysics*, 12(2):409–415, March 1991.

[136] Chunli Fan, Fengrui Sun, and Li Yang. Simple Numerical Method for Multidimensional Inverse Identification of Heat Flux Distribution. *Journal of Thermophysics and Heat Transfer*, 23(3):622–629, September 2009. WOS:000268300300023.

[137] You-An Shi, Lei Zeng, Wei-Qi Qian, and Ye-Wei Gui. A data processing method in the experiment of heat flux testing using inverse methods. *Aerospace Science and Technology*, 29(1):74–80, August 2013.

[138] H. M. Park and W. S. Jung. On the solution of multidimensional inverse heat conduction problems using an efficient sequential method. *Journal of Heat Transfer-Transactions of the Asme*, 123(6):1021–1029, December 2001. WOS:000172645400001.

[139] Ayhan Demirbas. Determination of calorific values of bio-chars and pyro-oils from pyrolysis of beech trunkbarks. *Journal of Analytical and Applied Pyrolysis*, 72(2):215–219, November 2004.

[140] P. M. Mortensen, J. D. Grunwaldt, P. A. Jensen, K. G. Knudsen, and A. D. Jensen. A review of catalytic upgrading of bio-oil to engine fuels. *Applied Catalysis A: General*, 407(1–2):1–19, November 2011.

[141] L.P.L.M. Rabou, R.J.C. van Leijenhorst, and J.H.O. Hazewinkel. *High efficiency power production from biomass and waste*. ECN Biomass, Coal and Environmental Research, November 2008.

[142] Lars Waldheim and Torbjörn Nilsson. Heating value of gases from biomass gasification. *Report prepared for: IEA bioenergy agreement, Task*, 20, 2001.

[143] Guillaume Gauthier. *Synthèse de biocarburants de deuxième génération : Etude de la pyrolyse à haute température de particules de bois centimétriques*. PhD thesis, INPT EMAC, 2013.

[144] HITRAN on the Web.

[145] Eric. Dimensional Shrinkage.

[146] Je Hirschfelder. Molecular Theory of Gases and Liquids. *New York: John Wiley & Sons, Inc.(a) p*, 165:562, 1957.

[147] M. Quintard, M. Kaviany, and S. Whitaker. Two-medium treatment of heat transfer in porous media: numerical results for effective properties. *Advances in Water Resources*, 20(2–3):77–94, April 1997.

[148] Fabrice Golfier and Michel Quintard. Heat and mass transfer in tubes: An analysis using the method of volume averaging. *Journal of Porous Media*, 5(2):169–185, 2002.

[149] Ej Kansa, He Perlee, and Rf Chaiken. Mathematical-Model of Wood Pyrolysis Including Internal Forced-Convection. *Combustion and Flame*, 29(3):311–324, 1977. WOS:A1977DU60400010.

[150] Jaakko Saastamoinen and Jean-Robert Richard. Simultaneous drying and pyrolysis of solid fuel particles. *Combustion and Flame*, 106(3):288–300, August 1996.

[151] Czesław Buraczewski and Jan Stasiek. Application of generalized Pythagoras theorem to calculation of configuration factors between surfaces of channels of revolution. *International journal of heat and fluid flow*, 4(3):157–160, 1983.

[152] Theodore L. Bergman, Frank P. Incropera, and Adrienne S. Lavine. *Fundamentals of heat and mass transfer*. John Wiley & Sons, 2011.

[153] Y. Chen and T. C. Bond. Light absorption by organic carbon from wood combustion. *Atmos. Chem. Phys.*, 10(4):1773–1787, 2010.

[154] Philipp Hass, Falk K. Wittel, Sam A. McDonald, and Federica Marone. Pore space analysis of beech wood: The vessel network. *Holzforschung*, 64:639–644, 2010.

[155] Toshiro Harada, Toshimitsu Hata, and Shigehisa Ishihara. Thermal constants of wood during the heating process measured with the laser flash method. *Journal of Wood Science*, 44(6):425–431, 1998.

[156] S. Youcef-Ali and J.Y. Desmons. Numerical and experimental study of a solar equipped with offset rectangular plate fin absorber plate. *Renewable Energy*, 31(13):2063–2075, October 2006.

[157] Michael Forsth and Arne Roos. Absorptivity and its dependence on heat source temperature and degree of thermal breakdown. *Fire and Materials*, 35(5):285–301, September 2011. WOS:000294175800003.

[158] Adam L. Redman, Henri Bailleres, Ian Turner, and Patrick Perré. MASS TRANSFER PROPERTIES (PERMEABILITY AND MASS DIFFUSIVITY) OF FOUR AUSTRALIAN HARDWOOD SPECIES. *BioResources*, 7(3):3410–3424, June 2012.

[159] W. Y. Walter, T. Ezra, and C. George. Combined conductive/radiative heat transfer in high porosity fibrous insulation materials: theory and experiment. In *The 6th ASME-JSME thermal engineering joint conference*, 2003.

[160] John C. Chen and Stuart W. Churchill. Radiant heat transfer in packed beds. *AIChE Journal*, 9(1):35–41, January 1963.

[161] Isaac I Kantorovich and Ezra Bar-Ziv. Heat transfer within highly porous chars: a review. *Fuel*, 78(3):279–299, February 1999.

[162] S Duber, J.-N Rouzaud, C Clinard, and S Pusz. Microporosity and optical properties of some activated chars. *Fuel Processing Technology*, 77–78(0):221–227, 2002.

[163] P. Boulet, G. Parent, Z. Acem, T. Rogaume, T. Fateh, J. Zaida, and F. Richard. Characterization of the radiative exchanges when using a cone calorimeter for the study of the plywood pyrolysis. *Fire Safety Journal*, 51:53–60, July 2012.

[164] Eli Grushka and V. Maynard. Measurements of gaseous diffusion coefficients by gas chromatography. *Journal of Chemical Education*, 49(8):565, August 1972.

[165] T. R. Marrero and E. A. Mason. Gaseous Diffusion Coefficients. *Journal of Physical and Chemical Reference Data*, 1(1):3, 1972.

[166] Henry G. Weller, G. Tabor, Hrvoje Jasak, and C. Fureby. A tensorial approach to computational continuum mechanics using object-oriented techniques. *Computers in physics*, 12(6):620–631, 1998.

[167] OpenFOAM - The Open Source Computational Fluid Dynamics (CFD) Toolbox.

[168] Markus Nordlund. Modified Rhie-Chow/PISO algorithm for collocated variable finite porous media flow solvers. In *5th International Conference on Porous Media and Their Applications in Science, Engineering and Industry*, 2014.

[169] I. Burgert and D. Eckstein. The tensile strength of isolated wood rays of beech (Fagus sylvatica L.) and its significance for the biomechanics of living trees. *Trees-Structure and Function*, 15(3):168–170, March 2001. WOS:000168336800006.

[170] Allen L. Robinson, Steven G. Buckley, Nancy Yang, and Larry L. Baxter. Experimental Measurements of the Thermal Conductivity of Ash Deposits: Part 2. Effects of Sintering and Deposit Microstructure. *Energy Fuels*, 15(1):75–84, 2000.

[171] R. S. Miller and J. Bellan. Analysis of reaction products and conversion time in the pyrolysis of cellulose and wood particles. *Combustion Science and Technology*, 119(1-6):331–373, 1996. WOS:A1996WP80000015.

[172] M Gupta, J Yang, and C Roy. Specific heat and thermal conductivity of softwood bark and softwood char particles. *Fuel*, 82(8):919–927, May 2003. WOS:000182003900006.

[173] G. Leon, J. Cruz-de Leon, and L. Villasenor. Thermal characterization of pine wood by photoacoustic and photothermal techniques. *European Journal of Wood and Wood Products*, 58(4):241–246, 2000.

[174] O Boutin, J Lede, G Olalde, and A Ferriere. Solar flash pyrolysis of biomass direct measurement of the optical properties of biomass components. *Journal De Physique Iv*, 9(P3):367–372, March 1999. WOS:000080492400058.

[175] Wang Jinman, Dai Chengyue, and Liu Yixing. Wood permeability. *Journal of Forestry Research*, 2(1):91–97, 1991.

[176] Jyuung-Shiauu Chern and Allan N. Hayhurst. A model for the devolatilization of a coal particle sufficiently large to be controlled by heat transfer. *Combustion and Flame*, 146(3):553–571, August 2006. WOS:000239871400012.

[177] M. W Chase, United States, and National Bureau of Standards. *NIST-JANAF Themochemical Tables*. American Chemical Society ; American Institute of Physics for the National Bureau of Standards, Washington, D.C.; New York, fourth edition edition, 1998.

[178] Thermal Conductivity of Nitrogen from Dortmund Data Bank.

[179] Charles F. Bonilla, Robert D. Brooks, and Philip L. Jr. Walker. The Viscosity of Steam and of Nitrogen at Atmospheric Pressure and High Temperature. In *Heat-Transfer Discussions*, pages 79–85, London, September 1951.

[180] J. Millat and W. A. Wakeham. The Thermal Conductivity of Nitrogen and Carbon Monoxide in the Limit of Zero Density. *Journal of Physical and Chemical Reference Data*, 18(2):565–581, April 1989.

[181] Eckhard Vogel. Towards Reference Viscosities of Carbon Monoxide and Nitrogen at Low Density Using Measurements between 290k and 680k as well as Theoretically Calculated Viscosities. *International Journal of Thermophysics*, 33(5):741–757, May 2012.

[182] L. S. Zaitseva, L. V. Yakush, and N. A. Vanicheva. Thermal conductivities of benzene and toluene vapors. *Journal of engineering physics*, 31(5):1292–1295, November 1976.

[183] Robert D. Goodwin. Benzene Thermophysical Properties from 279 to 900 K at Pressures to 1000 Bar. *Journal of Physical and Chemical Reference Data*, 17(4):1541–1636, October 1988.

[184] Kim Wonsoo, Chair Tong-Seek, and Pak Hyunsuk. A Paradigm for the Viscosity of Fluids. *Bull. Korean Chem. Soc.*, 9(4):213 –217, February 1998.

[185] Maria L. V. Ramires, Carlos A. Nieto de Castro, Yuchi Nagasaka, Akira Nagashima, Marc J. Assael, and William A. Wakeham. Standard Reference Data for the Thermal Conductivity of Water. *Journal of Physical and Chemical Reference Data*, 24(3):1377–1381, May 1995.

List of Figures

List of Tables

Biomass gasification under high solar heat flux

Abstract: Concentrated solar energy is as an alternative energy source to power the thermochemical conversion of biomass into energy or materials with high added value. Production of syngas from lignocellulosic biomass is an example, as well as the production of carbonaceous residues with controlled properties.

This work focuses on the study of the behaviour of a thermally thick beech wood sample under high solar heat flux (higher than 1000 kW/m^2). Two approaches have been undertaken at the same time: an experimental study and the development of a numerical model.

Experiments have highlighted a specific behaviour of beech wood under high solar heat flux. Indeed, a char crater, symmetrical to the incident heat flux distribution, forms in the sample. This study has also shown that biomass initial moisture content has a strong impact on its behaviour. The dry sample can achieve an energetic conversion efficiency of 90 %, capturing up to 72 % of the incident solar power in chemical form. While, high initial moisture content samples produce more hydrogen, at the price of an energetic conversion efficiency around 59 %. Furthermore, tar thermal cracking and steam reforming are enabled by the temperatures reached (higher than 1200 °C) and the presence of water. Finally, wood fiber orientation has been shown to have only a minor impact on its behaviour.

At the same time, a modelling of the coupled reactions, heat and mass transfers at stake during solar gasification was undertaken. The development of this model has highlighted the necessity to implement innovative strategies to take into account radiation penetration into the medium as well as its deformation by gasification. Numerical model predictions are in good agreement with experimental observations. Based on the model predicted behaviour, further understanding of biomass behaviour under high solar heat flux was derived. In addition, sensitivity analyses revealed that Arrhenius type models are not fitted for precise intra-particular water behaviour description and that the choice of the pyrolysis scheme is key to properly model biomass behaviour under high solar heat flux.

Keywords: Solar energy, Pyrolysis, Gasification, High heat flux, Drying, Wood.

Gazéification de biomasse sous haute densité de flux solaire

Résumé : L'énergie solaire concentrée est une source d'énergie alternative pour la conversion thermochimique de biomasse en vecteurs énergétiques ou en matériaux à haute valeur ajoutée. La production d'un gaz de synthèse à partir de biomasse lignocellulosique en est un exemple, de même que la production de résidus carbonés à propriétés contrôlées.

Ces travaux portent sur l'étude du comportement d'un échantillon de hêtre thermiquement épais sous de hautes densités de flux solaire (supérieures à 1000 kW/m^2). Deux approches ont été développées en parallèles : une étude expérimentale et le développement d'un modèle numérique.

Les expériences ont permis de mettre en lumière le comportement particulier du hêtre sous de hautes densités de flux solaire. En effet, un cratère de char, dont la forme correspond à celle de la distribution du flux incident, se forme dans l'échantillon. Cette étude a aussi montré que la teneur en eau initiale de la biomasse a un fort impact sur son comportement. Les échantillons secs peuvent atteindre un rendement de conversion énergétique de 90 %, capturant jusqu'à 72 % de l'énergie solaire incidente sous forme chimique. Quant aux échantillons humides, ils produisent nettement plus d'hydrogène, au prix d'un rendement de conversion énergétique aux alentours de 59 %. De plus, le craquage thermique et le reformage des goudrons produits par la pyrolyse sont rendus possibles par les températures atteintes (supérieures à 1200 °C) et la présence d'eau. Enfin, il a été montré que l'orientation des fibres du bois n'a qu'un impact mineur sur son comportement.

En parallèle, une modélisation des transferts couplés chaleur matière et des réactions chimiques mis en jeu lors de la gazéification solaire d'un échantillon a été développée. La construction du modèle a mis en avant la nécessité de recourir à des stratégies innovantes pour prendre en compte la pénétration du rayonnement dans la matière ainsi que la déformation du milieu par la gazéification. Les prédictions du modèle montrent un bon accord avec les observations expérimentales. Elles ont ainsi permis de mieux comprendre les couplages mis en jeu lors de la dégradation de biomasse sous haute densité de flux solaire. De plus, des analyses de sensibilités ont révélé que les modèles de type Arrhenius ne permettent pas de décrire finement le comportement de l'eau à l'intérieur de l'échantillon et que le choix du modèle de pyrolyse était capital pour décrire correctement le comportement la biomasse sous haute densité de flux solaire.

Mots-clés : Energie solaire, Pyrolyse, Gazéification, Haute densité de flux, Séchage, Bois.